NORTHWESTERN UNIVERSITY

Mixing and Segregation of Granular Flows in a 3D Tumbler

A DISSERTATION

SUBMITTED TO THE GRADUATE SCHOOL

IN PARTIAL FULFILLMENT OF THE REQUIREMENTS

for the degree

DOCTOR OF PHILOSOPHY

Field of Chemical and Biological Engineering

By

Mengqi Yu

EVANSTON, ILLINOIS

December 2020

ABSTRACT

Mixing and Segregation of Granular Flows in a 3D Tumbler

Mengqi Yu

Granular mixing has received less attention than fluid mixing due to the unique properties of granular materials and the complexity of their flow behaviors. Unlike fluid flows, where a continuum perspective accurately captures flow behavior, neither a continuum nor a discrete perspective by itself can describe the global behaviors of granular flows. The tendency of particle mixtures to segregate based on varying physical properties further complicates the mixing problem. In this work, a 3D granular tumbler flow system is considered as a prototype to study the behaviors of granular mixing that can be understood using dynamical systems approaches based on the "cutting-and-shuffling" mixing paradigm. The proposed mixing mechanism is a synergy of "cutting-and-shuffling" and "stretching in the flowing layer," a combination of discrete and continuum perspectives. This dissertation aims to tackle two main points, mixing and non-mixing behaviors induced by the underlying flow dynamics (no segregation), and the interaction between segregation and the said flow dynamics. The role of mixing with "cutting-and-shuffling" is first studied by taking into consideration of uncertainty in operations in a simplified one-dimensional case. In the 3D granular flow system, x-ray based particle tracking techniques are used to identify mixing and non-mixing behaviors corresponding to dynamical systems features predicted by the continuum model.

A continuum model, based purely on the flow kinematics, demonstrates that complex non-mixing and mixing regions exist in the system. When segregation is induced by using two physically distinct particle species, a pattern formation process is identified as a result of the interaction of segregation and flow dynamics including a weak axial perturbation. Statistical analysis enabled by discrete element method simulations (DEM), combined with continuum descriptions are used to uncover the mechanism of pattern formation of segregating granular materials in 3D tumbler flows.

Acknowledgements

My advisors Paul B. Umbanhowar, Richard M. Lueptow, and Julio M. Ottino have provided valuable guidance during my research. I am grateful for their tireless mentoring and support that make my work possible. Julio never ceases to inspire when he is around, through the whole-brain cross discipline seminar series, enlightening comments during group seminars, even just a brief chat in the hallway, and emails during the pandemic. Rich has been an example by his concentration, dedication, and mentoring for me in both research and interaction with professionals. He ensures that I get more than enough support and encouragement as well as critiques to do the best and even beyond what I can. Paul has been through numerous technical challenges with me together in utilizing various experimental and computational methods. He never fails to guide me ways of trouble shooting and always inspires creative solutions to problems. When I was digging my hole deep, he has reminded me the beauty and joy of science. I am also incredibly thankful for Rich and Paul's help in improving my writing, communication, and presentation in research as well as everyday interaction with people.

My research has also evolved with the help and mentoring from my colleagues. In particular, Zafir Zaman, who has started the x-ray experiments, not only trained me in designing and building experimental apparatus, but also in critical thinking and teamwork. Paul Park, has also been a great collaborator that shaped the earlier research. It was a great pleasure to share my experience here through discussions and activities with other colleagues, Zhekai Deng, Vidushi Dwivedi, Alexander Fry, Austin Isner, Ryan Jones, Thomas Lynn, Shen Meng,

Adithya Shankar, Lachlan Smith, Darius Wheeler, and Hongyi Xiao, and visiting scholars, Sam Zhao, and Ming Zhu.

I would also like to acknowledge my family and friends who provided support through difficult times during the past few years.

Lastly, the research in this dissertation is based on material funded by National Science Foundation Grant No.CMMI-1435065.

Table of Contents

List of Tables

List of Figures

CHAPTER 1

Introduction

SUMMARY

Granular mixing has received less attention than fluid mixing due to unique properties of granular materials and the complexity of their flow behaviors. Unlike fluid flows, where a continuum perspective is suitable to characterize behaviors, neither a continuum nor a discrete perspective by itself can describe the behaviors of granular flows. The tendency of particle mixtures to segregate, or de-mix, based on differing physical properties further complicates the mixing problem. In this dissertation, a 3D granular tumbler system is used as a prototype to study the behaviors of granular mixing using dynamical systems approaches based on the "cutting-and-shuffling" mixing paradigm. This dissertation tackles mixing and non-mixing behaviors induced by the underlying flow dynamics and the interaction between segregation and these flow dynamics. Hence, in this chapter several important concepts necessary for the remainder of the dissertation are defined and explained.

1.1. Mixing

1.1.1. What is mixing?

Mixing is a process that reduces heterogeneity of a system with components that differ in physical or chemical properties. It occurs naturally over a wide range of time and length scales. Some examples include material transport in blood vessels, gas exchange in lung alveoli, pollution dispersion in oceans, and magma transport in Earth's mantle. It is also a process that humans employ to create essentials in a variety of areas, including pastry making, concrete forming, polymer blending, pharmaceutical manufacturing, and microfluidic

mixing. Often, chemical reactions require a homogeneous mixture of reactants to take place efficiently. Pharmaceutical products require a precise composition of active and inactive ingredients to be effective and safe. Mixing is fundamental to many chemical engineering processes, but its effective and efficient realization tend to differ from system to system.

1.1.2. Mixing in fluid systems

Conventional mixing mechanisms of passive scalars in fluids can be categorized into classes dominated by diffusion, turbulence, or chaotic advection. Mixing by diffusion is a slow molecular-scale process driven by a concentration gradient. Turbulence, on the other hand, mixes quickly, but requires a high Reynold's number (and is not considered further here). Chaotic advection is a mixing process where materials are advected by laminar flow in a chaotic manner to create highly complex structures. It is characterized by the stretching of materials into long strips which are then folded back onto themselves, known as stretching and folding [113, 167]. This process is illustrated with dye experiments in a simple rectangular cavity flow in Fig. 1.1. Blobs of green and red fluorescent dyes (which do not affect the underlying flow) initially injected at different locations in the flow develop in strikingly different ways — the green dye remains a blob stretched only slightly, whereas the red dye is mixed well by stretching and folding of the chaotic flow. This experiment illustrates two important points, one being that the flow field in chaotic systems can be quite complex, and two, the overall mixing efficiency cannot be quantified in a simple measurement. For laminar flow, the flow material can be stretched and folded multiple times and still stay connected as thin filaments. Eventually, the material elements may break into separate segments. Diffusion also occurs everywhere along the material interface to mix at the smallest scales. In general, the flow field for chaotic advection and the resulting mixing is continuous and time dependent.

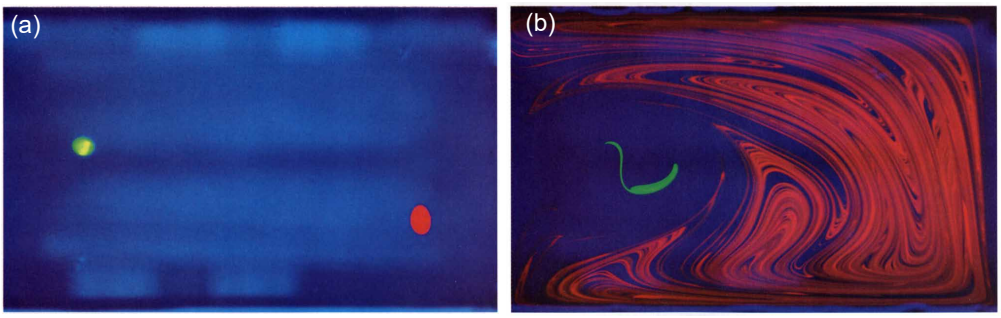

Figure 1.1. Chaotic and non-chaotic regions illustrated by fluorescent dye in a cavity flow. Blobs of green and red fluorescent dye are initially placed in two locations in (a). The top and bottom walls move periodically in a discontinuous manner in the horizontal directions. Because of their initial locations in the flow, red dye is mixed by stretching and folding while green dye is only stretched slightly at the end of 10 periods (b). Reprinted from Ottino [114]. Used with permission of the author.

1.1.3. Mixing in solid systems

Mixing in systems of discrete solids differs from fluids systems mostly because of the unique properties of solid materials. Turbulence rarely occurs, chaotic advection is not sustained, and diffusion only occurs for systems with materials that are flowing or vibrating. However, solid systems can be mixed with discontinuities, for example a deck of cards or a Rubik's cube. In rare cases, discontinuities can be introduced in a fluid system to enhance mixing [153]. For example in a partitioned pipe mixer, fluid flow is separated into two parts by helically twisted plates, then joined together but quickly divided again through a subsequent separator (helically twisted plate) perpendicularly placed [48, 82, 91]. However, discontinuities can occur naturally in solid systems. In addition to commonplace systems like a deck of cards or a Rubik's cube, in the continental crust near continental boundaries, a mechanism called thrust-faulting includes both discontinuities and stretch-and-folding in mountain-building processes, where crust layers break and fold on top of other layers [12].

To understand the role of discontinuities in solid mixing, consider a simple case, shuffling a deck of cards. The deck can be first divided into several smaller decks, and the sequence of these smaller decks is rearranged. Usually, this is done by splitting the deck into two smaller

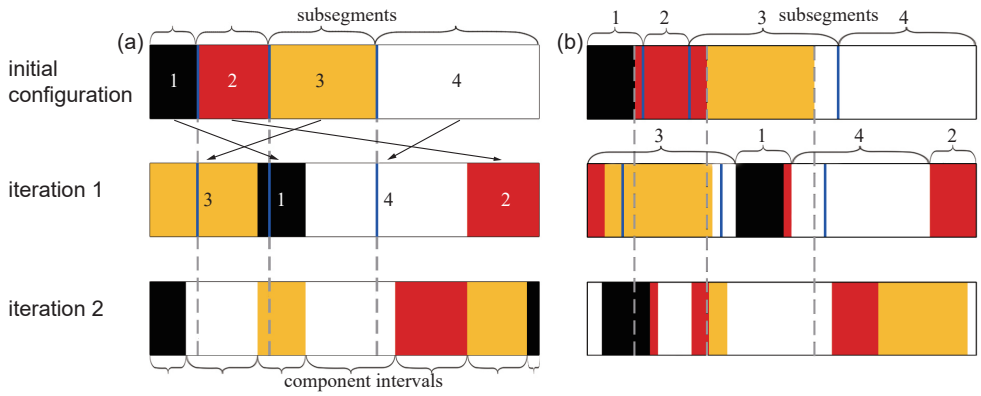

Figure 1.2. Illustration of the first two iterations of an IET for the initial conditions four subsegments of length ratio 1.5 (different colors). Dashed lines indicate exact cut locations. Cut locations (blue solid lines) can be made at the same location (a) or varied (b). Adapted from Yu et al. [170] with permission of World Scientific Publishing Co., Inc.

decks and interleaving the cards in the two smaller decks. In general, this process is referred to as "cutting-and-shuffling," based on the fact that the original shape is divided into pieces and rearranged to put it back together. In mathematics, cutting-and-shuffling is described using the theory of piecewise isometries (PWI) [51, 53] in simple geometries. In its simplest terms, PWI involves cutting an object into two or more pieces and rearranging the pieces to reconstruct the object in its original form. For a deck of cards, the pieces (cards) can be rearranged by cutting-and-shuffling to reform the deck with the cards in a different order.

Application of PWI in a one dimensional system is called an interval exchange transformation (IET) [50], where a line segment is repeatedly cut into short segments which are rearranged. Recent studies have delved into understanding mixing through this framework in simple 1D systems [8, 9, 26, 89, 170]. An example IET is illustrated in Fig. 1.2 (a). A line segment consisting of four colors corresponding to labels 1, 2, 3, and 4 is cut at the initial subsegment boundaries indicated by solid blue lines. The subsegments are then rearranged according to the permutation ($\Pi([1234]) = [3142]$) such that the yellow subsegment is placed on the left, followed by the black, white, and red subsegments. In the second iteration, the cuts (solid blue lines) occur at the same locations coinciding with the original

subsegment boundaries indicated by the gray dashed lines. At the end of two iterations, the line subsegment is slightly mixed as the original four subsegments are cut into seven component intervals and rearranged. This process can be repeated for any desired number of iterations. In most cases, dynamics of IETs are periodic (with the exception of segments having irrational length ratios), meaning the initial condition is recovered periodically after a certain number of iterations. The example in Fig. 1.2(a) is a standard construction of an IET system where cuts occur at the exact same locations and the permutation order is the same for every iteration. Since uncertainty is relevant in practical mixing systems, the effect of uncertainty in cut locations can be studied to understand its relationship to the mixing dynamics of the system. As illustrated schematically in Fig. 1.2(b), cuts can be made at locations with some variation (smaller than 1% of the total length but substantially exaggerated in the figure). The initial configuration of the line segment is the same as in Fig. 1.2 (a) with four colored subsegments, but they are cut at blue solid lines that differ slightly from the original subsegment boundaries (dashed gray lines). The cut locations also vary from iteration to iteration, which enhances mixing in certain protocols. This variation in cut locations in an IET on the mixing is the topic of Chapter 3 of this dissertation. Compared to IETs, the study of PWI in 2D planar systems are scarce [61, 6, 53, 153], and even more so in 3D systems due to increasing difficulty in computation.

The difference between stretching-and-folding and cutting-and-shuffling is illustrated by comparing mixing efficacy of a square in Fig. 1.3. A very simple example of stretching-and-folding is Smale's horseshoe map, where a piece of "dough" is repeatedly stretched into a strip and folded in half onto itself. The mixing of the horseshoe map process can be easily illustrated by the baker's map in Fig. 1.3 (a) (it retains the stretching-and-folding of the horseshoe map while avoiding complex dynamics at the ends). A square shape consisting of equal areas of light gray and dark gray is first stretched into a rectangular shape while preserving the total area. The shape is then cut in the middle indicated by the dashed vertical

line. The two halves are then stacked together to reconstruct the square shape. Since each half consists of two long stretched strips of light gray and dark gray, the reconstructed square now has four distinct color regions alternating in light gray and dark gray. This process effectively produces an increasing number of striations with repeated applications. The baker's map produces strong mixing by stretching and folding that is characterized by exponentially growing interfacial area per unit volume.

In comparison, the cutting-and-shuffling process is illustrated by mixing the same square in Fig. 1.3(b). The square is cut into several pieces indicated by dashed cutting lines, then rearranged according to the number labels into a square again. The mixing depends heavily on the number of cuts, and the permutation (reordering of the pieces). After two iterations, some pieces still occupy large areas, while at the same time, there are pieces that are finely cut; this is not optimal mixing. In the best case scenario for cutting-and-shuffling, the interfacial area only increases polynomially [78]. Interestingly, in the first two iterations, cutting-and-shuffling may produce comparable mixing to stretching-and-folding depending on the protocol.

In practice where mixing efficiency in a short time is desired, a combination of cutting-and-shuffling and stretching-and-folding may yield the best results. In fact, such processes readily occur for fluid flows with valves [76, 63, 146, 148], yield stress materials [111, 93, 15, 11], geological faults [12], as well as splitting and recombining droplets [68, 140]. The mixing and transport of combined cutting-and-shuffling with stretching-and-folding is examined in detail for the PWI-based mathematical for the tumbler flow considered in this dissertation in work by Smith et al. [149]. In fact, in this dissertation, I show that the skeleton of granular mixing in a 3D tumbler is defined by cutting-and-shuffling, but it is modified by stretching that occurs as part of the process [173].

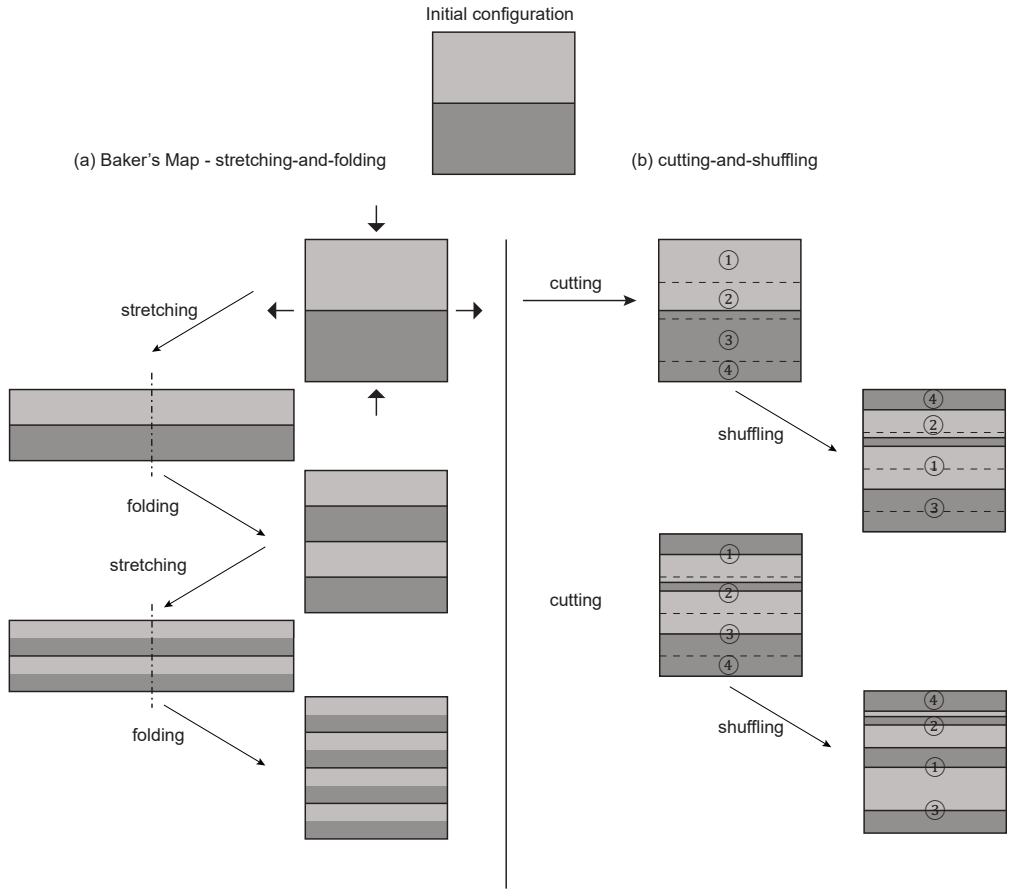

Figure 1.3. Comparison of mixing by (a) stretching and folding in a baker's map and (b) cutting-and-shuffling using an interval exchange transformation (IET). Initial configuration is a square with distinct species in the upper and lower halves. Adapted from Christov et al. [23] with permission of AIP publishing.

1.2. Mixing granular materials

1.2.1. Granular materials

Among various solid systems, granular materials is one of the most important topics in industry. Vast amounts of materials in granular form are processed daily, and the energy consumption of granular material processing has been estimated to be about 10% of energy produced globally [35]. The manufacture of many products includes processing steps that involve mixtures of granular materials of various species with various physical properties. The goal is usually to mix them efficiently and keep them mixed. For example, powder

blending is essential in pharmaceutical manufacturing to ensure the proper composition of tablets. A tablet is usually a compressed mixture of at least two powder ingredients: an active pharmaceutical ingredient (API) and an inactive filler material to add volume, allow compression of the API into a tablet, or to aid in processing. However, the proper ratio of active to inactive ingredients is crucial. Too much or too little of the API in a tablet can cause great harm to an individual via either overdose or inadequate medication to be medically effective. In other applications, mixing is found in processing of food grains, dry chemicals, polymer pellets, and mineral ores.

What is a granular material? Simply put, it is a collection of a large quantity of macroscopic particles. Though individual particle interactions can be simply determined by Newton's Law of motion, extending this approach to predict collective behaviors of millions of particles or more turns out to be quite challenging. Macroscopically, granular materials can exhibit behaviors that are gas-like, liquid-like, and solid-like [70, 4]. For example a pile of sand is at rest (solid-like) when the slope is less than a critical angle called the angle of repose. The grains of sand on the pile are held in place by frictional forces as well as steric effects (normal forces pertaining to conformations). When the slope of the pile exceeds the angle of repose, grains start to flow down the surface (liquid-like), but only on the surface while the base of the heap remains fixed in place. As the material is further dilated such that only occasional binary contacts occur as might occur during strong vertical vibration or rapid flows, the behavior is gas-like. In practice, all three regimes may even coexist at the same time, or transitions between them may occur quickly depending on how the system is forced.

For granular materials under terrestrial conditions, the temperature energy scale, $k_B T$, is negligible compared to the potential energy scale, mgd, of a single particle (the ratio is of $\mathcal{O}(-12)$) [70]. In other words, a granular system can only be agitated with external forces, not thermal input. Moreover, interactions between particles are dissipative and collisions are

inelastic. This means, the kinetic energy of a granular system decreases to zero when there is no external driving. For granular materials to flow, energy must be introduced continuously, for example by rotating a tumbler or by pouring grains. The state of a granular system also depends on the history of how it is forced. For example, the angle of repose of a sand pile just before the sand flows and right after flow ceases depends heavily on how the pile is formed. This is also obvious in that the "density" or packing of particles significant varies when the system undergoes tapping. For example, a box of breakfast cereal may be completely full when prepared at the factory, but over the course of transportation and handling many tapping events cause the cereal to settle to a smaller overall volume. Thus, the collective behavior of granular materials cannot easily be predicted based only on traditional individual particle interactions [35].

1.2.2. Practical mixing challenges

Given how important granular materials are, it is surprising that the design of industrial machinery and processes for mixing granular materials is all too frequently based on empirical understanding with only incremental improvements after costly damage, processing problems, or failures. For examples, workers in many industries, including pharmaceuticals, often use brute force such as banging a sledge hammer on the side of a hopper to keep a hopper unjammed for material discharge [73, 156]; hundreds of industrial and farming silos (tall cylindrical grain storage units) fail to some degree in the United States each year [32]; and the ubiquitous V-blender mixing device commonly used in industry often yields poor mixing despite having been employed for decades. It was estimated in 1989 that costs related to poor mixing amount to between $1 billion and $10 billion in the US chemical industry alone [123].

Much of the work in this dissertation focuses on mixing in tumblers. Several common mixer designs for non-cohesive free-flowing granular materials are shown in Fig. 1.4 [14]. In

all cases, the tumbler is partially filled so the material inside can freely flow as the tumbler rotates. Cylindrical tumblers are the easiest equipment to use [Fig. 1.4 (a)], but often do not accomplish effective mixing because the flow of the material in the tumbler is quite simple. A double-cone mixer uses shear and diffusion [Fig. 1.4 (b)]. Unlike the cylindrical tumbler, the double-cone geometry results in a fairly complex flow of the material inside as it rotates, which often promotes mixing. The V-blender takes advantage of its geometry to induce diverging and converging flow in the axial direction while only rotating about a single axis [Fig. 1.4 (c)]. The granular material flow is even more complex than the double cone blender. This makes the V-blender popular in industrial processing. A lab-scale multi directional tumbler, Turbula ®, shown in Fig. 1.4 (d), is mounted to two rotation shafts at the two ends so that the container moves in alternating pulsating motions in an "∞" manner [97, 99]. The complexity of the flow and the multi-axes rotation motion enhances mixing in the tumbler. As is evident from the examples in Fig. 1.4, the complexity of tumbler geometry or system construction (including rotation axes) on one hand improves mixing, but on the other hand, it poses challenges to construct a universal theoretical framework for granular mixing in tumblers. As a result, the design and application of such tumblers is often ad hoc.

1.2.3. Segregation of granular materials

Adding more complexity to the picture is the tendency to de-mix for granular materials that vary in physical properties, including density, size, shape, or surface roughness. In many other engineering systems where temperature has a significant effect on its energy, agitation of a system generally results in an increase in entropy, which normally leads to mixing [70]. When a granular system is subject to vibration or shear, components can spontaneously separate, called "segregation," into spatially distinct regions with the details depending on the specific flow field and system state [116, 134, 90]. This unique feature of heterogeneous granular materials leads to fascinating natural phenomena, as well as technical challenges

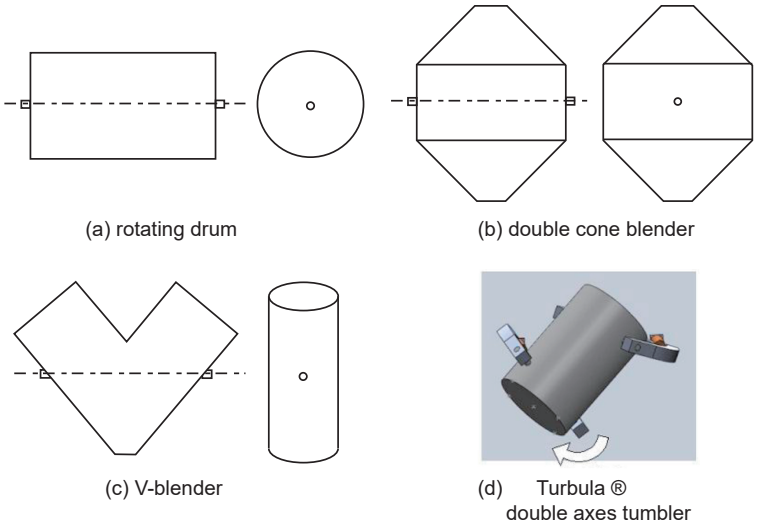

Figure 1.4. Schematics of blenders used in industry: rotating cylindrical drums (a), double cone blenders (b), V-blenders (c), and a device called Turbula ®(d). The axis of rotation is the horizontal dashed line in (a-c). (a-c) Reprinted from Bridgwater [14] with permission ©2012 Elsevier. (d) Reprinted from Mayer-Laigle and Berthiaux [99] with permission ©2015 Elsevier.

in industry. Granular segregation occurs during handling of granular materials including transportation through pipes, mixing in rotary containers, and when filling and discharging silos and hoppers. Segregation in these situations can undo mixing and degrade product quality and performance, which can be disastrous, for example, for poorly mixed ingredients in pharmaceutical tablets.

Segregation in granular systems has been studied intensely over the past several decades. Generally, in a size-bidisperse system, small particles find voids opened up beneath them as particles dilate due to flow or vibration so they percolate downward to the bottom of the container or flow. As a result, large particles are pushed upward toward the top of the material. This phenomenon has been studied extensively both experimentally and theoretically in a number of canonical flow geometries including chutes [135, 33], quasi-two-dimensional (2D) bounded heaps [40], quasi-2D tumblers [67, 83], and cylindrical tumblers [176, 3]. In chute flows that transport granules, size-bidsperse materials segregate into distinct layers. In another example, the pile build-up process in filling silos can be simplified into a quasi-2D

bounded heap [41, 139]. A mixed feed at the peak of the heap results in particles deposited on the heap in a segregated pattern where small particles accumulate in the upper portion of the heap closer to the feed location, and the periphery is mostly occupied by large particles because they flow further down the heap after having segregated upward in the flowing layer to the surface.

A rotating cylinder is a canonical system used to study mixing of granular materials in tumblers. Gravity-driven free surface flow occurs similarly to flows in chutes and bounded heaps, but since materials are confined spatially in tumblers, the flow field is time-periodic, which results in complex flow behaviors. Particles repeatedly pass through the thin flowing layer at the free surface as the tumbler rotates. Therefore, segregation in the flowing layer is enhanced with an increasing number of rotations, which can lead to a variety of segregation structures, as described in the next section. Because of the significant width of the cylinder compared to quasi-2D systems, there can also be significant lateral/axial transport of particles in rotating cylinder flows that result in unusual segregation patterns when a heterogeneous material is used [176, 3, 22, 66, 128].

Thus, mixing of heterogeneous granular materials in tumblers is a two-fold problem. First, even without considering segregation, mixing different species that have the same physical properties but differ in some other way (for example, color) in a tumbler depends heavily on the flow. Resolving mixing dynamics in such a space-time coupled flow system is the first step to understanding mixing of granular materials. Second, spontaneous segregation of particles having different physical properties such as size or density occurs simultaneously, often offsetting the mixing. Interactions between segregation and the complex flow dynamics becomes important: this is the focus of this dissertation.

1.3. Understanding granular segregation and mixing

The unique properties of granular flows have limited the study of an overarching framework for transport and mixing compared to liquids. In liquid flows, the length scale of molecule interactions and microscopic properties is much smaller than the length scale of macroscopic deformation [56], so that liquid flows can be described from a continuum perspective. However, the difference in scale between discrete particle interactions and collective flow in granular materials is much narrower [59]. This narrower difference for granular materials contributes to the difficulty of deriving fundamental governing equations, analogous to the Navier-Stokes equation for fluid flows. In particular, such a continuum description depends heavily on a mesoscale understanding of the segregation process. Nevertheless, the continuum approach has been used in some cases to model granular flow in a dense state that is similar to fluid flows [70]. Various attempts to describe the mixing and segregation of granular flows combine different tools including continuum descriptions, experiments, and discrete element method (DEM) simulations, a computational approach similar to molecular dynamics.

Discrete models [36, 92, 137] and continuum models [85, 38, 67, 96, 86] both have been used to model surface flows of granular materials in tumblers and other geometries. They both provide important insights but at the same time have their own limitations and domains of applicability. In some cases, a continuum model may work better than a discrete model and vice versa. Discrete models are often used where particle-particle contact or particle-wall contact plays an important role in determining macroscopic behaviors. For example, discrete models are useful for surface flows of cohesive particles, and considering surface roughness of particles, or the effect of wall roughness in long cylindrical tumblers. More importantly, DEM simulation results offer information that is not easily accessible from experiments, including local values of the velocity and concentration of particles. In this dissertation, DEM simulations are used to gain insight into particle motion below the visible portions

of the flow and obtain important surface flow information including exact particle locations and their velocities to be used in a continuum model (Chapter 6). One limitation of DEM simulation is the enormous expense of computation power and time, especially for large scale studies of industrial processes. Even though the simple idealized tumbler flow in this dissertation considers around 10^5 particles, a simulation typically still takes 1-2 days in highly parallelized GPU (graphical processing unit) enabled DEM simulations. Detailed discussions of various force models for particle interactions in the DEM simulation and implementation of GPU computations can be found elsewhere [69].

Continuum models can be much faster to solve than discrete models and have the additional advantage of providing physical insight. In systems where details of the particle-particle interactions do not influence the flow or are not a concern, continuum models can be very attractive. When considering dependence of mixing behaviors on system parameters, continuum models also offer opportunity for insights that can be generalized beyond a single specific simulation. Moreover, continuum models can utilize information obtained from experiments and DEM simulations to generate a broader understanding of the underlying physics of the flow or segregation [41]. As will be demonstrated later in this section, using a continuum model in conjunction with dynamical systems approaches provides flexibility to consider different system parameters and also a more fundamental understanding of mixing. In the remainder of this section, examples of rotating cylindrical tumblers and quasi-2D tumblers are used to introduce some universal features of granular tumbler flows and methods to study them, including flow kinematics, continuum descriptions, segregation, and dynamical systems approaches. Then, the connection of a quasi-2D tumbler to a fully 3D tumbler will be discussed.

1.3.1. Flow kinematics in rotating tumblers and continuum descriptions

Tumbler flows can be quite complex. The flow of granular particles in a partially filled tumbler changes dramatically with rotation speed. In a long rotating cylinder partially filled with particles, tumbler flow can be classified into several regimes by the ratio of centripetal acceleration to the gravitational acceleration, the Froude number $Fr = \omega^2 R/g$ [132, 102]. Different flow regimes are illustrated schematically as viewed through transparent tumbler sidewalls, shown in Fig. 1.5. At low Froude number, the flow consists of periodic avalanches [Fig. 1.5(a)]. The bed of particles stays static until the tumbler rotates to β_m, the angle of marginal stability. Then, particles relax by flowing down the surface until the bed reaches a new surface with an angle $\beta_s < \beta_m$, the static angle of repose. The avalanches happen intermittently as the tumbler rotates. As Froude number increases, continuous or cascading flow occurs in a lenticular flow region with the highest velocity at the surface Fig. 1.5(b). The flow has a steady flat free surface at an angle β_d (the dynamic angle of repose) to horizontal. Particles enter the flowing layer on the left from the bed of particles in solid body rotation with the tumbler. They flow down the free surface rapidly and then deposit into the bed to begin solid body rotation again. The angles of repose (β_m and β_s) [35, 117, 133] varies as a function of granular material properties including size [112], surface roughness [129], as well as tumbler wall effects [37, 112], and rotation speed [112, 132, 169]. At a higher rotation speed, cataracting flow occurs [Fig. 1.5(c)] in which particles follow the tumbler wall to a much higher location at the upstream end of the flowing layer and sometimes are thrown off, resulting in an S-shaped free surface. With a high enough rotation speed at a Froude number exceeding approximately 1, the flow becomes centrifuging [Fig. 1.5(d)], where particles are centrifuged outward to the tumbler wall and rotate as a solid body in a ring [102, 101]. The avalanching regime, has attracted particular research interest to understand the unique properties of granular materials transitioning from a static state to a flowing state, but it is not particularly common in industrial flows that motivate the research here. Likewise,

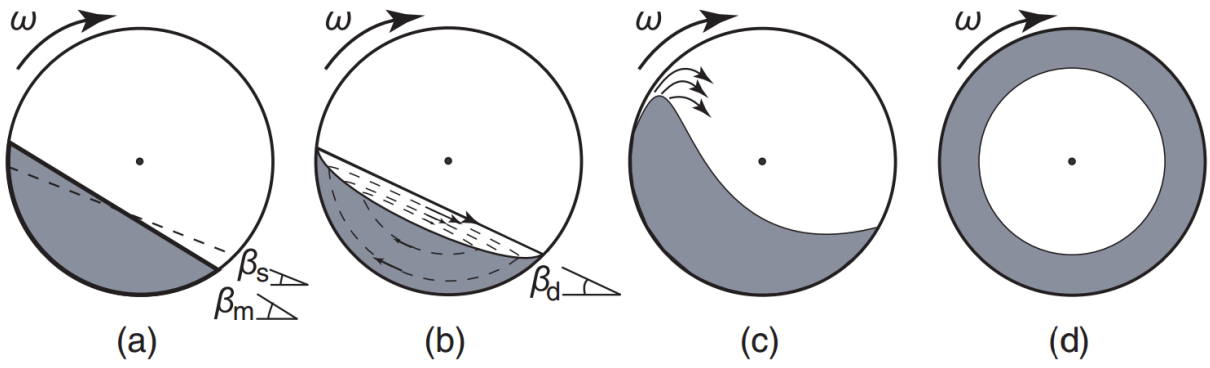

Figure 1.5. Illustration of flow regimes in tumblers: (a) avalanching (intermittent flow), (b) continuous flow/cascading, (c) cataracting, and (d) centrifuging. Reprinted from Meier et al. [101] with permission ©2007 Taylor & Francis.

because the particles are in solid body rotation, the centrifuging regime is of little practical interest. Cataracting flow is quite difficult to characterize, so we do not consider it here. In this dissertation, the focus is on the continuous flow regime [Fig. 1.5(b)], where the gravity driven flow is steady and the free surface is flat.

These observations and analysis of flow in a cylindrical tumbler are provided here because the flow can be considered in a plane perpendicular to the axis of rotation. In other words, the axial flow is so small that it does not significantly alter the overall flow and can be safely ignored. (However, later in this dissertation, I show that there are situations where relatively small axial flows cannot be ignored.) Thus, to simplify the flow, a cylindrical tumbler with a small axial dimension compared to radial dimensions is considered. This disk-like tumbler is called a "quasi-2D" tumbler, since the flow is nearly two-dimensional, confined in the plane perpendicular to the axis of rotation. The quasi-2D geometry allows direct visualization and measurements of the flow through clear endwalls and requires less material than fully 3D systems. Therefore, it is an attractive laboratory system to study details of flow kinematics [17, 28, 85, 84, 67, 83, 112]. Jain et al. measured the velocity profile in the flowing layer of a quasi-2D circular tumbler rotating at a constant speed in the continuous flow regime. Velocities are calculated from optical images of particles from

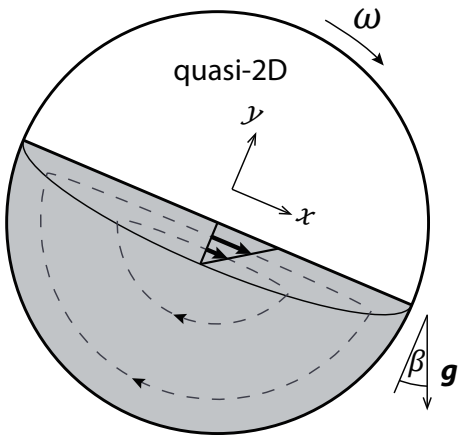

Figure 1.6. Continuum description of granular flow in a quasi-2D circular tumbler rotating at constant speed ω. The flow is modeled as a steady state where the free surface is flat and inclined at an angle of repose β. The flow is described as a constant shear rate flow in the thin lenticular flowing layer and solid body rotation in the fixed bed. Reprinted from Zaman et al.[172] with permission ©2013 American Physical Society.

the clear endwalls using particle tracking velocimetry (PTV) and particle image velocimetry (PIV) methods [71]. The streamwise velocity in the flowing layer varies almost linearly as a function of the flowing layer depth for most of the flowing layer. Near the interface between the fixed bed and flowing layer, the streamwise velocity decreases exponentially toward zero as a function of depth. In attempts to describe the flow with continuum approaches, the flow field can be simplified to a linear velocity profile as a function of depth in a lenticular shaped flowing layer symmetric about the midpoint of its length [101, 24], as shown schematically in Fig. 1.6. The exponential transition near the interface can be neglected because it occurs over a very short distance and the velocity is small enough to have no significant influence on the flow in the continuous flow regime. An incompressible continuum flow model of the quasi-2D circular tumbler can be constructed with a constant shear rate velocity profile in the flowing layer and using mass balance between the flowing layer and the bulk material in solid body rotation below the flowing layer [101, 24]. The continuum model can then be used to model the flow in a granular tumbler.

Studies of granular material mixing and segregation in these tumblers are primarily motivated by the observation that distinct segregation patterns form in mixtures where species vary in size or density. One of the simplest examples that illustrates segregation of particles in tumblers is segregation of size-bidisperse particles in a quasi-2D tumbler with a circular cross section rotated at a constant speed, as shown in Fig. 1.7 [101]. The tumbler is filled to 48% with an initially well-mixed mixture of equal volume large clear particles ($d = 1.11$ mm) and small black particles (diameter $d = 0.35$ mm). Upon rotation (continuous flow regime), the mixture quickly separates (1-2 rotations) into a distinct pattern with a layer of clear large particles close to the tumbler wall and at the free surface (barely visible in the figure), leaving a core of small black particles [Fig. 1.7(a)]. This radial segregation is an example of the granular segregation that can occur in all free surface flows whether, as in this case, driven by percolation (small particles fall into the voids between large particles) or other mechanism such as density-difference-driven buoyancy where light particles rise to the free surface of the flow and heavy particles sink. During flow down the free surface, small particles percolate through voids generated by shear, therefore, pushing large particles to the top of the flowing layer. In the downstream half of the flowing layer, particles reach the interface between the flowing layer and the bulk before depositing into the bulk to continue solid body rotation. Small particles that have percolated to the bottom of the flowing layer reach the interface first, and deposit near the middle of the flowing layer. Whereas, large particles on the top of the flowing layer continues further downstream, and leave the flowing layer closer to the tumbler wall. By repeated passes through the flowing layer, segregation between small and large particles is enhanced after the initial pattern forms in only 1-2 passes.

Segregation in the quasi-2D circular tumbler has been studied using a model incorporating the advection of the mean flow, percolatation-driven segregation, and diffusion due

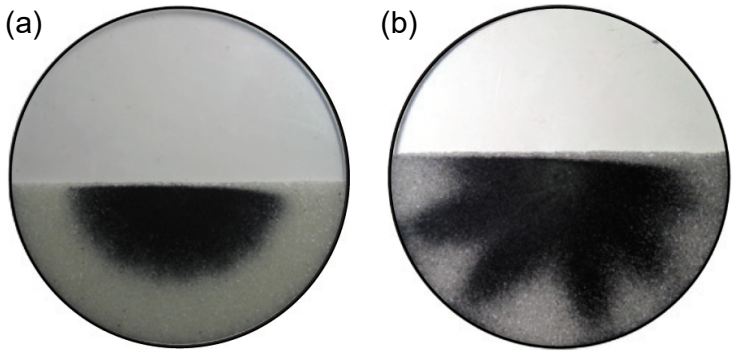

Figure 1.7. (a) Radial segregation of an initially well mixed mixture of 1.11 mm (clear) and 0.35 mm (black) diameter particles in a quasi-2D circular tumbler filled to 48% of its total volume. (b) Radial streak segregation pattern in the same tumbler when it is 58% full. The tumbler has a diameter of 200 mm and thickness of 6 mm. Reprinted from Meier et al. [101] with permission ©2007 Taylor & Francis.

to particle collisions [138]. The model is formulated based on an advection-diffusion continuum transport equation with an added term for segregation that determines concentration of each particle species as a function of space and time. This method has previously been shown to capture the segregation process in various geometries including plug, annular, and chute flows, where the flow field is relatively simple [159]. Specifically, two dimensionless groups, the ratio between advection and diffusion as well as ratio between advection and segregation, have been shown to play important roles in determining final segregation patterns [41, 138]. Schlick et al. combine this segregation model with the continuum description of the kinematics in the flowing layer in the quasi-2D circular tumbler to demonstrate quantitative agreement with DEM simulations and qualitative agreement with experiments [138]. Although this method is useful in predicting segregation and provides fundamental insights into the mixing and segregation, it can be challenging to implement this model for more complex flow field dynamics often encountered in 3D mixing systems.

1.3.2. Segregation patterns and dynamical systems approach

Consider here an example of a more complex segregation pattern in the quasi-2D circular tumbler. If the tumbler is filled to 58% volume faction with initially mixed equal volumes of small black particles and large clear particles, a lobed segregation pattern occurs as shown in Fig. 1.7(b). Similar lobed patterns can occur when the rotation speed is slowed into the avalanche regime or modulated at an integer multiple of the rotation speed [67, 83, 44, 72]. Similarly, lobed patterns have been observed in quasi-2D tumblers having a polygon shape because the flow becomes time-periodic due to the polygonal tumbler geometry[100].

To understand these intricate patterns, dynamical systems approaches have been utilized to analyze mixing as a result of interaction between segregation and the chaotic dynamics of the underlying flow field [100]. In one instructive example [Fig. 1.8], a square quasi-2D tumbler is initially filled with a uniform mixture of small ($d = 0.3$ mm) black glass particles and large ($d = 1.2$ mm) clear glass particles. The tumbler is rotated at constant angular speed ($\omega = 1.44$ rpm) so that particles continuously flow down the free surface (rolling/cascading regime [102, 62]). After several revolutions, shown in Fig. 1.8(a), the small black particles accumulate in the two lobes, which extend from the core toward the two corners, while large clear particles occupy the periphery of the tumbler.

The lobed pattern comes from the time-periodic nature of the flow due to the tumbler geometry. That is, the surface flowing layer varies in length periodically from the position shown in Fig. 1.8(a) to a position where it spans the diagonal of the tumbler. This lobed pattern matches quite well with the non-chaotic regions on the diagonal in the Poincaré section map, shown in Fig. 1.8(b). A Poincaré section map is a stroboscopic mapping [152] that captures the time-periodic nature of the flow by recording the positions of tracer points after each period (one quarter revolution in this example). Chaotic regions are made clear by scatter of points in the domain, while non-chaotic regions are shown by points trapped in islands on the diagonals (closed loops) [100]. The correspondence between the lobes of small

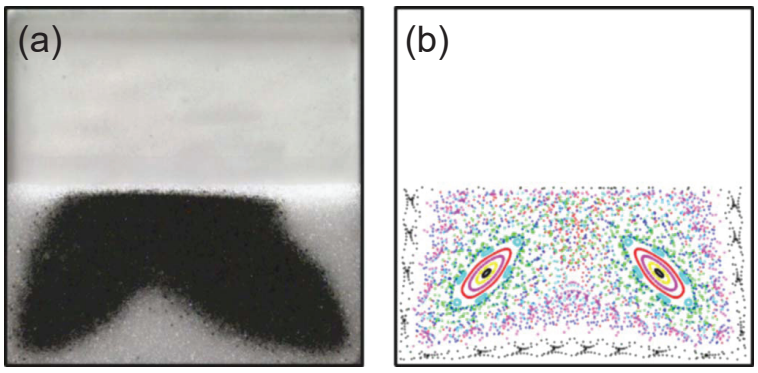

Figure 1.8. (a) Segregation experiment in a half-full square tumbler with 40% small (0.3 mm) black particles and 60% large (1.2 mm) clear particles by weight. Steady-state pattern after ten clockwise revolutions of the tumbler at 1.44 rpm. (b) Poincaré section of a half-full square tumbler derived from model of flow kinematics. Reprinted from Meier et al. [100] with permission ©2006 American Physical Society.

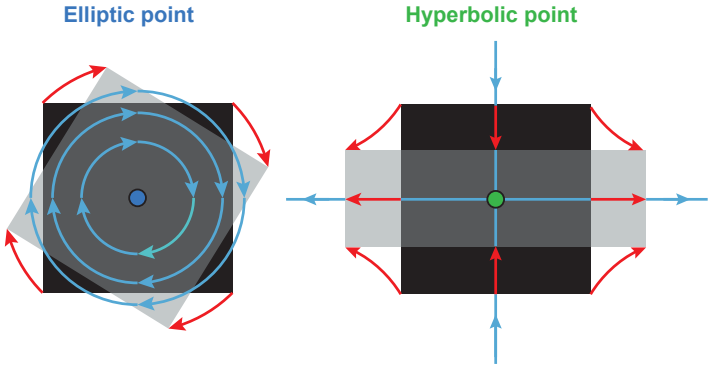

Figure 1.9. Fixed points categorized by surrounding flow shown in stroboscopic map. The black square around a fixed point is deformed along the pathlines of red curves into the gray shape. Blue curves and arrows indicate local stroboscopic motion. Elliptic fixed point is surrounded by rotational movement (a). Hyperbolic fixed point experiences compression and stretching in two directions (b). from Meier et al. [101] with permission ©2007 Taylor & Francis.

black particles in the experiment and the non-chaotic regions on the diagonal in the Poincaré map results from the interaction between segregation and the flow dynamics. The key point here is that the points are advected according to a continuum model formulated purely from the flow kinematics without consideration of segregation. Yet the correspondence between the Poincaré map and the segregation pattern is quite clear.

Before considering how the dynamical systems features are related to mixing, it is helpful to explain some of the features of the Poincaré map in Fig. 1.8(b). The closed loops on the diagonals shown in the Poincaré section [Fig. 1.8(b)] are a signature of periodic non-chaotic regions (or regular islands) [113, 152]. The center of such a non-chaotic region is an "elliptic" fixed point, as shown schematically in Fig. 1.9(a). A tracer point at this location, denoted as the blue dot in the center, returns to the same location after every period (or some multiple of the period) of the flow. The flow in the vicinity of the elliptic point is quasi-periodic, meaning tracer points return to the corresponding closed loop but at a certain angular distance away, depending on system conditions. In phase space, the trajectories become closed loops as shown by blue curves with arrows in Fig. 1.9(a). Orbits surrounding an elliptic fixed point that persist under weak perturbation (remains quasi-periodic instead of becoming unstable or destroyed) are called KAM (Kolmogorov-Arnold-Moser) orbits, and the resulting KAM islands act as barriers to mixing [113]. On the other hand "hyperbolic" fixed point that experiences both compression and stretching is usually associated with mixing. As shown in Fig. 1.9(b), the "hyperbolic" fixed point (green dot) connects two material lines pointing in opposite directions, indicated by blue curves with arrows. The blue trajectory approaching the fixed point in forward time is called the stable manifold, while the blue trajectory leaving the fixed point is called the unstable manifold. The material lines near them asymptotically approach the stable manifold in forward time, but the unstable manifold in backward time. Chaos is created when the stable manifolds and the unstable manifolds asymptotically connect two hyperbolic points (heteroclinic connection) [113]. The Poincaré section does not show the stable and unstable manifolds, because the separation of points on the manifolds grow exponentially with time. Therefore, the chaotic regions appear as a scatter of points. These chaotic regions promote mixing by distributing particles randomly in the chaotic portion of the domain.

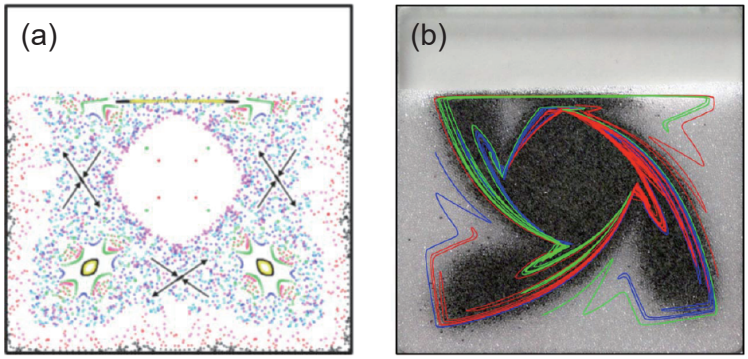

Figure 1.10. (a) Poincaré section in a 75% full square tumbler. The arrows indicate direction of stretching and compression around the hyperbolic points. (b) Unstable manifold of the same system overlaid on an experimental image of a 75% full square quasi-2D tumbler with 30% large clear particles and 70% small black particles. Reprinted from Meier et al. [100] with permission ©2006 American Physical Society.

An example of mixing behaviors influenced by unstable manifolds can be shown in the square quasi-2D tumbler in Fig. 1.10. The continuum model predicts period-3 elliptic fixed points and associated islands where one period is one quarter of the tumbler revolution. At the rotational phase shown in the Fig. 1.10(a), two of the three periodic islands are located in the lower half of the tumbler on the diagonals, while the third is stretched out in the thin flowing layer. Hyperbolic points are shown by arrows indicating the directions of stretching and compression around them. The unstable manifolds originating from these hyperbolic points are shown in Fig. 1.10, overlaid on an experimental image of 30% large clear particles and 70% small black particles. Similar to the 50% full case in Fig. 1.8, the small black particles accumulate at the periodic non-mixing islands on the diagonal and near the flowing layer. The shape of the lobed pattern follows the structure of the unstable manifolds closely. Similar unstable manifolds have been found in the BST flow for period-1 hyperbolic points, and their association with non-mixing behaviors are discussed in [24]. In this dissertation, stable and unstable manifolds are calculated for several protocols and their connections to mixing are discussed in Chapters 5 and 6.

The intent of using dynamical systems approaches is to determine whether the system approaches an equilibrium state, repeats in cycles, or produces chaotic behaviors and regular behaviors at the same time [152]. It has been applied to fluid mixing [5], particularly in regard to chaotic advection. Chaotic advection, characterized by stretching and folding, has been studied in microfluidics [151], geophysics [165], composites processing [74] and food processing [104]. Deterministic chaos or "chaos theory" aims to understand the typical chaotic flow structures and how they became chaotic [115]. It also provides insight into the relationship between these structures and the actual flow [115]. The correspondence between visualization of chaotic advection in incompressible 2D time-periodic flows and 2D area preserving maps of dynamical systems has inspired researchers to merge the two areas [118, 166]. The dynamical systems perspective excels at providing a theoretical and computational framework that offers a fundamental understanding of mixing that can be use to describe phenomena in various systems even with different length and time scales. As shown in the example of the square quasi-2D tumbler, some of these dynamical systems approaches including computation methods of finding the structures and experimental visualization methods are useful for understanding mixing in granular systems as well. Thus, this dissertation sets out to look for similar connections between the dynamical systems approaches and the mixing of granular materials in a 3D tumbler system.

1.3.3. From quasi-2D tumbler to 3D tumblers

Examples of quasi-2D tumblers have demonstrated the complexity of tumbler flows, but also provide insights for understanding the 3D tumbler flows. A simplified continuum model for 3D tumbler flows has been proposed by decomposing the 3D geometry into many 2D slices [101, 24]. An example of describing a 3D spherical tumbler in terms of many non-interacting 2D slices is shown schematically in Fig. 1.11. The velocity profile based on the quasi-2D circular tumbler shown in Fig. 1.6, is parametrized in the axial direction with varying radius

and length of the flowing layer. Justification of this simplification comes from the observation that velocity in the axial direction is small compared to streamwise velocity [127]. Zaman et al. have also measured the axial drift of particles near the tumbler wall to be about half a particle diameter (about 2% of tumbler diameter) per pass through the flowing layer [172]. Using 2D slices provides a simple approach to explore mixing in 3D tumbler flows in more complex geometries. However, any small axial displacements or velocities inherent to the 3D geometries can be amplified through repeated tumbler rotations. Several studies have demonstrated that transport in the axial direction is critical in long-term flow patterns observed in systems with granular materials of two or more species [176, 66, 22, 3, 65, 20]. This is also shown to be the case in Chapter 6 of this dissertation. Moreover, contact of particles with the endwalls can induce slow axial circulations that transmit of particles axially in rotating cylinders [128, 19]. The effect of contact between particles and tumbler walls can also result in non-trivial segregation patterns that can invert when mixture composition or tumbler wall roughness changes [18, 34, 45].

In a 3D tumbler flow, there are many questions analogous to those related to the phenomena in quasi-2D tumblers. What are the dynamical systems structures in 3D tumbler flow? How are these structures related to mixing or segregation and why? When tumbling a mixture of segregating particles, what will happen? How is segregation affected by chaotic and non-chaotic regions of the flow? Does the continuum model based on quasi-2D kinematics still work? To begin answering these questions, we first define several aspects of 3D tumbler flow in the next chapter.

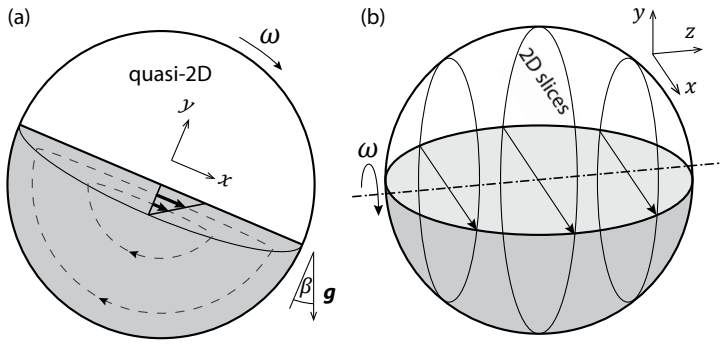

Figure 1.11. (a) Schematic of flow kinematics in a 2D slice consists of constant shear rate flow in the flowing layer and solid body rotation in the bulk. (b) Decomposition of a 3D spherical tumbler into 2D slices. Reprinted from Zaman et al. [172] with permission ©2013 American Physical Society.

CHAPTER 2

Three-dimensional spherical tumblers

SUMMARY

This chapter introduces the model system studied in this dissertation, the bi-axial spherical tumbler (BST). The spherical tumbler is the simplest 3D tumbler geomety that serves as a prototype for understanding the mixing and segregation of granular materials. With bi-axial protocols, the resulting flow represents a simple model for time-periodic flows that occur in 3D tumblers used in industry. In this chapter, the BST is defined and past work related to BST reviewed, including a continuum description, dynamical systems analysis, experimental results, and the cutting-and-shuffling framework of the BST. An outline for the remainder of this dissertation is provided at the end of this chapter.

2.1. Bi-axial spherical tumbler

This dissertation focuses on what is arguably the simplest geometry for 3D mixing — a sphere. Consider the problem of how to mix granular materials that only differ in color in a sphere, as shown in Fig. 2.1. When the sphere is rotated continuously around a single horizontal axis [Fig. 2.1(a)], only slow diffusion occurs. If, however, the rotation is stopped, and the tumbler is rotated about a perpendicular axis, and these rotations are repeated alternately [Fig. 2.1(b-d)], it seems likely that the mixing would be improved. The seemingly simple additional rotation about a second axis introduces time-periodic complex flow. Spherical tumblers are not used in industry, but an idealized 3D spherical tumbler offers a simpler path to understanding the fundamentals of mixing in 3D granular flows.

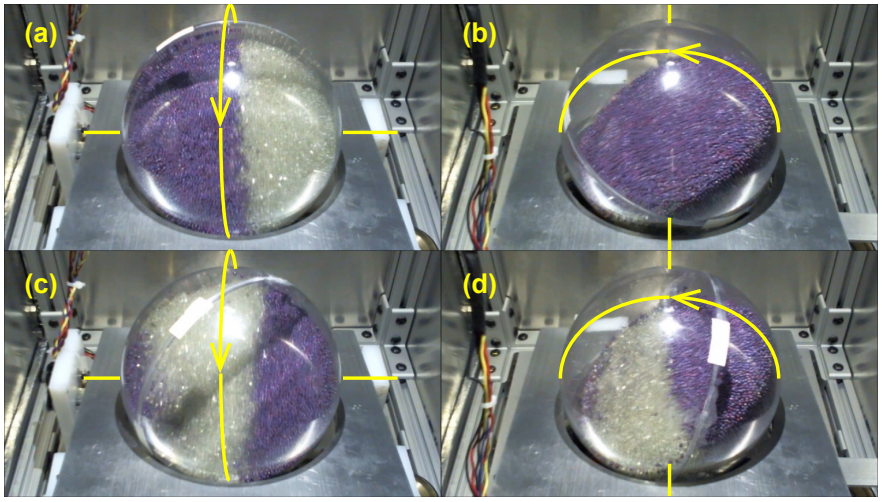

Figure 2.1. Tumbling a spherical tumbler ($D = 14$ cm) half-filled with equal volumes of purple and clear particles of the same size with a initial interface vertically perpendicular to the page with arrows indicating rotation direction around axes: (a) Only weak axial diffusion near the interface drives mixing for single axis rotation; (b) Introduction of a second rotation axis; (c,d) Repeated rotations about two axes. (See Appendix B for details of the apparatus.)

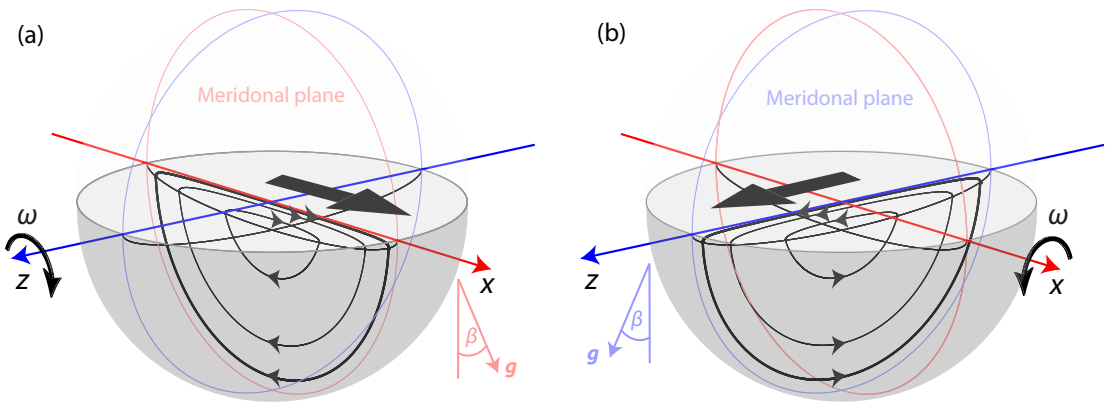

Figure 2.2. Bi-axial spherical tumbler (BST) flow consists of two rotations about two perpendicular horizontal axes per iteration. The tumbler is rotated about (a) the z-axis for θ_z, and then about (b) the x-axis for θ_x, at rotation speed ω. A normal vector to the free surface is offset from the direction of gravity by the angle of repose β. Streamlines are shown on a 2D slice. Adapted from Zaman et al. [173] ©2018 with permission of Springer Nature.

The focus of this dissertation, the spherical tumbler rotating alternately about two orthogonal horizontal axis, i.e. the bi-axial spherical tumbler or BST, is shown schematically in Fig. 2.2. The spherical tumbler is half-filled with dry granular materials and rotated alternately about two orthogonal horizontal axes, here the z- and x-axis by angles (θ_z, θ_x) beyond the angle of repose β. In Fig. 2.2, the free surface and direction of gravity are offset by β for purposes of visualization. In general, a mixing protocol is denoted by a triplet $(\theta_z, \theta_x, \gamma)$, where γ is the angle between the rotation axis and is kept constant at $\gamma = 90°$ in this dissertation but can be set to other values [77, 94].

The primary practical challenge in experimentally studying the flow in most granular systems including the BST system lies in the opaque nature of granular materials, which makes it difficult to experimentally probe the flow and mixing dynamics inside the tumbler. For this reason, we use three different approaches to study flow and segregation in the BST system. First, we perform experiments using an x-ray system to track x-ray opaque particles in the flow. Second, we develop and use a continuum model approach to explore the dynamical systems aspects of the bi-axial tumbler flow and connect those aspects to PWI approaches. Third, we use discrete element method (DEM) simulations in which the motion of tens of thousands of interacting particles are tracked computationally in the flow. Together, these approaches allow the investigation of the underlying physics of the mixing, segregation, and segregation pattern formation in the BST system.

2.1.1. Previous work on BST flow dynamics

Meier et. al devised a continuum model for BST based on the quasi-2D continuum description [101]. Two-dimensional slices normal to the z (axial) direction are described with the same model for quasi-2D [Fig. 1.11] with the assumption that each 2D slice is independent from the adjacent slices (no axial flow). The flowing layer length and flowing layer thickness of each 2D slice is adjusted according to the axial position of that slice. The description for

rotation about the z-axis is identical for rotation about the x-axis with just a change in the rotation axis. Using this approach, Meier et. al found period-1 elliptic points associated with regions that return to their starting locations every iteration [101], analogous to the elliptic points shown in Fig. 1.8(b) for a square quasi-2D tumbler. Similar to the quasi-2D tumbler, these periodic regions in a BST are assumed to be associated with non-mixing behaviors, while the rest of the domain is generally chaotic and associated with mixing [101].

Continuing the dynamical systems approach, Christov et al. derived analytical expressions for period-1 points for a range of protocols [24]. The periodic fixed points were found to form a curve in the 3D BST flow that pierces hemispherical shells with a range of radii as shown in Fig. 2.3 [24], where the blue line coincides with a curve of periodic elliptic points piercing the hemispherical shell at the center of KAM islands, and the green line coincides with a curve of periodic hyperbolic points. The elliptic fixed points on this curve, when connected, form the center lines of 3D KAM tubes as shown by the magenta structure in Fig.2.4, analogous to KAM islands in 2D dynamical systems [113]. Mixing within KAM tubes is likely to be poor [24], and the boundary of the KAM tube is likely a barrier to mixing between the tube and the remainder of the domain [113], like the boundary of a 2D KAM region. Christov et al. also found and visualized the stable and unstable manifolds of the BST flow, which are signatures of chaotic flows in fluid systems [113]. These dynamical system features are derived purely from the continuum description, but are later shown in this dissertation to capture the underlying flow dynamics of the BST system [78, 77, 173].

The mixing of monodisperse particles in the BST system was explored using the cutting-and-shuffling framework by Juarez. et al. [78, 77]. Experiments using particle species differing only in color illustrated pattern evolution in the BST system with a high correspondence to the BST continuum model as well as the PWI description of BST in the first few iterations. Over a large number of iterations, collisional diffusion and stretching in the

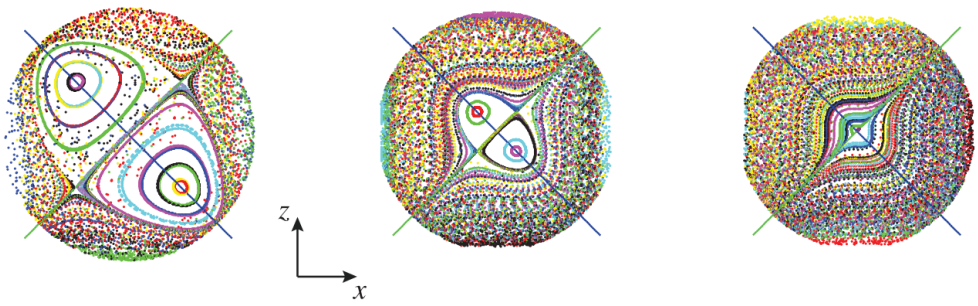

Figure 2.3. Poincaré sections showing KAM islands surrounding elliptic fixed points on hemispherical shells of various radii (decreasing from left to right) for the $(180°, 180°)$ protocol (bottom view). The periodic elliptic (hyperbolic) curve on the diagonal is indicated by the blue (green) line. Reprinted from Christov et al. [24] with with permission of the authors.

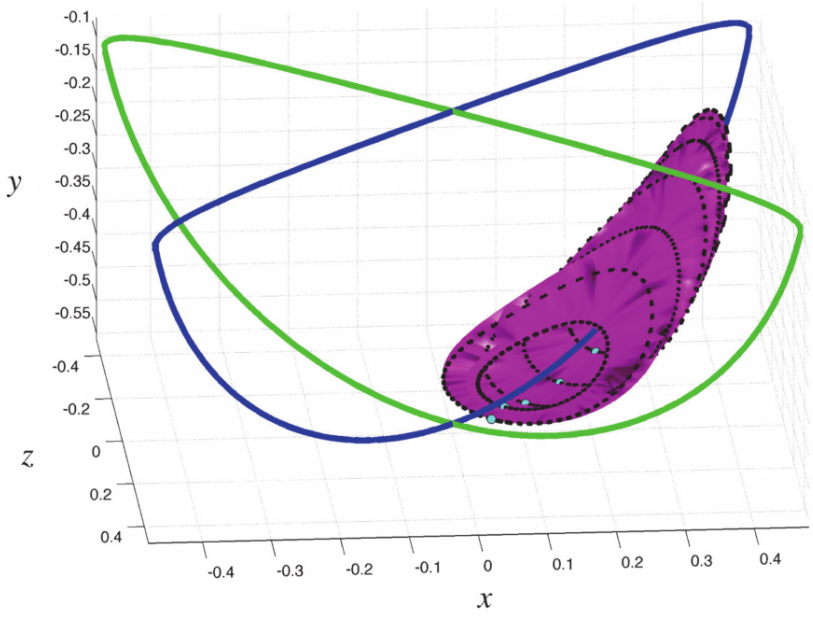

Figure 2.4. KAM tube (magenta) in the BST for the $(180°, 180°)$ protocol surrounding the elliptic periodic curve (period-1) indicated in blue. The green curve indicates the hyperbolic periodic curve. Reprinted from Christov et al. [24] used with permission of the authors.

flowing layer has an increasing influence, making the pattern resulting from cutting-and-shuffling less discernible. The mixing pattern for the colored particles can be traced back to the underlying cutting-and-shuffling framework considering material on a hemispherical shell. This work demonstrates that mixing in the BST flow consists of traditional chaotic

dynamics (stretching) in the flowing layer, but it is built upon the underlying framework of mixing due to cutting-and-shuffling. Again, cutting-and-shuffling alone can produce only polynomial mixing rates [16, 7], but the skeleton of mixing due to cutting-and-shuffling is clear for small numbers of iterations. The application of PWI related to cutting-and-shuffling in such a physical flow has inspired further study of the rich dynamics of the BST PWI [122, 121, 148].

It is important to note in the context of this dissertation that the assumption of negligible axial transport between 2D slices in the continuum model was challenged experimentally by Zaman et. al [172]. Axial drift of particles in a spherical tumbler half-filled with monodisperse particles rotating about a single axis was measured to be about one particle diameter at the surface of the flow for each pass through the flowing layer (small compared to primary flow down the sloped surface). This axial drift was also observed in DEM simulations by D'Ortona et al. [172], and further circulation of particles was illustrated in which particles drift axially toward the poles on the free surface of the flowing layer, and drift back toward the equator when they are submerged in the flowing layer. Curved trajectories of particles suggested the axial transport is primarily a result of the curved geometry of the bounding wall of a spherical tumbler. Although it has been shown that the continuum model predicts tumbler dynamics relatively well [78, 77], the axial velocity will later be shown critical to pattern formation behaviors in the BST flow of particles that segregate (Chapter 5 & 6).

2.1.2. Previous work on segregation

Most studies of segregation in spherical tumblers focused on rotation about a single axis. In a size-bidisperse system, continuous rotation about a single axis leads to a segregation pattern in the form of bands perpendicular to the axis of rotation as shown in Fig. 2.5 [18, 34, 45]. Depending on the composition of the mixture used, tumbler fill level, and tumbler wall roughness, large particles accumulate in a single band on the equator or double bands near

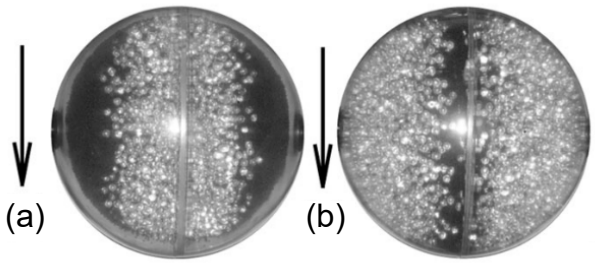

Figure 2.5. Segregation pattern of banding in a spherical tumbler with equal volumes of small black particles (1 mm) and large clear particles (4 mm): (a) Top view of single large particle band on the equator for a 30% full tumbler; (b) Top view of double large particle bands near the poles of a 60% full tumbler. The flow direction in the flowing layer is indicated by the arrow. Reprinted from Chen et al. [18] with permission ©2009 American Physical Society.

the poles. Due to radial segregation, large particles only occupy the bands near the tumbler walls and on the free surface, resulting in a core of small particles underneath. At high fill levels, large particles form two bands, one at each pole, while a single band at the equator occurs at lower fill levels. This transition also occurs at a lower fill level for smaller absolute particle sizes. The curvature of particle trajectories was found to be inversely related to the tumbler to particle diameter ratio, with a small ratio resulting in large particles curving toward the poles. The important observation in this study is that at lower fill levels (30%), a thin layer of small particles are pushed along the upstream tumbler wall above the free surface, and fall off toward the poles, resulting in single banding of large particles on the equator. However, this layer of small particles does not occur at higher fill levels ($\geq$ 50%) because the free surface is nearly perpendicular to the wall. Thus, the large particles drift toward the poles, leading to double banding.

D'ortona et al. investigated the effect of tumbler wall roughness on the transition between the single banding and double banding of large particles [34]. Wall roughness significantly affects the curvature of particle trajectories between small and large particles as well as their axial drift. Rough walls promote less curved trajectories and more axial drift, resulting in double bands near the poles [34]. Both studies [18, 34] indicate that curved trajectories

play an important role in segregation pattern transitions. These results demonstrate that although the axial drift with each pass through the flowing layer may be small in the 3D spherical tumbler flow, it can have a large influence on mixing and segregation in size-bidisperse systems.

An earlier study addressing mixing and segregation in a BST-like flow was published by Gilchrist and Ottino [49], in which the spherical tumbler is constantly rotating about one axis, while periodically rocking about an orthogonal axis. The introduction of rocking around the second axis is in the pursuit of better mixing and it inspired the BST flow [49]. A continuum description based also on non-interacting 2D slices was used to model the flow, although it did not include segregation. A robust single band segregation between size different particle species was observed in experiments that matches the non-mixing KAM islands predicted by the continuum model for several protocols. It was speculated that once the segregation is complete, the system behaves as a single species. Therefore, the continuum model without segregation should be appropriate for describing the system in the steady-state limit. This work on mixing and segregation in a 3D spherical tumbler shows that similar to the quasi-2D square tumbler in Chapter 1.3.2, a continuum model based solely on kinematics predicts the segregation patterns. It also encourages searching for similar mixing and segregation behaviors in the BST flow and developing a deeper understanding of the mechanism driving only one particular particle species into non-mixing regions.

2.1.3. Cutting-and-shuffling in the BST

The BST flow can be viewed through the lens of PWI (cutting-and-shuffling) by focusing on how material is displaced by rotations about alternating axes. Because cutting-and-shuffling is only concerned with discontinuities and rearrangements, the finite thickness flowing layer in physical systems and the model in Fig. 1.6 is simplified as infinitesimally thin ($\delta \to 0$), as shown schematically in Fig. 2.6. As the flowing layer thickness δ decreases, the flowing layer

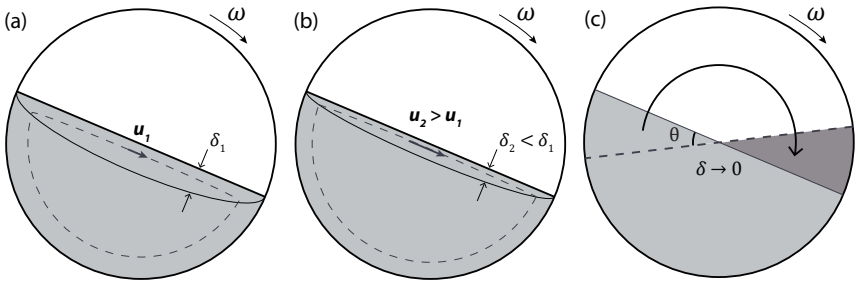

Figure 2.6. Characterization of granular flow in a quasi-2D circular tumbler. Adapted from Zaman [174] as the flowing layer thickness is reduced from (a,b) a finite value to (c) zero in which limit the dynamics are described by PWI where wedges of material are flipped across the rotation axis.

velocity $\vec{u}$ increases. When δ goes to the limit of 0 [Fig. 2.6(c)], the flow is equivalent to instantaneously flipping a wedge over the rotation axis. A wedge having an apex angle of θ (corresponding to θ_z or θ_x) in light gray starting on the left side undergoes a rotation along the arrow and ends at the dark gray wedge shape location on the right. The free surface changes from the solid line into the dashed line.

The situation is analogous in a spherical tumbler except that the wedge of a circle in Fig. 2.6(c) becomes the wedge of a sphere. Furthermore, with an infinitesimal thin flowing layer, the hemisphere is radially invariant. Thus, the PWI for a hemisphere can be simplified to a hemispherical shell. The operation of PWI for the BST is illustrated in Fig. 2.7 for successive rotations about z-axis (a-d) and x-axis (e-h) [122]. The blue boundary before z-axis rotation and the red boundary before x-axis rotation trace the cuts that define the resulting non-mixing islands [122, 148]. During the z-axis rotation, the hemisphere is first rotated by θ_z and cut through the $y = 0$ plane (red curve). The lune bounded by the blue and red curve in (c) is rotated about the z-axis so that the blue curves coincide and red boundary becomes horizontal. Similar to the first rotation, a lune of θ_x is cut at $y = 0$ (black curve) in (f) and rotated about the x-axis so that the red curves meet in (h). This process is then repeated, and the locations of blue and red boundaries are tracked.

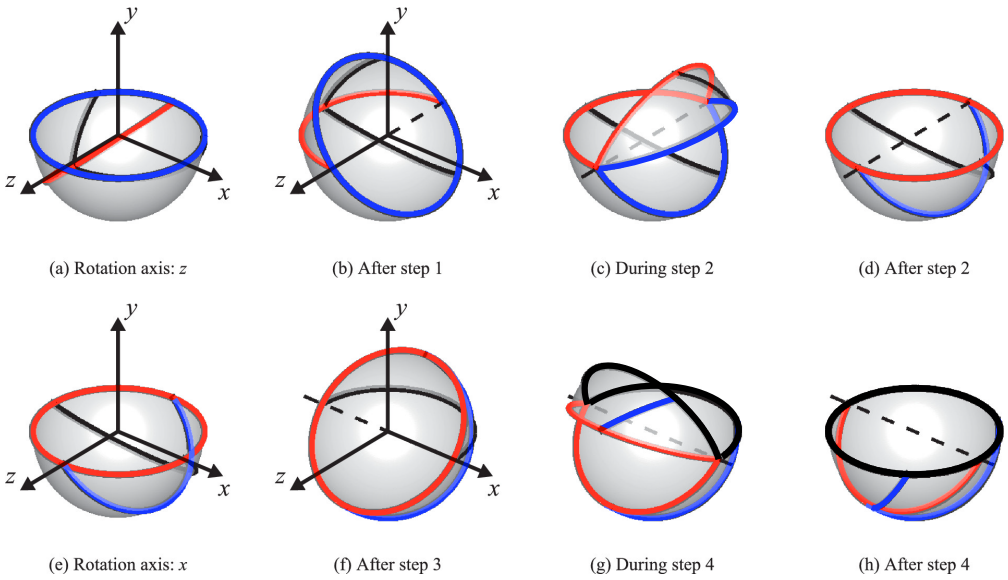

Figure 2.7. Three-dimensional view of the BST PWI operation on the hemispherical shell for the $(45°, 45°)$ protocol. Reprinted from Park et al. [122] with permission ©2016 AIP Publishing.

Park et al. formalized the PWI of a BST system on 2D curvilinear surfaces (hemispherical shells) and identified large regular cells (open areas that are analogous to KAM islands in Poincaré maps) associated with non-mixing behaviors for some protocols, while there are no discernible structures for others [122, 121]. The non-mixing behavior can be understood in terms of a mathematical formulation (*exceptional sets*) that effectively tracks cumulative cutting lines — large regular cells remain uncut and therefore do not mix [122]. Mixing is induced for protocols where the entire domain is cut into small pieces and rearranged. The extent of mixing therefore, is correlated with area of regions that are cut into fine pieces [121]. Thus, protocols with large uncut regions in the PWI correspond to continuum model predictions of non-mixing islands. An example for the $(57°, 57°)$ protocol is shown in Fig. 2.8. In this case, there are two sets of large period-3 regions (six non-mixing regions) evident as large white circular regions in the *exceptional set*. The $(90°, 90°)$ protocol, which is a unique case where the hemispherical shell is only cut in the horizontal and vertical planes, dissects the entire hemispherical surface into four large non-mixing regions. As will be shown later in

this dissertation, these regular cells correspond to the segregation pattern that comes about in a BST flow of size-bidisperse particles. The PWI theory predicts a variety of structures [122]: arrowheads for the $(45°, 45°)$ protocol, nearly uniform cut distribution with no evident structure for the $(45°, 15°)$ protocol, and an intricate pattern for the $(15°, 15°)$ protocol.

Smith et al. used the idea of resonance (similar to periodic return of regular cells) to identify system parameters that govern the shape, size, and locations of regular cells [145]. This study provides important insights to the geometric and systematic reasons for non-mixing behaviors in the PWI and offers a priori prediction of mixing efficacy of the entire protocol space considered [BST protocols of $(\theta_z, \theta_x, 90°)$].

These results for PWI offer guidelines for studying non-mixing behaviors in the BST flows. However, stretching in the flowing layer occurs on top of the underlying skeleton of mixing induced by cutting-and-shuffling. For this reason, a continuum model for the BST is developed as part of this dissertation that can be used to generate Poincaré maps that bridge between cutting-and-shuffling of the PWI, which is the skeleton of the dynamics, and actual granular flow and segregation in a spherical tumbler undergoing the BST protocol for mixing.

2.2. Objective and Topics

This dissertation extends work on dynamical systems approaches to understand mixing and segregation in BST flow. We identify dynamical systems structures of granular flow in a BST flow and understand their role in inducing mixing and non-mixing behaviors, as well as

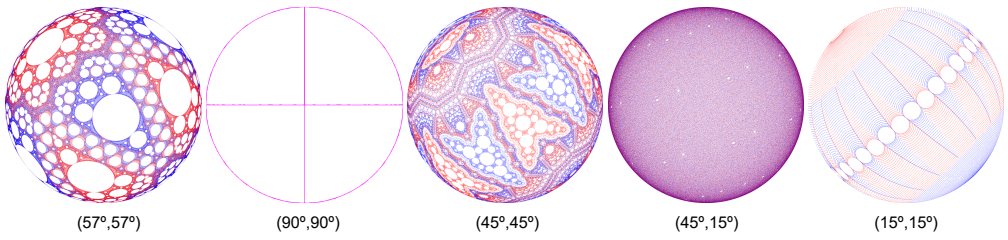

Figure 2.8. Exceptional sets from PWI on hemisphere (bottom view) for BST protocols as indicated with $\gamma = 90°$.

segregation pattern formation. First, analysis of experiments, a continuum model, and PWI theory demonstrates complex mixing dynamics in the 3D BST flow even without particle segregation. Second, segregation pattern formation in a BST flow is explained as a result of the interaction between mixing and segregation of particle species.

To begin, Chapter 3 discusses cutting-and-shuffling as a mixing paradigm in a simple 1D system in comparison to stretching and folding. This abstract mathematical system demonstrates various principles of practical concern for mixing. I extend the previous research in this area by considering uncertainty in cut locations to mimic actual process uncertainties, and demonstrate that its influence on mixing is dependent on the nature of the unperturbed dynamics.

The main focus of this dissertation starts in Chapter 4 with an experimental study of mixing and non-mixing behaviors induced by the flow dynamics in a 3D BST system. Correspondence of experiments to the PWI theory occurs when dynamical systems features persists through finite thickness flowing layer and are large compared to particle size and diffusive effects. These considerations of physical parameters of the flow are made possible by the continuum model, combining the cutting-and-shuffling framework and stretching in the flowing layer. The interaction between mixing induced by flow dynamics and segregation of particle species is described in Chapter 5. Structures of complex segregation patterns are visualized by both photography and x-ray imaging, and a mechanism of pattern formation is proposed. Chapter 6 utilizes DEM simulations of segregation in BST flow to analyze particle movement, which supplies data for demonstrating the mechanism for segregation pattern formation. Chapter 7 summarizes the dissertation and discusses possible extensions.

CHAPTER 3

Cutting and shuffling a line segment: Mixing in one-dimension

SUMMARY

Cutting and shuffling a line segment, a seemingly simple system, generates surprisingly complex dynamics by varying only a few parameters. This system is a realization of cutting-and-shuffling in 1D, formulated as a type of interval exchange transformation (IET) in mathematics. Mixing and the effect of "uncertainty" in mixing are examined across a wide range of parameter space. Mathematical definitions of mixing and their relevance to granular materials are discussed. In general, mixing depends on the long term dynamics of a specific protocol (mixing occurs for irreducible non-rotational permutation). The deterministic mixing result can also be improved by adding stochastic randomness to the system as demonstrated by adding variation in cut locations.

This chapter is based on the publication "Cutting and shuffling a line segment: effect of variation in cut location" by Mengqi Yu, Paul B. Umbanhowar, Julio M. Ottino, and Richard M. Lueptow, *Int. J. Bifurcat. Chaos* **26**, 1630038 (2016). Earlier studies on cutting-and-shuffling of a line segment, i.e. interval exchange transformations, focused on connections to mathematical theories, while I included practical "uncertainties" to examine how they influence system behaviors and mixing.

3.1. Introduction

Dynamical systems provide a widely adopted framework to study flow and mixing problems. Chaotic mixing [113, 5], specifically, has made inroads in wide-ranging fields, including microfluidics [120, 151], physiology [158], food processing [104], polymer processing [178],

composite processing [74], earth sciences [124], oceanography [131, 165], and atmospheric sciences [125]. In the absence of diffusion, a key measure of mixing quality is the amount of intermaterial, or interfacial, area between initially distinct components [119, 78, 136]. Stretching and folding, the fingerprint of chaotic mixing, is the key mechanism to create intermaterial area. The literature covering this topic is vast.

Mixing can also be generated by cutting and shuffling, which, in contrast to stretching and folding, has only recently begun to be explored. The framework of piecewise isometries (PWI) [51, 53] has emerged as a foundation to understand cutting and shuffling. Though PWI is not chaotic, they can generate surprisingly complex dynamics. [79, 103]. The simplest PWI is the one-dimensional case, which is called an interval exchange transformation (IET). In our previous work [89], a specific IET system was constructed to analyze mixing by cutting and shuffling. Here, we consider an even more practical aspect — the effects of small variations in cut location. We show how small random perturbations to the length of subsegments can significantly change mixing dynamics in cutting and shuffling of a line segment.

In this chapter, IET system construction is reviewed along with two different initial conditions, and relevant mathematical theories are summarized to set the foundation for this work. Then we explore the dependence of mixing by cutting and shuffling on various parameters including the permutation order, the magnitude of variation in cut location and the subsegment length ratio. The interplay of these parameters is examined as well as the impact of the initial condition on the mixing metrics. We conclude by characterizing approaches that typically result in good mixing and discuss how they might apply to more complicated PWI.

3.2. IET construction and simulation methodology

A specific realization of an IET can be constructed for cutting and shuffling a line segment [89]. The mixing procedure consists of repeated cutting of a line segment into subsegments, and then rearranging (shuffling) the subsegments in a prescribed order. A unit length line segment is divided into N subsegments of length L_i (i = 1,2,$\cdots$,N), where the ratio $r = L_{i+1}/L_i \geq 1$ defines the relative lengths of consecutive subsegments. Subsegment lengths are normalized so that the entire line segment is defined on [0 1].

Two types of initial conditions are considered: 1) multicomponent initial conditions ($N \geq$ 4) with the initial interfaces between component intervals corresponding to the cut locations; and 2) two-component initial conditions in which the line segment consists of two equal intervals of distinct components independent of cut locations. In the multicomponent initial condition case, each component is assigned a unique color for visualization (multicolor), as shown in Fig. 3.1(a). We call an interval of a single component (color) in the line segment a "component interval" to distinguish it from the subsegments whose interfaces are the cuts. In this case, the component intervals are equivalent to the subsegments divided by the cuts in the initial configuration. This is in contrast to the two-component initial condition in which each component interval (black or white) covers one-half of the line segment, independent of the cut locations. The effect of initial conditions on cutting and shuffling is discussed later in this chapter.

For both types of initial conditions, the subsegments after the cut are numbered consecutively (1,2,. . . , N) and rearranged in the order specified by the permutation Π([1 2 ... N]) = {1,2,...,N}, where {1,2,...,N} denotes all possible permutations of the set. For example, in Fig. 3.1(a), after the cut, the subsegments are shuffled according to the permutation Π([1 2 3 4]) = [3 1 4 2], where the integers denote the sequence of the output of one iteration. We use the notation Π = [3142] for brevity. The transformation maps the line segment [0 1] onto itself. After shuffling, interfaces between identical components are removed allowing

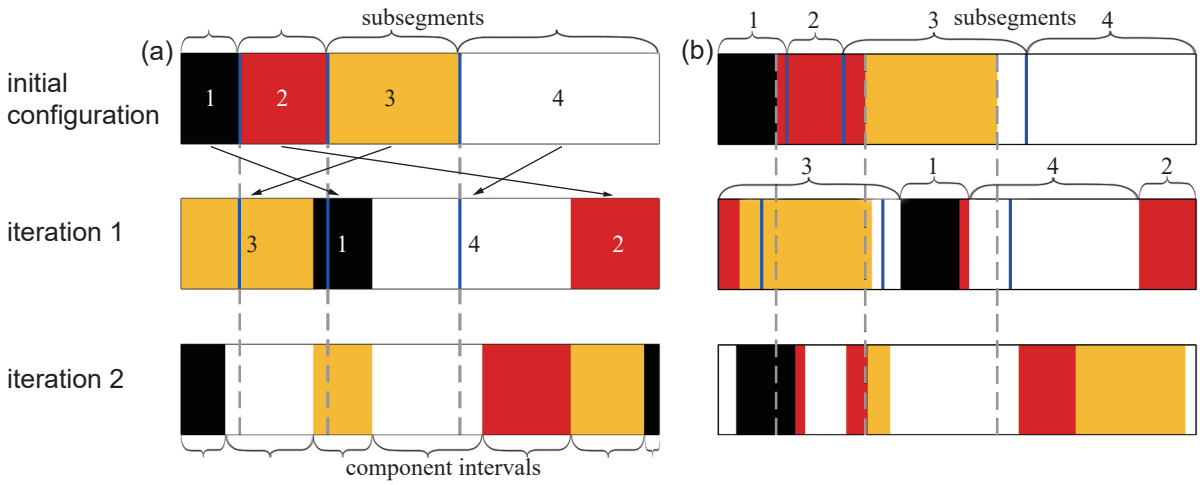

Figure 3.1. Illustration of the first two iterations of an IET for the initial conditions with $N = 4$, $r = 1.5$, and $\Pi = [3142]$. Dashed lines indicate exact cut locations. Cut locations (blue solid lines) can be made at the same location (a) or varied (b). Subsegments are defined by the cut locations whereas component intervals are independent of the cuts. Subsegments and component intervals are equivalent to each other in the initial condition in (a), but not in (b).

them to recombine. Interfaces between distinct components remain. For the subsequent iteration, the line segment is cut at the same locations (independently of components) to give N subsegments again, and the new subsegments are shuffled and reassembled according to the same rearrangement order. Multiple applications of the IET mixes the components (colors) of the initial line segment to different degrees depending on N, r, Π, and the number of iterations, n.

3.2.1. Variation in cut location

To analyze the effect of variation in cut location, we introduce a small random variation to the "exact" locations for each cut of every iteration. The "exact" cut locations, shown by blue vertical lines in Fig. 3.1(a), are aligned for every iteration. In contrast, the cut locations with variation, shown in Fig. 3.1(b), can be on the left or right of the "exact" cut locations (dashed lines). Note that the initial condition is still constructed with the interfaces between component intervals corresponding to the "exact" cut locations as in Fig. 3.1(a).

However, the subsegments are not equivalent to component intervals for the initial condition in Fig. 3.1(b) since the cuts are perturbed. The lengths of the subsegments after the cut are slightly different from the "exact" subsegment lengths (but they still sum to 1). After the first iteration, there are seven component intervals in Fig. 3.1 (b) instead of only four in Fig. 3.1(a). The variation in cut location is distributed according to a normal distribution with variance σ^2. $\sigma = 0$ indicates cutting and shuffling with exact cut locations, and $\sigma > 0$ corresponds to variation in the cut location. Thus, now σ can be varied in addition to the parameters N, r, and Π. In MATLAB simulation, the variation in cut location is generated by the *randn* command. A brief description of the algorithm is given in the Appendix A. In these simulations, σ is always smaller than the shortest subsegment length and the distribution is bounded as needed so that the cut locations do not overlap or exceed the [0 1] interval.

The degree of mixing is quantified using the percent unmixed, U_n, and the number of interfaces between distinct components, C_n. U_n at iteration n is the percentage of the line segment corresponding to the longest continuous component interval, which is a measure of the degree of local mixing. In both Fig. 3.1(a) and 3.1(b), U_2 is the percentage of the line segment corresponding to the large white component interval in the middle. A small U_n corresponds to good mixing since all component intervals are equal to or shorter than this value. C_n at iteration n is the number of interfaces between distinct components. $C_2 = 6$ in Fig. 3.1(a) and $C_2 = 9$ in Fig. 3.1(b). The number of interfaces measures global mixing properties. Large C_n corresponds to many interfaces and, hence, good mixing. Although various ways to quantify mixing exist [8, 153, 98], U_n and C_n are suitable for finite time non-diffusive mixing analysis as in the present work. Both measures are intuitive, easy to compute, have physical significance, and have been used previously [89].

3.2.2. Reducible, irreducible and rotational permutations

IET permutations can be categorized as ***reducible*** or ***irreducible***. A permutation Π is ***reducible*** [81] if for some $1 \leq i \leq N-1$,

$$\Pi(\{1,2,...,i\}) = \{1,2,...,i\} \tag{3.1}$$

A permutation that is not reducible is termed **irreducible**. For any $i < N$, the set of the first i elements after shuffling is a permutation of the subset itself for a ***reducible*** permutation, or equivalently, a ***reducible*** permutation is one that can be decomposed into separate permutations of the subsets. For example, $\Pi = [2143]$ is a ***reducible*** permutation because the first two elements are a permutation of the subset itself, i.e., $\Pi([12]) = [21] = \{1,2\}$. Similarly, $\Pi = [24135]$ is a ***reducible*** permutation in that $\Pi([1234]) = [2413]$ is a permutation of the subset itself. In contrast, $\Pi = [3412]$ is ***irreducible***, because it cannot be decomposed into separate subsets. Note that $\Pi([12345]) = [52341]$ is ***irreducible*** even though $\Pi([234]) = [234]$. The definition of a ***reducible*** permutation requires that one of the subsets always includes the first element.

A subgroup of ***irreducible*** permutations is ***rotations***. A rotational permutation Π of {1,2,...,N} satisfies [9]

$$\Pi(i+1) \equiv \Pi(i) + 1 \quad mod \quad N \tag{3.2}$$

for all $i \in \{1,2,...,N\}$. It is easily understood as a permutation where all elements shift in one direction by the same amount, but the sequence of elements does not change. For example $\Pi = [3412]$ is a rotation.

3.2.3. Mixing and related theories

Mathematical theories concerning IETs have been developed in close relationship to ergodic theory, which provides a hierarchy of definitions of mixing [155, 153] that considers levels of randomness [10] of a system in the limit as the number of iterations goes to infinity. Keane defined the minimality condition and further proved that if an IET has an irreducible permutation and the subsegment lengths are rationally independent (not linear combinations of each other with rational coefficients), then such an IET is minimal [81]. It was shown that a minimal IET is ergodic [81], satisfying the lowest level of the ergodic hierarchy. More recently, it has also been proven that almost every minimal IET with irreducible non-rotational permutation is weakly mixing [9]. Weakly mixing is a stronger result then ergodicity in the hierarchy, yet both of these results only consider the infinite iteration limit.

For a finite number of iterations, nevertheless, it has been shown that cutting and shuffling a line segment with irreducible permutations can yield significant mixing provided that the protocols have the following characteristics [89] :

(i) The rearrangement order should be an irreducible permutation.

(ii) The line segment should be cut into a large number of subsegments ($N \geq 6$ subsegments).

(iii) The ratio of adjacent subsegment lengths should ideally be irrational and close to 1.

Reducible permutations do not mix well [89, 81, 162], since the decomposition of subsets hinders mixing by trapping the elements inside the subsets. As we will show later, rotational permutations, even though they are irreducible, do not yield good mixing, because the elements only cycle through the line segment. The observation that an irrational subsegment length ratio yields optimal mixing [89] corresponds to the theoretical requirement that subsegment lengths be rationally independent to avoid periodic dynamics [81, 162]. However, the impact of variation in cut location on mixing, which is a practical consideration, has not been studied and is the focus here.

3.2.4. Space-time plots

Space-time plots effectively illustrate the dynamics of cutting and shuffling a line segment as shown in Fig. 3.2. In the space-time plots, the initial configuration is located at the top, and the output from each iteration is consecutively positioned below. In this way, the evolution of the overall pattern is made evident.

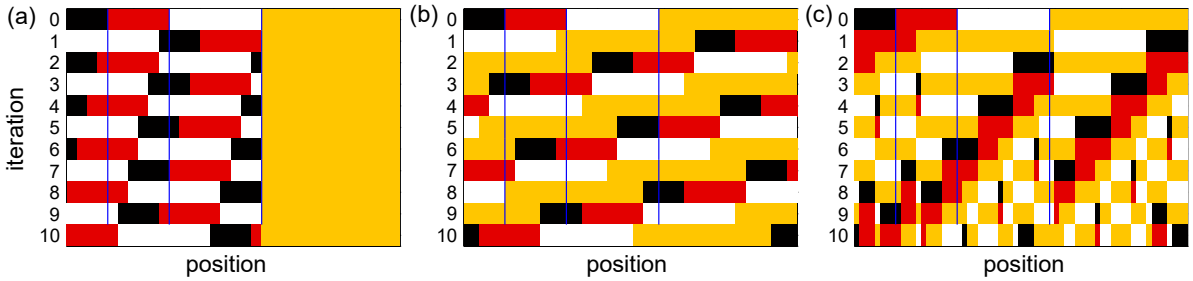

Figure 3.2. Cutting and shuffling of a line segment by (a) a reducible permutation $\Pi = [3124]$ for which the last subsegment remains in the same location; (b) an irreducible permutation that is a rotation $\Pi = [3412]$, where the pattern demonstrates simple periodic dynamics; and (c) an irreducible permutation that is not a rotation $\Pi = [2431]$, where significant mixing occurs after relatively few iterations.

The choice of permutation can affect mixing significantly. Figure 3.2(a) shows an example of poor mixing under a reducible rearrangement order $\Pi = [3124]$. The degree of mixing remains low because the fourth subsegment is never shuffled to other locations. In contrast, irreducible rearrangement orders in 3.2(b) and 3.2(c) shuffle all subsegments. However, there is an obvious difference between 3.2(b) and 3.2(c): a simple periodic pattern in 3.2(b) and significant mixing in 3.2(c). The rearrangement order $\Pi = [3412]$ in Fig. 3.2(b) is a rotation and its mixing is representative of all rotational permutations. Mixing under rotations yields periodic dynamics in which the initial pattern only shifts laterally but never mixes. In our previous work [89], rotations were identified with poor mixing, but all irreducible permutations (including rotations) were used when comparing to reducible permutations in the analysis of the effects of N and r on mixing.

3.3. Results and discussions

3.3.1. Cutting and shuffling with rational r

In Fig. 3.3 we show the results of two sets of cutting and shuffling protocols with $N = 4$, $r = 1.5$, $\Pi = [3142]$ and $N = 6$, $r = 1.25$, $\Pi = [653241]$ both without variation ($\sigma = 0$) and with variation ($\sigma = 0.005$) in cut location.

In Fig. 3.3(a), a periodic pattern is clearly evident in the space-time plot, with complete reassembly at iteration 65. Even though $\Pi = [3142]$ is irreducible and non-rotational, the periodicity comes about from r being rational, and particularly, a ratio of two small integers, $r = 1.5$, or $3/2$. Such a periodic pattern correlates with poor mixing. In Fig. 3.3(b), introducing variation in cut location changes the dynamics significantly and slowly destroys the periodic pattern that resulted from r being rational. The original periodicity of the pattern becomes hard to discern after 60 iterations, though some vestiges remain evident near the bottom of the plot. Nevertheless, it is clear that introducing variation in cut location prevents reassembly of the initial components and improves mixing.

Now consider an irreducible permutation that leads to significant mixing with no variation in cut location (Fig. 3.3(c)). Variation in cut location again perturbs the pattern, as shown in Fig. 3.3(d), but the improvement in mixing quality from Fig. 3.3(c)-3.3(d) is less obvious when comparing the mixing at iteration 100 in the two cases.

To explore mixing in more depth, including the interplay between Π, r, and σ, we examine several cases in detail. Four typical mixing results for *irreducible non-rotational* permutations can be obtained by simply switching two elements in the permutation order [89], as shown in the left column of Fig. 3.4(a)-(d). We contrast space-time plots of mixing with no variation in cut location ($\sigma = 0$ in the left column) with variation in cut location ($\sigma = 0.005$ in the middle column) and compare the percent unmixed U_n as a function of the number of iterations in both cases (right column). The blue lines in the space-time plots indicate the

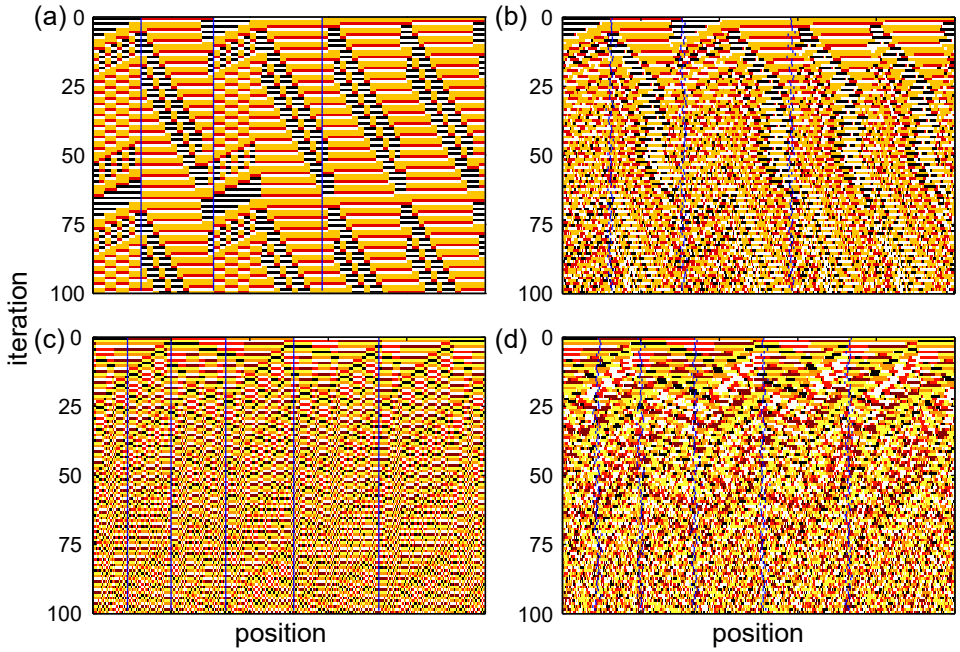

Figure 3.3. Space-time plots over 100 iterations of IET based cutting and shuffling for two different combinations of parameters: (a,b) $r = 1.5$, $\Pi = ([3142])$; (c,d) $r = 1.25$, $\Pi = ([653241])$. Variation in cut location is $\sigma = 0$ (a,c) and $\sigma = 0.005$ (b,d).

cut locations. For $\sigma = 0$ (left column), the cut locations are fixed at each iteration resulting in straight vertical blue lines, whereas the blue lines are distributed around the exact cut locations for mixing with variation in cut location in the middle column for $\sigma = 0.005$.

Figure 3.4(a), for the irreducible, non-rotational permutation $\Pi = [52413]$, suggests that significant mixing can be achieved with exact cuts ($\sigma = 0$). However, there is still a global periodic pattern that limits mixing. This pattern is disturbed by variation in the cut location ($\sigma = 0.005$), evident starting from about the 20th iteration. The component intervals appear more random in length and location. The difference is quantified in terms of the decay of the percent unmixed, U_n (right). After approximately 50 iterations, U_n for $\sigma = 0$ varies with a small amplitude as intervals reassemble and are cut again. U_n for $\sigma = 0.005$ continues to decay with increasing n as the longest interval decreases in length. Thus, slightly improved mixing results from variation in cut location.

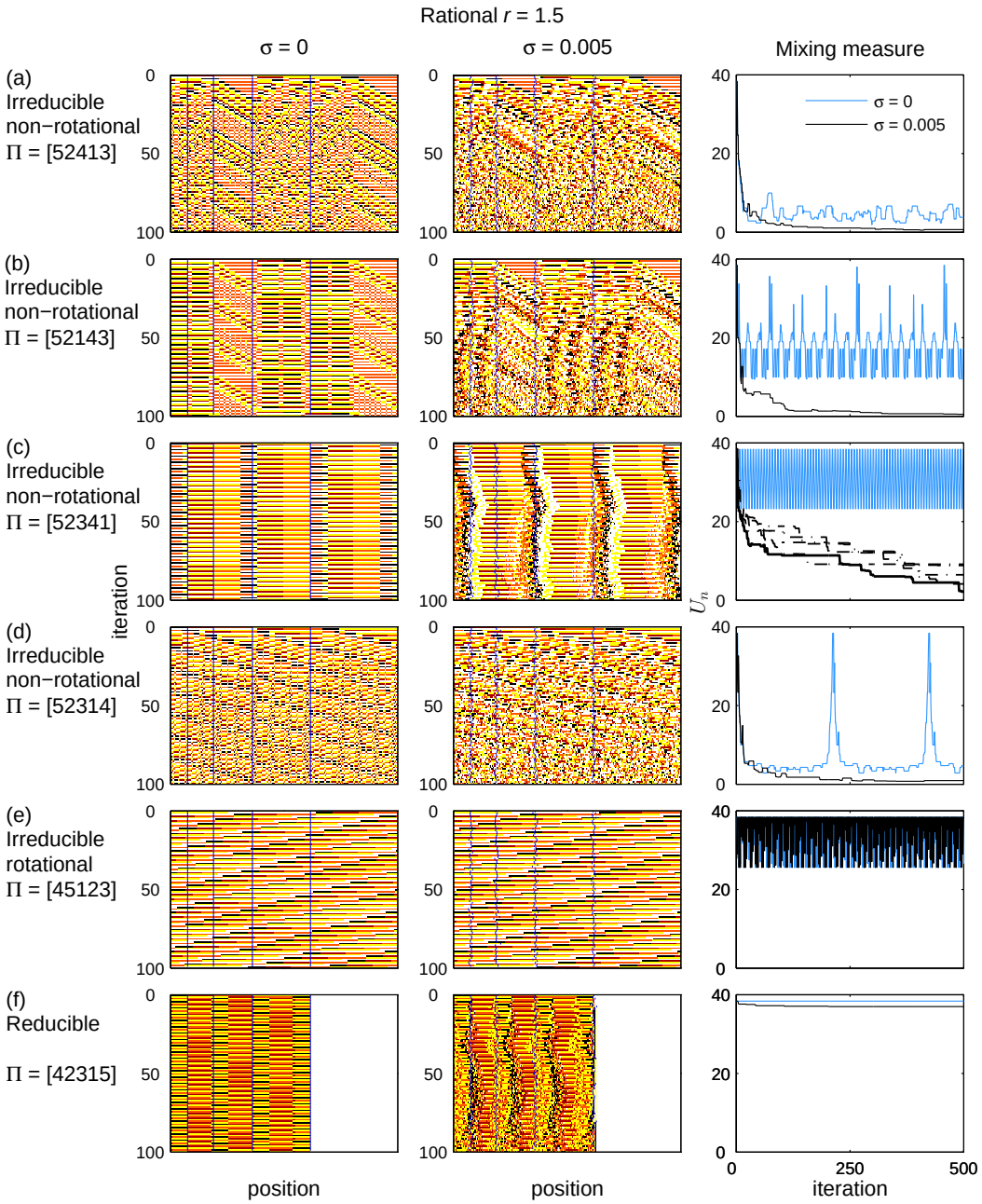

Figure 3.4. Mixing depends on permutation ($N = 5$, $r = 1.5$, and $\sigma = 0$ (left column) or $\sigma = 0.005$ (middle column)). The percent unmixed U_n is displayed as a function of iteration n in the right column. Irreducible non-rotational permutations are applied in (a) $\Pi = [52413]$, (b) $\Pi = [52143]$, (c) $\Pi = [52341]$, and (d) $\Pi = [52314]$; an irreducible rotational permutation is applied in (e) $\Pi = [45123]$, and a reducible permutation is used in (f) $\Pi = [42315]$.

The second irreducible non-rotational permutation order considered, $\Pi = [52143]$ shown in Fig. 3.4(b), results in a periodic pattern that is obvious in the space-time plot for $\sigma = 0$. The periodicity corresponds to short period oscillations in U_n and large amplitude peaks

as component intervals reassemble. Cutting and shuffling with variation in cut location ($\sigma = 0.005$) destroys the periodic pattern after only about 20 iterations, and the associated value of U_n is well below that for the case with no variation in cut location ($\sigma = 0$).

In Fig. 3.4(c), the irreducible, non-rotational permutation $\Pi = [52341]$ also results in a periodic pattern in the space-time plot for $\sigma = 0$. This pattern persists with variation in cut location ($\sigma = 0.005$), except with the interfaces slightly perturbed. The periodic fluctuation of U_n indicates that cutting and shuffling with $\sigma = 0$ in this case ($\Pi = [52341]$) results in global reassembly every few iterations. U_n for $\sigma = 0.005$ decreases monotonically as expected but at a much slower rate here (Fig. 3.4(c)) than in Fig. 3.4(a) and Fig. 3.4(b). Note, however, that the randomness in the locations of the cuts plays a significant role. The decay of U_n with variation in cut location is shown for five different runs, each with different sets of variations generated randomly. In one case, U_{500} is less than 5%, while in four other cases it is substantially higher. Thus, variation in cut location improves mixing but the details are sensitive to the particular variations.

The surprisingly large value for U_n ($\sigma = 0$) and slow decay of U_n ($\sigma = 0.005$) for this irreducible non-rotational permutation in Fig. 3.4(c) is a result of the [234] sequence in the middle of the permutation ($\Pi = [52341]$). The only other irreducible non-rotational permutations for $N = 5$ with a sequence of 3 consecutive elements are $\Pi = [54123]$ and $\Pi = [34521]$ which have similar mixing characteristics to $\Pi = [52341]$. Likewise, shorter sequences of 12, 23, 34, or 45 in the middle of an irreducible non-rotational permutation do not mix as well as permutations without these sequences, though the effect is not as severe. Similar results occur for consecutive sequences in irreducible non-rotational permutations for $N = 4$ and $N = 6$. Thus, it seems that consecutive sequences in irreducible non-permutations should be avoided to obtain good mixing, though we are not aware of a theoretical basis for this result.

The last example of an irreducible non-rotational permutation, $\Pi = [52341]$ in Fig. 3.4(d), again demonstrates how variation in cut location perturbs the periodic pattern in the space-time plots. U_n for cutting and shuffling with $\sigma = 0$ decays to less than 5% in around 50 iterations, but the intervals reassemble to generate a peak in U_n within 250 iterations. U_n for cutting and shuffling with $\sigma = 0.005$ decays at the same rate for the first approximately 50 iterations, but continues to decay thereafter, completely obliterating the large peak that occurs at $n = 213$ for $\sigma = 0$.

Comparing the four examples discussed above in Fig. 3.4(a)-(d), U_{500} for $\sigma = 0.005$ is very similar in all four cases except Fig. 3.4(c) with $\Pi = [52341]$. This type of irreducible non-rotational permutation with a consecutive sequence yields mixing that depends on randomness in variation in cut location. Nevertheless, variation in cut location always improves both the rate and the degree of mixing for all irreducible non-rotational permutations.

Mixing under a *rotational* permutation ($\Pi = [45123]$) is shown in Fig. 3.4(e). The simple periodic pattern in the space-time plot demonstrates how the intervals just cycle through the line segment in the same order. Even with variation in cut location, the order of the component intervals does not change, and the variation in cut location only offsets the starting point of a cycle, since all subsegments shift together. The resulting plot of U_n shows a very large value with high frequency variations regardless of σ. Clearly, cutting and shuffling with variation in cut location does not significantly improve mixing for rotational permutations.

Figure 3.4(f) demonstrates that mixing for a *reducible* permutation ($\Pi = [42315]$) remains poor even when variation in cut location is introduced. The last subsegment remains at the same location and prevents further mixing. In the space-time plot for cutting and shuffling with $\sigma = 0.005$, the length of the last white interval is reduced only slightly by the shifting cut at its left edge while the other intervals mix. As n increases, the cut could possibly occur far from the mean location, but with low probability. U_n for $\sigma = 0$ stays constant,

and U_n with $\sigma = 0.005$ decreases only slightly even after 500 iterations. Thus, reducible and rotational permutations that yield poor mixing with exact cut locations will not show significant improvement when variation in cut location is introduced. Instead, the dynamics are dictated by the permutations.

3.3.2. Cutting and shuffling with closer-to-irrational r

Mixing protocols with irrational r should produce better mixing [89, 81, 162]. However, all IETs realized with finite precision calculations necessarily have rational values for r and thus will always be periodic [81]. though the period may be quite long. Nevertheless, we can examine the effect of a rational r getting closer to an irrational number through the concept of a finite continued fraction [1] [88]. Every real number has a specific continued fraction expansion and it is finite for a rational number [88]. We call a number with a longer continued fraction expansion "closer-to-irrational". To demonstrate the effect of r, we consider in Fig. 3.5 a closer-to-irrational value of $r = 1.49$ (four terms expansion) for the same six permutations to compare with $r = 1.5$ (two terms expansion). We also considered $r = 1.497$, which is even closer to irrational (five terms expansion) than $r = 1.49$, but the results are very similar to those for $r = 1.49$, suggesting that the biggest gain comes from simply shifting away from $r = 1.5$. It is evident that a closer-to-irrational value of $r = 1.49$ reduces the propensity for reassembly that occurs for $r = 1.5$ when comparing the right column in Fig. 3.5 to that in Fig. 3.4 for the first four cases (a-d) with $\sigma = 0$. Furthermore, the mixing is comparable for $\sigma = 0$ and $\sigma = 0.005$ in 3.5(a), 3.5(b), and 3.5(d). In these three

[1] Finite continued fraction with k partial denominators:

$$[a_0; a_1, ..., a_k] = a_0 + \cfrac{1}{a_1 + \cfrac{1}{a_2 + \cfrac{1}{\ddots + \cfrac{1}{a_k}}}}. \tag{3.3}$$

The continued fraction expansion for $r = 1.5$ is [1;2] while for $r = 1.49$ it is [1;2,24,2]. Thus $r = 1.49$ is closer to irrational

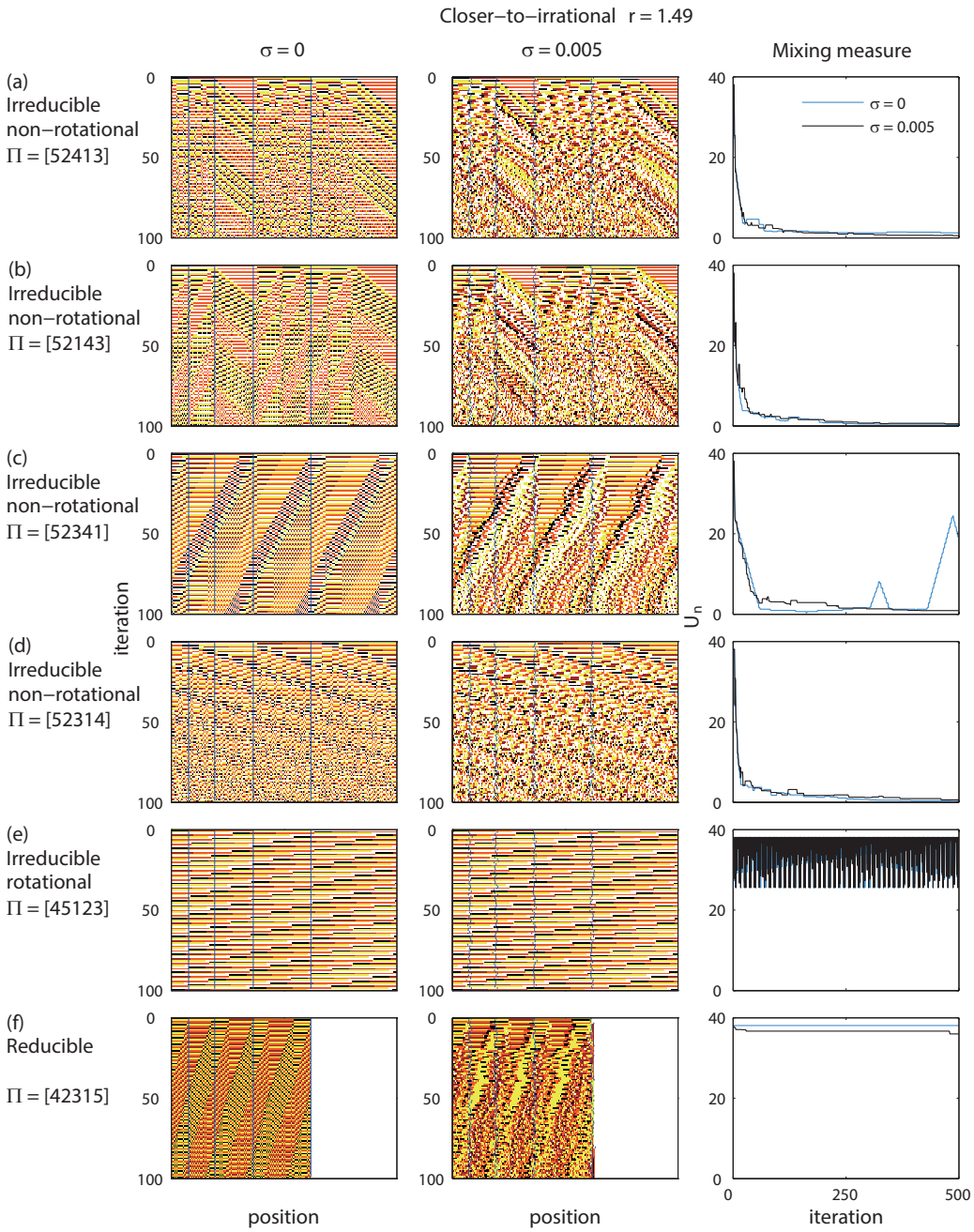

Figure 3.5. Mixing depends on permutation ($N = 5$, $r = 1.49$, and $\sigma = 0$ (left column) or $\sigma = 0.005$ (middle column)). The percent unmixed U_n is displayed as a function of iteration n in the right column. Irreducible non-rotational permutations are applied in (a) $\Pi = [52413]$, (b) $\Pi = [52143]$, (c) $\Pi = [52341]$, and (d) $\Pi = [52314]$; an irreducible rotational permutation is applied in (e) $\Pi = [45123]$, and a reducible permutation is used in (f) $\Pi = [42315]$. Identical permutations as in Fig. 3.4 but with a closer-to-irrational $r = 1.49$.

cases, regardless of the value of σ, U_n decreases to below 5% in the first 50 iterations and continues to decay even up to 500 iterations. Interestingly, for the irreducible non-rotational

permutation with a consecutive sequence in Fig. 3.5(c), partial reassembly still occurs for r = 1.49 and $\sigma = 0$. For the first 250 iterations, U_n for both $\sigma = 0$ and $\sigma = 0.005$ decreases to less than 5%. The two curves diverge around 300 iterations and again near 500 iterations when partial reassembly occurs for $\sigma = 0$. Nevertheless, mixing is improved with variation in cut location. For the permutations in Fig. 3.5(a), 3.5(b), and 3.5(d), reassembly is not evident within 500 iterations but will occur eventually, because every IET with a rational r is periodic. However, when reassembly starts, U_n for $\sigma = 0$ increases, while U_n for $\sigma = 0.005$ remains small as is the case in Fig. 3.5(c).

While the dynamics change with closer-to-irrational r for irreducible non-rotational permutations, the rotational permutation in Fig. 3.5(e) and the reducible permutation in 3.5(f) with r = 1.49 are quite similar to those with r = 1.5 in Fig. 3.4(e) and (f). Even with r = 1.49, a rotation like that in Fig. 3.5(e) only shifts the subsegments without mixing them, even when there is variation in the cut location. Similarly, neither a closer-to-irrational r nor a variation in cut location can alter the unchanging position of the last subsegment for the reducible permutation in Fig. 3.5(f).

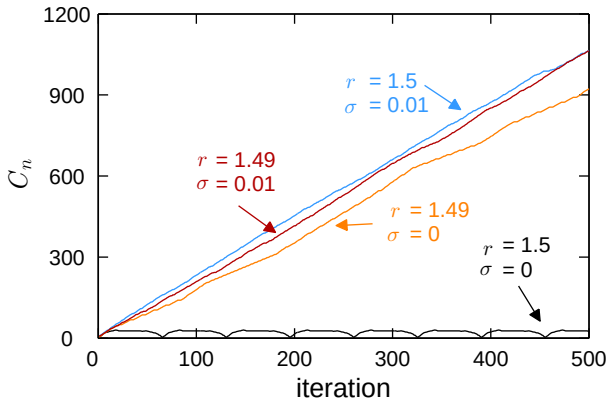

Figure 3.6. Number of interfaces C_n vs. iterations for $\Pi = [3142]$ for all four combinations of $r = \{1.49, 1.5\}$ and $\sigma = \{0, 0.01\}$.

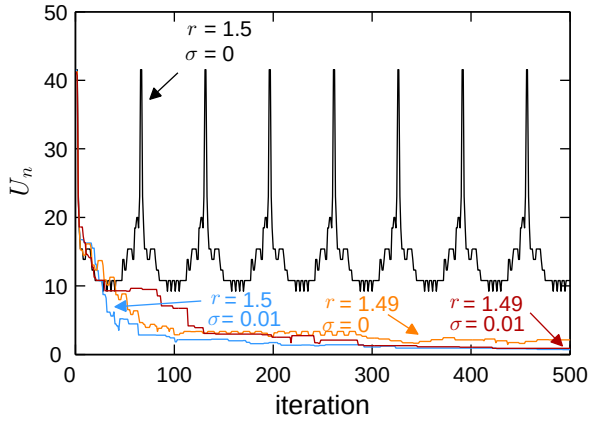

Figure 3.7. Percent unmixed U_n vs. iterations for $\Pi = [3142]$ for all four combinations of $r = \{1.49, 1.5\}$ and $\sigma = \{0, 0.01\}$.

3.3.3. Variation in cut location versus closer-to-irrational r

Variation in cut location enhances mixing to a degree similar to that for a closer-to-irrational r for some examples of irreducible non-rotational permutations — compare Figures 3.4(a, b, and d) with Figure 3.5(a, b, and d). Accordingly, we now consider in detail the effect of variation in cut location and r closer-to irrational for a typical irreducible non-rotational permutation, $\Pi = [3142]$. In Fig. 3.6, the number of interfaces C_n is plotted as a function of iteration for combinations of r and σ. C_n is periodic and stays small for $r = 1.5$ and $\sigma = 0$, since the initial pattern reassembles every 65 iterations (Fig. 3.3(a)). The period of C_n for $r = 1.49$ and $\sigma = 0$ is far beyond 10^5 iterations, so the increase in C_n is almost linear for the first 500 iterations. Similarly, changing σ from 0 to 0.01 for $r = 1.5$ induces linear growth of C_n over the first 500 iterations. However, changing $\sigma = 0$ to 0.01 for $r = 1.49$ does not alter the rate at which C_n increases. Note that for $r = 1.49$ and $\sigma = 0$, C_n eventually decreases to the initial number of cuts because of global reassembly, while C_n would continue to increase for $r = 1.49$ and $\sigma = 0.01$. We hypothesize that the growth of C_n for $\sigma \neq 0$ would continue linearly even as $n \to \infty$, since each cut is made at a distinct location, making component reassembly unlikely to occur. Note that the "linear" increase in intermaterial area indicates

cutting and shuffling is a different mechanism from stretching and folding which exhibits an exponential mixing rate [16].

Corresponding plots of U_n for the cases in Fig. 3.6 are shown in Fig. 3.7. The high frequency periodic dynamics for $r = 1.5$ with $\sigma = 0$ result in peaks in U_n due to global reassembly. Cutting and shuffling with the closer-to-irrational $r = 1.49$ but still $\sigma = 0$ leads to better mixing as U_n decays quickly in 100 iterations and continues to decrease up to 500 iterations, since $r = 1.49$ extends the reassembly period beyond 10^5 iterations. Cutting and shuffling with variation $\sigma = 0.01$ results in effective mixing at 500 iterations regardless of r.

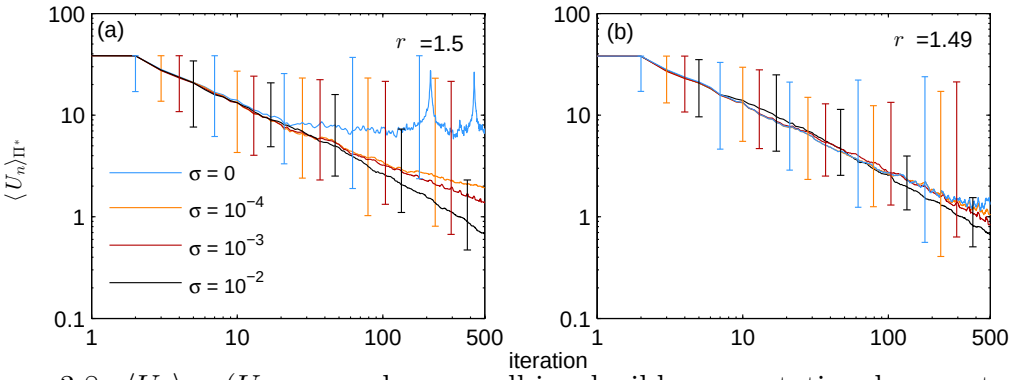

Figure 3.8. $\langle U_n \rangle_{\Pi^*}$ ($U_n$averaged across all irreducible non-rotational permutations Π^*) for (a) $r = 1.5$ and (b) $r = 1.49$ with $\sigma = 0$, 10^{-4}, 10^{-3}, and 10^{-2} for $N = 5$. Error bars indicate the upper and lower extremes of the U_n distribution.

Cutting and shuffling with variation in cut location improves mixing even with closer-to-irrational values for r by adding more discontinuities while preserving existing ones. For every iteration, the subsegment lengths are rational but they can vary randomly. Keane's condition[81] is not satisfied in the mathematical sense, since neither the cut variations nor the subsegment lengths are irrational values. Nevertheless, the dynamics appear to be aperiodic as if the subsegment lengths were rationally independent. Thus, the effect of variation in cut location and a closer-to-irrational r are similar in that the lengths of subsegments become rationally independent resulting in significant mixing.

3.3.4. Dependence of mixing on σ and r

We have demonstrated that variation in cut location can improve mixing for some specific examples of IETs with irreducible non-rotational permutations. Consider now the impact of the magnitude of σ on mixing for the irreducible non-rotational permutations shown in Fig. 3.8. The percent unmixed $\langle U_n \rangle_{\Pi^*}$, averaged across all irreducible non-rotational permutations Π^* is plotted as a function of iteration n for $N = 5$ and $r = 1.5$ in Fig. 3.8(a) and $r = 1.49$ in Fig. 3.8(b). Behaviors for $N = 4$, 5, and 6 are identical, so only the results for $N = 5$ are presented here. Peaks in $\langle U_n \rangle_{\Pi^*}$ for cutting and shuffling with $\sigma = 0$ in Fig. 3.8(a) indicate strong reassembly for many permutations around 200 iterations. As variation in cut location is introduced, $\langle U_n \rangle_{\Pi^*}$ decays almost linearly on a log-log scale and continues to decay after 500 iterations for all three values of $\sigma \neq 0$. This suggests that variation in cut location breaks a fundamental constraint associated with cutting and shuffling with unperturbed cuts. Even with variation of only $\sigma = 10^{-4}$, the peaks in U_n evident for $\sigma = 0$ are eliminated and mixing is improved for $n >$20. Large values of σ improve mixing marginally for $n >$50.

For the closer-to-irrational value of $r = 1.49$ shown in Fig. 3.8(b), $\langle U_n \rangle_{\Pi^*}$ for cutting and shuffling with $\sigma = 0$ does not exhibit periodic dynamics in the first 500 iterations, though global reassembly eventually occurs at a large enough n. Unlike the case for $r = 1.5$, $\langle U_n \rangle_{\Pi^*}$ for $r = 1.49$ decays with n regardless of whether there is variation in cut location or not. It is evident from Fig. 3.4 - 3.8, for irreducible, non-rotational permutations, that $\sigma \neq 0$ and closer-to-irrational values of r have similar effects in reducing reassembly and improving mixing, but using both together does not result in further improvement in mixing in finite time. In contrast, specific values for r and σ make little difference in mixing for reducible or rotational permutations. Poor mixing always results.

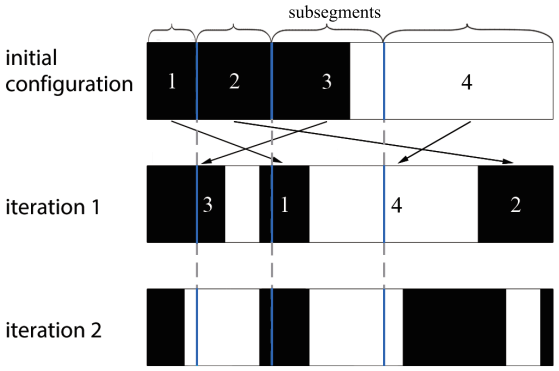

Figure 3.9. Illustration of the first two iterations of cutting and shuffling with a two component initial condition for $r = 1.5$, $\sigma = 0$, and $\Pi = [3142]$. The cut locations and variation are implemented in the same manner as in Fig. 3.1.

3.3.5. Effect of initial conditions

A question that arises is the dependence of the mixing on initial condition. Up to this point, multicomponent initial conditions have been used for our analysis. The coloring serves as a tracking method where each color can be thought to represent a group of tracers. From this perspective, the space-time plots show how the tracer points in each component interval move under cutting and shuffling. Moreover, the colors allow the human eye to easily discern if the line segment is mixed well or not. However, the initial condition in this approach depends on N and r, which are parameters for the cutting and shuffling protocols. In fact, U_0 depends on N and r even before the first iteration of shuffling. Therefore, using U_n to compare mixing efficiency at the same n for different choices of N and r has the potential to inadvertently reflect the initial conditions. Thus, we consider as an alternative a consistent initial condition independent of N and r.

A commonly used initial condition that may be the most relevant in practical applications is equal amounts of two components. Each component is assigned its own color, for simplicity black and white here. As Figure 3.9 shows, each iteration of cutting and shuffling still follows the same approach as in the multicolor scheme in Fig. 3.1.

Table 3.1. Number of permutations ($N!$), irreducible permutations, and fraction of rotations for increasing N. The number of rotation permutations is N - 1. The number of irreducible permutations is calculated by Comtet [1974] and recorded by Sloane [2010]. For a more detailed discussion of irreducible permutations, see Klazar [2003].

N	1	2	3	4	5	6	7	8	9	10
Total = $N!$	1	2	6	24	120	720	5040	40320	362880	3628800
Irreducible	1	1	3	13	71	461	3447	29093	273343	2829325
Rotation/irred.	0	1	0.67	0.23	0.06	0.01	0.0017	$2.4\text{x}10^{-4}$	$2.9\text{x}10^{-5}$	$3.2\text{x}10^{-6}$

The "multicolor" approach and the "black and white" approach can be compared in the context of the effect of subsegment length ratio r on mixing for cutting and shuffling with $\sigma = 0$ or $\sigma = 0.005$ and $N = 4$, 5, and 6. In Fig. 3.10(a), the percent unmixed $\langle \overline{U}_n \rangle_\Pi$ averaged across all irreducible permutations (including rotations) for iterations 51-100 is plotted as a function of r for the multicolor initial conditions. We consider iterations 51-100 to average out large fluctuations in $\langle \overline{U}_n \rangle_\Pi$ resulting from reassembly (like those in Fig. 3.4(b)). The best mixing corresponds to the smallest value of $\langle \overline{U}_n \rangle_\Pi$, which occurs at an r value slightly larger than 1, consistent with previous results [89]. $\langle \overline{U}_n \rangle_\Pi$ is smaller for larger N for $1 < \text{r} < 3$, also consistent with previous results. Results for the black and white initial condition shown in Fig. 3.10(b) are quite similar including peaks at $r = 1/1$, $2/1$, $3/2$, and $3/1$ (for which intervals readily reassemble). Again, better mixing results as N increases, and poorer mixing results as r increases, because it takes many iterations to break up the longest interval. Thus, the general conclusions [89] about the impact of the parameters on mixing in Section 3.2.3 are similar regardless of the initial condition. However, the numeric values for $\langle \overline{U}_n \rangle_\Pi$ differ between the two initial conditions with the multicolor initial condition having a lower value for r close to 1 due to their smaller initial subsegment lengths. When r increases, $\langle \overline{U}_n \rangle_\Pi$ is smaller for the black and white initial condition because the last component interval in multicolor initial condition is longer than 0.5.

As noted in Section 3.3.2, irreducible permutations that are rotations result in poor mixing. Moreover the fraction of rotational permutations that are a subset of the irreducible

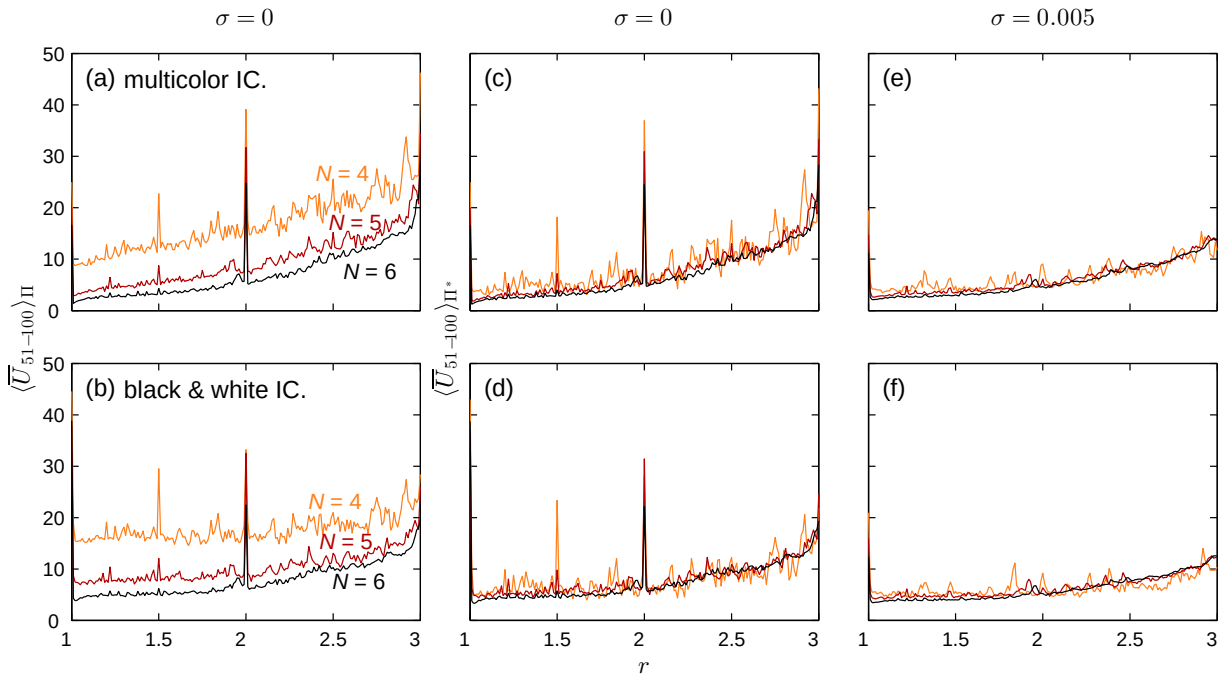

Figure 3.10. $\langle \overline{U}_{51-100} \rangle_{\Pi}$($U_n$averaged across a set of permutations and across iterations 51-100) vs. subsegment length ratio r for N = 4, 5, and 6. Mixing from multicolor initial conditions in (a), (c) and (e), and black and white initial condition in (b), (d) and (f). All irreducible permutations are included in (a) and (b), while only irreducible non-rotational permutations are used in (c)-(f).

permutations decreases as N increases (see Table 3.1). Thus, including rotations in $\langle \overline{U}_n \rangle_{\Pi}$ has a larger effect for smaller N. Therefore, we next consider $\langle \overline{U}_n \rangle_{\Pi^*}$ for irreducible permutations that are not rotations (Π^*) for multicolor initial conditions (Fig. 3.10(c)) and for black and white initial conditions (Fig. 3.10(d)). By excluding rotational permutations, $\langle \overline{U}_n \rangle_{\Pi^*}$ collapses to a single curve for N = 4, 5, and 6, though at some values of r, larger values of N result in slightly better mixing. Considering the fraction of rotations of all irreducible permutations in Table 3.1, it is clear that the large difference in mixing (Fig. 3.10(a,b)) for N = 4 compared to N= 5 or N = 6 for all irreducible permutations simply results from including rotations in the analysis. Furthermore, although the number of irreducible non-rotational permutations for a given N increases rapidly with N (10 for N = 4, 67 for N = 5, and 456 for N = 6), the averaged dependence of the mixing $\langle \overline{U}_n \rangle_{\Pi^*}$ on r is almost

identical. More interestingly, the standard deviation across all irreducible, non-rotational permutations Π^* is comparable in magnitude for all N, regardless of the initial condition, as shown in Fig. 3.11. Thus, comparable mixing on average can be achieved with $N = 4$ as with large N if irreducible non-rotational permutations are used exclusively.

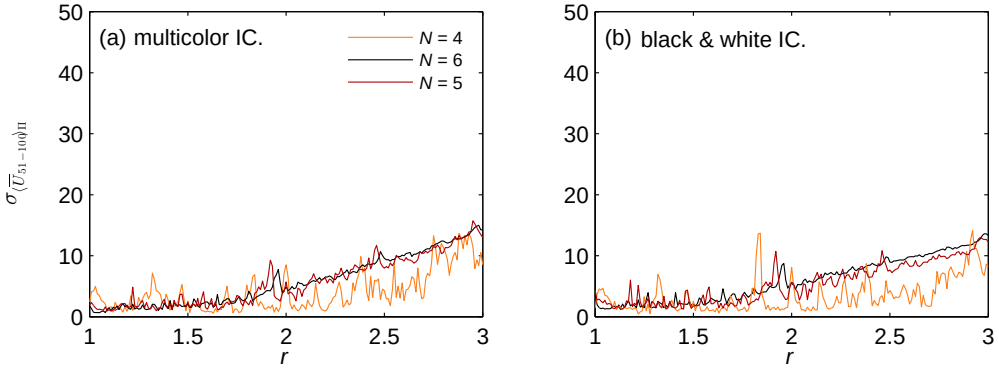

Figure 3.11. Standard deviation of $\langle \overline{U}_{51-100} \rangle_{\Pi^*}$ across all irreducible non-rotational permutations for $N = 4$, 5, and 6, $\sigma = 0$ for (a) multicolor (b) black and white initial conditions.

Finally, we compare the results for cutting and shuffling with and without variation in cut location. In Fig. 3.10(e-f), $\langle \overline{U}_{51-100} \rangle_{\Pi^*}$ is plotted against r for cutting and shuffling with variation in cut location ($\sigma = 0.005$). The overall trend follows that for $\sigma = 0$ (3.10(c-d)) in that $\langle \overline{U}_{51-100} \rangle_{\Pi^*}$ increases as r becomes larger. Most importantly, the "resonance peaks" at $r = 1/1$, $2/1$, $3/2$, and $3/1$ related to reassembly are eliminated by random variation in cut location. However, mixing improves only slightly for other values of r for both the multicolor initial conditions and the black and white initial condition. This again demonstrates that variation in cut location selectively enhances mixing and results in a similar effect as a closer-to-irrational r so long as the number of iterations is less than the reassembly period. Therefore, significant mixing over a finite time can be achieved even when r is the ratio of small integers (has a continued fraction expansion of length less than or equal to 2) provided that $\sigma \neq 0$. Finally we note that the small peaks in $\langle \overline{U}_{51-100} \rangle_{\Pi^*}$ in Fig. 3.10(e-f) are inherent structures rather than fluctuations from randomness in cut location variation evident for U_n

in Fig. 3.4(c), since they persist for different samples of the underlying distribution of cut location variation.

3.4. Conclusions

Cutting and shuffling a line segment generates surprisingly complex dynamics by varying only a few parameters. Small random perturbations to the dynamical system can enhance mixing. In particular, we have shown that variation in cut location improves mixing by varying the subsegment lengths every iteration so that, on average, they act as if they are rationally independent. Even though mixing is not significantly improved by varying the cut locations for IETs with closer-to-irrational subsegment length ratios, the periodicity of the dynamics is destroyed by perturbing the cuts. In addition to improving mixing by allowing variation in cut location, we also showed that the average dependence on subsegment length ratio for irreducible non-rotational permutations is almost identical for $4 \leq N \leq 6$. Pathological cases were also identified where mixing remains poor even with variation in cut locations for reducible and irreducible rotational permutations, as well as for permutations with a sequence of consecutive elements. Thus, the impact of introducing variation in cut locations depends on the fundamental dynamics of the protocol, which is more evident for irreducible non-rotational permutations not having consecutive sequences of elements.

In general, good mixing can be reliably obtained in finite time for IETs with the following characteristics:

(i) The rearrangement order should be an irreducible non-rotational permutation without sequences of consecutive elements.

(ii) The ratio of adjacent subsegment lengths should be close to 1.

(iii) Either the ratio of adjacent subsegment lengths should be irrational (or "closer-to-irrational") or there should be slight random variation in cut location.

Other methods to perturb the IET dynamical system include randomly choosing permutations for each iteration or distributing cuts randomly in the entire line segment, both of which would be appropriate subjects for future research.

We have demonstrated that it is possible to achieve significantly enhanced practical mixing with irreducible non-rotational permutations by randomly perturbing the cut locations when compared to the unperturbed protocol. This framework of mixing (cutting and shuffling with randomly perturbed cut locations) provides a point of departure for developing practical engineering processes with enhanced mixing properties.

Varying cut locations can also be applied to a three-dimensional PWI, for example one obtained by cutting and shuffling a hemisphere, which is a dynamical framework for flow in a biaxial spherical tumbler [78, 24, 101]. On the other hand, application of variation in cut location to arbitrary two dimensional PWI has limitations that depend on the geometry. In the example of the isosceles triangle PWI [53], the cut can only be made at one position for the isosceles subtriangles to reassemble into the original shape. However, it is possible to construct a 2D PWI by cutting and shuffling a square as shown in Fig. 3.12, using the "kindergarten" method [122] in which construction paper is manually cut and shuffled. Essentially, one iteration of 2D cutting and shuffling consists of a 1D interval exchange transformation in the horizontal direction (rectangles are shuffled in the horizontal direction) followed by another interval exchange transformation in the vertical direction (rectangles are shuffled in the vertical direction). In Fig. 3.12, the red lines indicate the cuts for each iteration, first vertical and then horizontal ($N = 4$ in each operation). The two dimensional PWI shown in Fig. 3.12 is likely to follow similar guidelines for good mixing to those for the 1D IET examined in this dissertation, but this is left to future work.

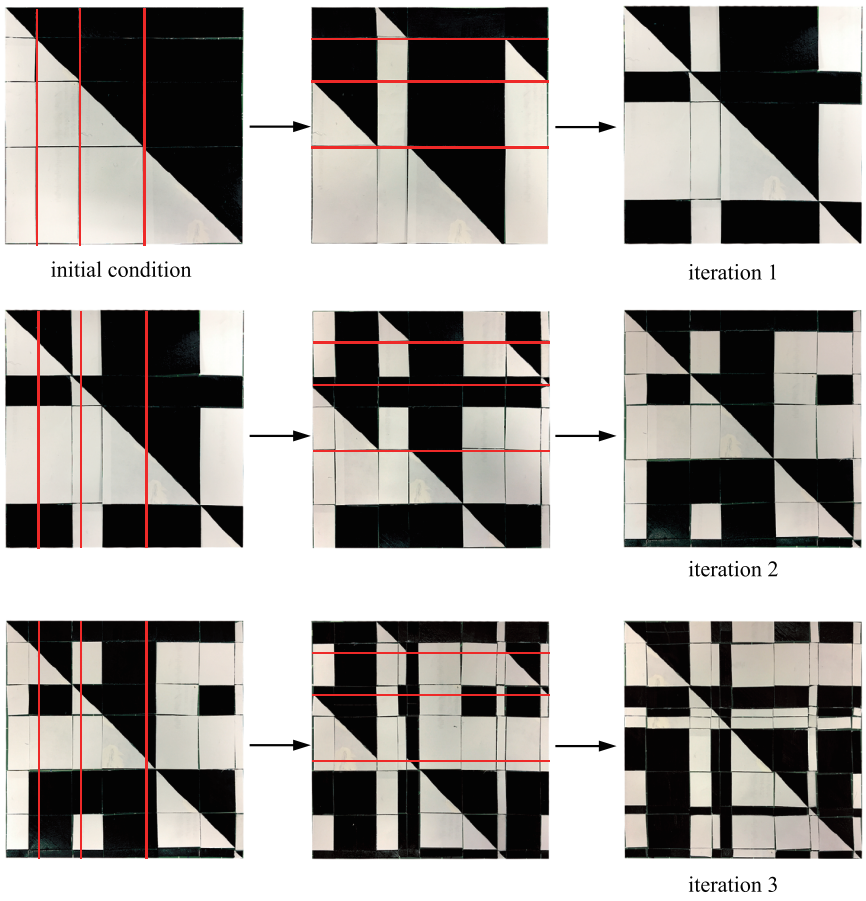

Figure 3.12. Rectangle exchange transformation of a diagonal two component initial condition realized manually using construction paper. Each row represents one iteration of cutting and shuffling, first in the vertical direction, and then in the horizontal direction. The analogous protocol used here is $\Pi = [3142]$, $r = 1.5$ with no intentional variation in cut location.

CHAPTER 4

Persistent non-mixing structures in BST flow

SUMMARY

Thorough mixing of granular materials in a 3D geometry appears to be simple. However, rotating a geometrically simple 3D tumbler, a sphere, about a single axis only produces slow mixing through diffusion. Rotating the spherical tumbler alternately about two different horizontal axes generates complex dynamics with the possibility of enhanced mixing. The unique flow kinematics of granular materials resemble those of a Bingham plastic. Granular materials in a rotating tumbler in the presence of gravity only flow near the free surface while the majority of material rotates rigidly with the tumbler. Non-destructive x-ray imaging allows continuous tracking of particles that demonstrates regular non-mixing regions coexist with chaotic mixing regions. These dynamical structures can be understood by studying the interplay between stretch-and-folding in the flowing layer and the solid rearrangement of cutting-and-shuffling formalized in terms of piecewise isometries (PWI). In the presence of stretching-and-folding in the flowing layer and collisional diffusion, structures of periodic non-mixing islands persist in the continuum model, resulting in mixing barriers. This chapter demonstrates that dynamical systems analysis not only can be applied to fluid mixing, but also to granular flows, particularly in flows with both static and flowing regions. Understanding the fundamentals of mixing dynamics of the underlying flow in the BST sets the stage for further investigation into the interaction of mixing and segregation.

This chapter is based on the publication "Persistent structures in a three-dimensional dynamical system with flowing and non-flowing regions" by Zafir Zaman, Mengqi Yu, Paul P. Park, Julio M. Ottino, Richard M. Lueptow, and Paul B. Umbanhowar, *Nat Commun*, **9**,

3122 (2018) [173] ©2018 Springer Nature. This work is a collaboration with Zafir Zaman and Paul Park. Zafir Zaman designed and built the original x-ray imaging equipment. Zafir Zaman designed the tumbling apparatus and I worked with him to build and test it (see Chapters 4-5 in [174] for details of the x-ray equipment). I also developed the continuum model simulations. Zafir and I performed the experiments and analyzed results. Paul Park developed the BST PWI model and methods for model simulations.

4.1. Introduction

The goal of mixing is to rearrange initially segregated matter into states where the constituent elements are homogeneously distributed. In fluids, where the elements are atoms or molecules, mixing at low Reynolds numbers can be achieved by the stretching-and-folding of chaotic flows combined with thermal diffusion which drives mixing at the smallest length scales [167, 87, 113]. In bulk solids composed of macroscopic (athermal) particles, the particles can be deliberately rearranged, as in the cutting-and-shuffling of a deck of cards [154]. Other rheological materials–Bingham fluids and polymer mixtures [175] for example–fall between these two extremes.

While mixing of fluids and mixing of solids have long histories and are relatively mature fields, little is understood about mixing when flowing and non-flowing regions coexist, especially in three-dimensions (3D). For example, in yield stress materials, constituent elements move together as a solid where local stresses are low, but flow in relative motion where the yield stress is exceeded. Common examples of yield stress materials include paint, concrete paste, polymer mixtures [175], and granular materials, e.g., sand. Understanding 3D mixing in such materials is critical in many domains where variations in local concentration can be disastrous, including the pharmaceutical industry [108], composite materials [160], and concrete manufacturing. Understanding when and how flowing and non-flowing regions interact in the presence of both stretching-and-folding and cutting-and-shuffling will likely lead to new and more effective mixing methods that take advantage of both mechanisms simultaneously. An amusing but noteworthy example of mixing in a system with flowing and non-flowing regions is the Spanish Christmas Lottery (the second longest continuously running lottery with the largest payout in the world), where 100,000 wooden balls are mixed within a 2 m diameter sphere rotated about a horizontal axis with the expectation of randomness [163]. Our results show that this expectation cannot be taken for granted.

To study the interaction of mixing by stretching-and-folding with mixing by cutting-and-shuffling, we consider a geometrically simple 3D model system with localized flow — a spherical tumbler half-filled with a dry granular material and rotated alternately about orthogonal horizontal axes. Experiments with this system demonstrate the existence and extraordinary persistence of non-mixing island structures due to cutting-and-shuffling for many different experimental protocols even in the presence of diffusion and flowing regions. To understand the structure, we employ the mathematics of piecewise isometries to predict the geometric skeleton of the mixing and non-mixing regions, demonstrating that for a range of tumbling protocols, the mixing structure is a fundamental consequence of the dynamics of cutting-and-shuffling. We further utilize a continuum model that connects the solids mixing by cutting-and-shuffling with fluid-like mixing by stretching-and-folding. This model fully captures the mixing and non-mixing regions observed in the experiments and provides insight into the interaction between stretching-and-folding and the underlying structure of the dynamical system based on cutting-and-shuffling.

4.2. Results

4.2.1. Persistent periodic structures

In a tumbler, (a common device used in many industrial processes such as particle mixing, coating, and drying), particles flow in a relatively thin layer at the free surface, while below the surface in the non-flowing bed, particles move together in solid body rotation about the rotation axis, see Fig. 4.1. To mix the granular material in our half-filled $D(= 2R_o) = 14\,\text{cm}$ diameter spherical tumbler, the tumbler is rotated alternately about orthogonal horizontal axes by angles (θ_z, θ_x) beyond the repose angle of the granular material, β [101]. To characterize the mixing, we use x-ray imaging to track the location of a 4 mm diameter spherical tracer particle in a bed of 2 mm diameter glass spheres after each iteration for a wide range of protocols [i.e., (θ_z, θ_x) pairs], details are provided in the Appendix B. The larger diameter

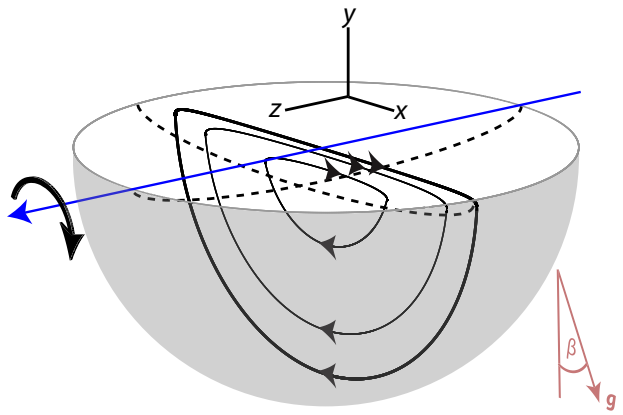

Figure 4.1. Spherical tumbler geometry and flow. Sketch showing three representative particle trajectories (curves with arrowheads) in the flowing layer and in solid body rotation in a plane normal to the free surface and perpendicular to the z-rotation axis. The two dashed curves show the lower boundary of the flowing layer in planes normal to the free surface and parallel and perpendicular to the rotation axis.

tracer particle flows on the free surface and is subsequently deposited in the bed near the tumbler wall.

Using our experimental apparatus, we consider first the itinerary of the tracer particle for an example protocol when the spherical tumbler is alternately rotated by 57° about orthogonal horizontal axes [a $(57°, 57°)$ protocol] for 500 iterations. The position of the tracer particle viewed from the bottom of the spherical tumbler after each iteration (small circles) is shown in Fig. 4.2(a). After each iteration the tracer particle is alternately displaced between three distinct regions as indicated by the gray lines between the tracer particle positions. In this run, the tracer particle never departs from these three non-mixing regions (islands) despite collisions with other particles that drive random collisional diffusion, and other minor experimental errors including small variations in the rotation angle. These effects, however, can play a role. Figure 4.2(b) shows a second 500 iteration experiment under the same conditions for which the tracer particle moves periodically between the same three regions (blue points) but also between a second set of period-3 regions (red points) and aperiodically (black points). The aperiodic motions, where the tracer particle is not in one of the two

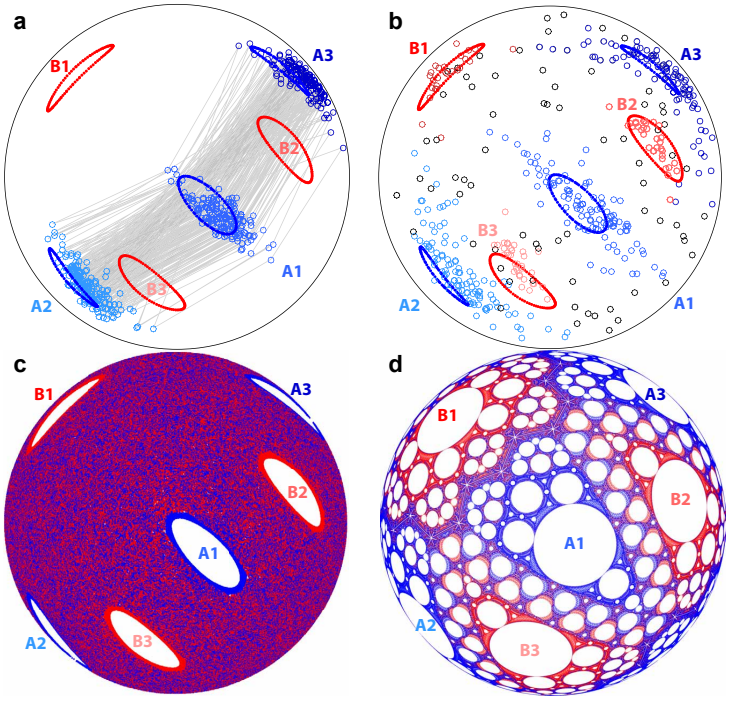

Figure 4.2. Period-3 non-mixing regions under the $(57^o, 57^o)$ protocol. (a) In one experiment, the tracer particle cycles between period-3 regions A1-A3 (blue circles) with stroboscopic paths (gray lines) for 500-iterations of the protocol. (b) In a second experiment with the same macroscopic initial conditions, the tracer particle cycles between period-3 regions A1-A3 (blue circles) for 326 iterations (1-90, 96-331), period-3 regions B1-B3 (red circles) for 101 iterations (386-486), and outside of period-3 regions (black circles) for 73 iterations (91-95, 332-385, and 487-500). (c) Passive tracers in the finite flowing layer (FL) model mix everywhere except in two sets of period-3 regions (A1-A3 and B1-B3), whose boundaries are superimposed on the experimental data in (a,b). (d) The piecewise isometry model (PWI), which describes solids mixing by cutting-and-shuffling, predicts unmixed cells (white regions) of which only the largest cells, (A1-A3, B1-B3) persist in the continuum model (c). Period-3 trapping regions from experiments correspond with period-3 cells from the continuum and PWI models [blue (red) curves for regions A1-A3 (B1-B3)]. Bottom-views ($+y$-direction) shown in all panels.

sets of period-3 regions, occur in only 73 of the 500 iterations but allow the tracer particle to move from one set of period-3 regions (blue) to the other set (red) and back. Similar period-3 non-mixing regions are observed in the 'nearby' protocols $(54^o, 54^o)$ and $(60^o, 60^o)$.

To better understand the existence of these non-mixing and mixing regions, we first consider the predictions of a standard and simple advection based continuum model [101] for flow in a half-filled tumbler. In the model (see Appendix C), particles flow down the

surface in a thin flowing layer that lies on top of non-flowing particles in the bulk that move in solid body rotation with the tumbler. For rotation about any axis (the z-axis here with x in the streamwise direction and y normal to the free surface), the non-dimensionalized velocity field $\mathbf{u} = (u, v, w)$ is piecewise defined such that the flowing layer ($0 \geq y \geq -\delta$) velocity is $\mathbf{u}_{\text{fl}} = ((\delta + y)/\epsilon^2, xy/\delta, 0)$ and the bulk ($y < -\delta$) solid body rotation velocity is $\mathbf{u}_{\text{b}} = (y, -x, 0)$. The interface of the lenticular flowing layer with the bulk is located at $\delta(x, z) = \epsilon\sqrt{1 - x^2 - z^2}$, where $\epsilon = \delta(0, 0) = \sqrt{\omega/\dot{\gamma}}$ is the maximal dimensionless flowing layer depth at the center of the sphere ($x = z = 0$) for shear rate $\dot{\gamma}$ and angular rotation velocity ω. All variables are dimensionless—lengths are normalized by the tumbler radius R_o and the rotation period T is normalized by $1/\omega$. This flowing layer (FL) continuum model, which includes stretching characteristic of chaotic flows [113], is parameterized by the flowing layer depth ϵ, which is set to 0.15 to match the conditions in the experiments (see Appendix C).

To characterize mixing in the continuum model, blue passive tracer points are seeded at the intersection of the flowing layer boundary δ and a hemispherical subshell having normalized radius $r = 0.9$ (Radius $r = 0.9$ was used to mimic tracer particle position in experiments as elliptic regions at larger $r > 0.9$ reveal more intricate structures not apparent in experiments likely due to particle size effects and collisional diffusion. As the intricate elliptic regions at $r > 0.9$ occur at the same location on the hemispherical shell as elliptic regions at $r = 0.9$, we use the elliptic orbits at $r = 0.9$ for comparison to experiment.) before the first rotation, while red points are seeded in the same location after a half-iteration (i.e., rotation about the z-axis). In Fig. 4.2(c), the Poincaré (stroboscopic) map (see, e.g., Ref. [152]) of tracer points advected by the continuum model under the same conditions as the experiment [Fig. 4.2(a)] displays uniform mixing throughout the domain except for six empty regions. These empty regions correspond to two sets of period-3 regions (A1-A3 and B1-B3): a point initially in A1 cycles to A2 in the next iteration, to A3 in the following

iteration, and then back to A1. Overlaying the non-mixing regions in Fig. 4.2(c) on the experimental tracer results in Fig. 4.2(a,b) shows that they correspond to the regions in experiments where the tracer particle lingers.

Although the continuum model captures the main features of the experiments shown in Fig. 4.2(a,b), deeper insight into why persistent period-3 structures form under the $(57^o, 57^o)$ protocol (and period-n structures for other protocols) is gained from a perspective based exclusively on solids mixing by cutting-and-shuffling. This is accomplished by taking the $\epsilon \to 0$ limit (an infinitely thin flowing layer). In this theoretical limit, particles instantaneously jump across the free surface to a downstream point symmetric about the midpoint of the free surface and, consequently, undergo only solid body rotation. Since there is no shear in the flowing layer for a half-filled tumbler, the biaxial mixing protocol in the $\epsilon \to 0$ limit corresponds to a radially invariant hemispherical domain with mixing dynamics that are equivalent to slicing the hemisphere into four pieces that are rearranged and then reassembled into a hemisphere again. This type of transformation is called a piecewise isometry (PWI) [81, 50, 53, 54, 80] and it has found use in several applications [27, 6, 142, 141, 147]. Here, and similar to the continuum model, the boundaries formed by the slicing after a rotation about a single axis are used as initial conditions for tracer points whose trajectories form a subset of the exceptional set [47], which is the skeleton for transport dynamics in PWI systems. Blue tracers are seeded where the domain is cut by the action of the θ_z rotation, while red tracers are seeded where the domain is cut by the θ_x rotation. The mixing mechanism for PWI is simply cutting-and-shuffling in analogy with mixing a deck of cards [2, 157], but this does not prevent PWI from possessing complicated dynamics [53, 54, 80, 52, 7]. In fact, the hemispherical piecewise isometry system described here has several interesting properties including non-mixing regions [122, 149], resonances corresponding to non-mixing regions [145], and a fractal nature [121].

Similar to the continuum model, repeated iteration of the four piece PWI model for the $(57^o, 57^o)$ protocol [Fig. 4.2(d)] generates open regions devoid of tracers, known as cells. These cells vary in size and periodicity across the domain, with certain areas dominated by a particular color of tracer particle. The largest circular cells have the lowest periodicity. The one-to-one correspondence in size and location between the largest cells in the PWI model (A1-A3 and B1-B3), the elliptical domains in the continuum model [Fig. 4.2(c)], and the non-mixing regions in the experiments [Fig. 4.2(a,b)] is remarkable. This agreement suggests that the periodic regions observed in experiment for the $(57^o, 57^o)$ protocol result from the solids mixing structure generated by cutting-and-shuffling, and that it is the cutting-and-shuffling that prescribes the underlying structure, or 'skeleton' of the mixing.

4.2.2. Dependence on rotation protocol

The periodicity, as well as the size and location, of non-mixing structures depends on the rotation protocol. For example, consider the results for the $(90^o, 90^o)$ protocol, which has period-2 non-mixing regions, shown in Fig. 4.3. In experiment [Fig. 4.3(a)], a tracer particle seeded in the A1 region, cycles between A1 and A2 and between B1 and B2 for a total of 263 and 46 iterations, respectively, for a 500-iteration experiment. Compared to the period-3 non-mixing regions under the $(57^o, 57^o)$ protocol in Fig. 4.2, the tracer escapes more frequently from the period-2 non-mixing regions. Again, the non-mixing regions (A1-A2 and B1-B2) correspond well with the islands in the continuum model [Fig. 4.3(b)], while in the PWI model [Fig. 4.3(c)] the four non-mixing regions occupy the entire domain since the entire hemisphere returns to its initial condition every two iterations. As with the $(57^o, 57^o)$ protocol, this is presumably the case because the finite-depth flowing layer in experiment and the continuum model converts a portion of the PWI model's non-mixing regions into mixing regions by virtue of stretching in the flowing layer [149], a point we return to below.

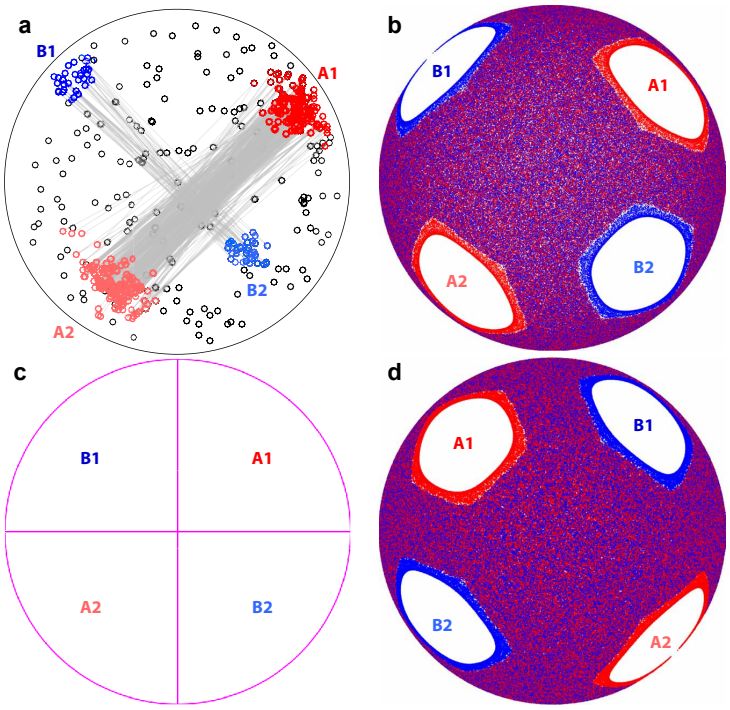

Figure 4.3. Period-2 non-mixing regions under the $(90^o, 90^o)$ protocol. (a) Tracer particle in a 500-iteration experiment appears in period-2 regions A1-A2 (red circles) for 263 iterations (mean 38 iterations per instance) and B1-B2 (blue circles) for 46 iterations (mean 12 iterations per instance), stroboscopic paths indicated by gray lines. (b) In the continuum model, two sets of period-2 regions (A1-A2 and B1-B2) exist. (c) The PWI model undergoes trivial period-2 rearrangement of the entire domain. (d) Interchange of non-mixing A and B regions in the continuum model at 500 plus one-half-iteration illustrates the generic (i.e., protocol independent) half-period offset relationship between A and B non-mixing regions.

For the half-full spherical tumbler mixed by alternating rotations about orthogonal axis, persistent non-mixing period-n regions always appear in pairs, which is a manifestation of the relationship between the full and half-iteration structures. For example, the two sets of non-mixing regions in Fig. 4.3(b) swap positions [Fig. 4.3(d)] upon an additional half-cycle of the mixing protocol. Thus, the B-set of non-mixing regions is the half-period offset of the A-set of non-mixing regions and *vice versa*.

Both PWI and continuum models capture the gross features of the large scale persistent mixing and non-mixing structures observed in experiments for the two protocols we have examined so far. However, they do not describe transitions of the tracer particle into and out

of the islands seen in experiments, e.g., Fig. 4.2(b) and Fig. 4.3(a). This is because particle diffusion, which is driven by particle-particle collisions in granular flows, is not included in either model so that the underlying structure of the mixing is evident. The collisional diffusion coefficient for flowing macroscopic particles scales as $d^2\dot{\gamma}$ where d is the diameter of the particles in the tumbler and $\dot{\gamma}$ is the shear rate [161]; in our tumbler and on average, diffusion randomly displaces a particle in the spanwise direction by ∼d per flowing layer pass [172]. For the $(57^o, 57^o)$ protocol which produces ∼1 flowing layer pass per iteration, the root-mean-square displacement after 500-iterations is $d\sqrt{500} \approx 4.5\,\text{cm}$, which is a bit more than half the tumbler radius. Based on the size of the non-mixing regions under the $(57^o, 57^o)$ protocol, we expect a mean residency time of about 350 iterations in the regions, which is on the order of the observed residence times of at least 500 iterations in Fig. 4.2(a), 326 iterations for the period-3 A regions in Fig. 4.2(d), and 101 iterations for the period-3 B regions in Fig. 4.2(d). Consequently, we expect particles in experiments to 'leak' out of non-mixing regions with a residence time that decreases as the square root of the size of the non-mixing regions. This is likely why smaller islands predicted by the continuum and PWI models are not evident in the periodic orbits of the tracer particle in experiment. What is remarkable, though, is that even though diffusion is intrinsic in the experiments, it has minimal impact. Even with diffusion in the experiments, the tracer particle remains in the non-mixing region [Fig. 4.2(a)] or returns to the non-mixing region after being bumped out of it by diffusion (Figs. 4.2(b) and 4.3(b)]. Thus, the fundamental structure of the flow (non-mixing regions predicted by the continuum model or the PWI) dominates in spite of diffusion.

To further illustrate the minimal influence of diffusion on particle motion, Fig. 4.4 shows the motion of 100 tracer particles starting inside and outside an island for the $(57^o, 57^o)$. The tracers follow the advective flow field defined by the continuum model but in addition undergo a random walk while in the flowing layer with a mean step size per flowing layer

pass of d. After twelve iterations of protocol, most of the tracers starting within the island are still within the island, while tracers starting outside the island are dispersed over the hemisphere. Thus, the chaotic mapping of tracer particles outside the island dominates the collisional diffusion. Similar results are obtained for tracer points with added diffusion in the PWI model.

Non-mixing islands in a background of mixing are the most common but not the only possibility; some protocols can produce nearly completely mixed domains. For example under the rotationally asymmetric $(75^o, 60^o)$ protocol (Fig. 4.5), the tracer particle explores most of the domain in experiments [Fig. 4.5(a)], while the continuum [Fig. 4.5(b)] and PWI [Fig. 4.5(c)] models generate mixing regions that completely and nearly completely, respectively, fill the domain. Note that, complete mixing is not guaranteed by an asymmetric protocol, i.e., $\theta_z \neq \theta_x$, and, conversely, a symmetric protocol, i.e., $\theta_z = \theta_x$, does not guarantee the existence of non-mixing regions.

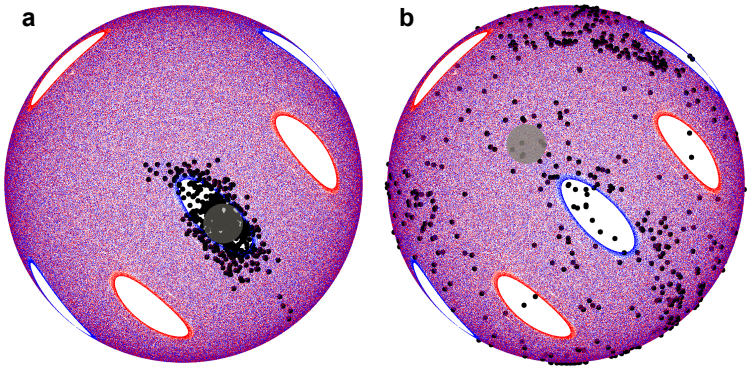

Figure 4.4. Influence of collisional diffusion. Comparison of the motion of 100 tracer particles under the $(57^o, 57^o)$ protocol with collisional diffusion and initially located (gray circle) (a) within an island and (b) outside an island. After twelve iterations of the protocol, most of the particles initially located (a) within the island remain, while particles initially located (b) outside the island are distributed over the entire hemisphere due to chaotic mixing.

Barriers to mixing

Under the three protocols used in Figs. 4.2-4.5, the non-mixing regions in experiments, also exist in the continuum model and the PWI model (where they correspond to the largest cells). In contrast, under the $(45^o, 45^o)$ protocol [Fig. 4.6], a mixing barrier emerges that divides the hemisphere into two regions and is not obviously captured by the PWI model. A tracer particle in two experiments [Fig. 4.6(a,b)] follows two different extended finger-like period-3 structures that are separated by a leaky barrier to particle transport and, together, cover the entire domain. These interdigitated period-3 structures are readily apparent in the continuum model [Fig. 4.6(c)]. Red and blue tracers each dominate half of the domain with an elongated non-mixing region in each 'finger,' which roughly corresponds to the tracer particle positions from experiment. The region dominated by blue tracers appears to have only two 'fingers.' The third 'finger' is mostly contained in the flowing layer, which is not visible in the view shown in Fig. 4.6(c), though the blue edges of this 'finger' are evident at the periphery of the domain as well as the periphery in the experiments [Fig. 4.6(b)]. For the equivalent half-iteration structures in the continuum model, the red tracer dominated regions alternate with the regions dominated by blue tracers with one of the red 'fingers'

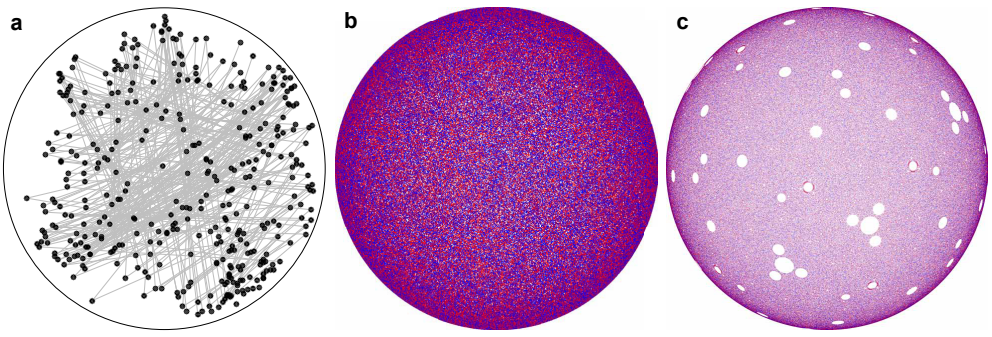

Figure 4.5. Mixing under the $(75^o, 60^o)$ protocol. (a) Tracer particle positions (black points) and stroboscopic paths (gray lines) in a 500-iteration experiment continuously explore nearly the entire domain with no obvious periodic (non-mixing) regions. (b) In the corresponding FL model, tracers are mixed throughout the domain, consistent with the experiment. (c) The PWI model predicts a mostly mixed domain with a few small cells that are indiscernible in the experiment and FL model.

mapped to the flowing layer. To delineate the two regions, we followed a tracer point in the continuum model seeded between the red and blue tracer dominated regions to produce the grey points superimposed on the experimental data in Fig. 4.6(a,b). The path of this tracer suggests a mixing barrier that wraps around the entire domain.

Unlike the PWI model structures for protocols shown in Figs. 4.2-4.5, the structure generated by the PWI model under the $(45^o, 45^o)$ protocol [Fig. 4.6(d)] is less clearly related to the experiment and the continuum model as it lacks the typical large cells that manifest as non-mixing regions in the experiment. Instead the PWI model generates large arrowhead-like features consisting of multiple small cells with transport barriers between adjacent red and

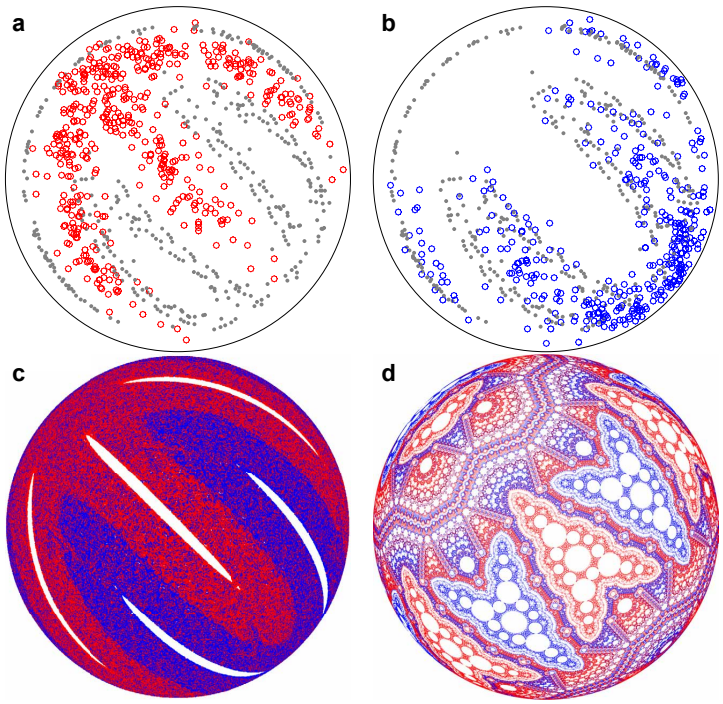

Figure 4.6. Period-3 mixing barrier between two halves of the domain for the $(45^o, 45^o)$ protocol. (a,b) In 500-iteration experiments, the tracer particle (red and blue circles) cycles through two distinct parts of the domain every three periods depending upon its initial location. (c) The corresponding FL model has two thin sets of period-3 islands corresponding to the structure in experiment (a,b) [red islands in (c) correspond to red 'fingers' in (a) and blue islands in (c) correspond to blue 'fingers' in (b)]. The two sets of islands in experiment are separated by a mixing barrier (grey points in (a,b) which are extracted from the continuum model). (d) The PWI model predicts two sets of period-3 arrowhead patterns.

blue arrowheads. However, the colors and positions of the arrowhead features correspond to the 'finger' features in the experiment and FL model.

4.2.3. Dependence on flowing layer depth

The structures generated by the continuum model match experimental observations regardless of the protocol, while those predicted by the PWI model are not always evident in experiment or the continuum model. For example, the small non-mixing cells in the PWI model for the four protocols we examine above are missing in results from experiments and the continuum model. As explained above, lack of fine structure is expected in experiments where granular diffusion is present, but this does not explain their absence from the diffusionless FL model. To better understand the relationship between the non-mixing structures in the PWI and FL models, particularly for the $(45^o, 45^o)$ protocol, we consider the influence of the flowing layer depth. Physically, the flowing layer depth increases with rotation rate ω and decreases with shear rate $\dot{\gamma}$, since $\epsilon = \sqrt{\omega/\dot{\gamma}} = \delta(0,0)/R$ [43], and is typically ~ 10 particle diameters in experiments. As Fig. 4.7 shows, non-mixing regions shrink and, in most cases, vanish with increasing flowing layer depth in the continuum model. Nearly all cells present in the PWI model (i.e., $\epsilon = 0$) disappear under the $(57^o, 57^o)$ and $(45^o, 45^o)$ protocols at $\epsilon = 0.2$ and $\epsilon = 0.1$, respectively, while under the $(90^o, 90^o)$ protocol, cells shrink but persist up to the largest ϵ examined.

Focusing on the $(45^o, 45^o)$ protocol [Fig. 4.7(c)], the cells present at $\epsilon = 0$ shrink and eventually annihilate with increasing ϵ. However, new structures emerge for larger ϵ, characterized by both non-mixing regions and a mixing barrier between red and blue tracer particles. In particular, at $\epsilon = 0.15$, the leftmost red 'finger' and its central non-mixing region land in the flowing layer after a half-iteration, while each of the subsequent red 'fingers' map to the flowing layer one iteration apart. The same phenomenon occurs for the blue 'fingers' except on full iterations. The flowing layer acts as a mixing barrier in the $(45^o, 45^o)$

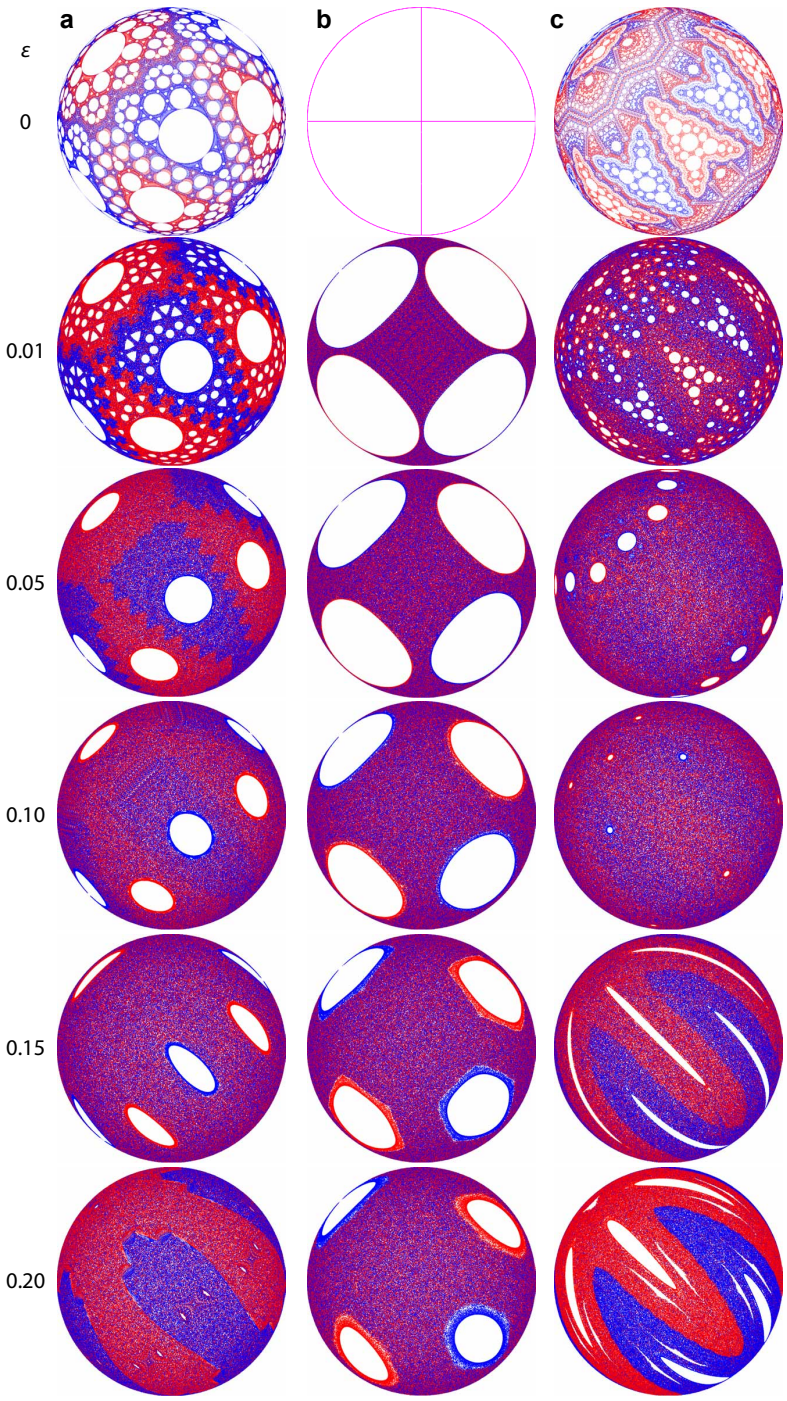

Figure 4.7. Effect of flowing layer depth on non-mixing regions. Three different protocols are examined (columns): (a) $(57^o, 57^o)$, (b) $(90^o, 90^o)$, and (c) $(45^o, 45^o)$. With increasing flowing layer depth, ϵ (rows), non-mixing regions formed by cutting-and-shuffling ($\epsilon = 0$) shrink in (a-c) and disappear in (a,c), while new non-mixing regions originating from stretching-and-folding in the finite depth flowing layer appear and grow in (c) for $\epsilon \geq 0.15$.

protocol as each part of the fixed bed lands in the flowing layer during a change in the rotation axis. This behavior is not unique to the $(45^o, 45^o)$ protocol as Fig. 4.8 illustrates for the $(45^o, 15^o)$ protocol. Here, the experiments show evidence for two sets of period-4 islands separated by a mixing barrier. Again, the continuum model shows that these features emerge for finite ϵ.

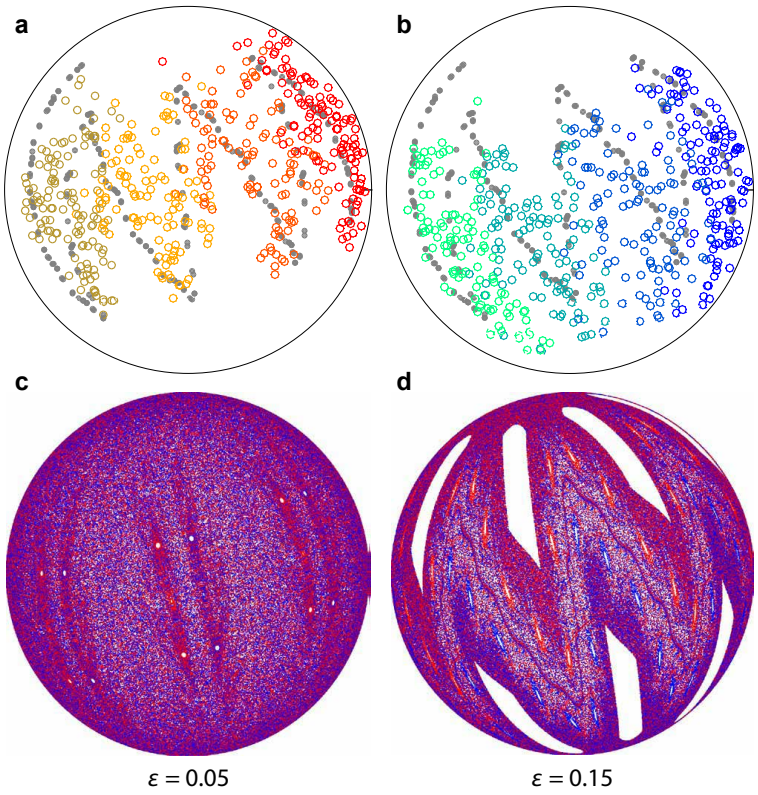

Figure 4.8. Weak elliptic non-mixing barrier around period-4 regions under the $(45^o, 15^o)$ protocol. (a,b) The tracer particle in 500-iteration experiments only occasionally crosses the mixing barrier (grey points). Color map illustrates the period-4 cycle. (c) Non-mixing regions are not evident for $\epsilon = 0.05$ but become prominent with increasing flowing layer depth in the continuum model.

4.2.4. Motion of persistent vs. emergent non-mixing regions

The primary difference between non-mixing regions present at $\epsilon = 0$ that persist for $\epsilon > 0$ and non-mixing regions that emerge only for $\epsilon > 0$ is that the persistent regions completely exit the flowing layer at the end of a rotation while the emergent regions are always fully

contained within the flowing layer at the end of a rotation. This difference is illustrated in Figs. 4.9 and 4.10 (and in Supplemental Movies 1[1] and 2,[2] respectively) which depict the usual images of the hemispherical bottom surface viewed from below, plus images of the free surface of the flowing layer viewed from below in order to visualize the passage of the non-mixing region through the flowing layer. In addition to images at the full iteration (500+), these figures also include images of both surfaces during and just after completing the first rotation of the 501^{st} protocol (i.e., $500\frac{1}{2}+$).

Viewed in this way, Fig. 4.9 reveals two generic features of persistent non-mixing regions [illustrated here for the (57^{o}, 57^{o}) protocol]. First, persistent non-mixing regions pass entirely through the flowing layer during each rotation, regardless of the flowing layer depth, which rearranges ('shuffles') them on the hemisphere. Second, their boundaries are set by the boundary of the flowing layer during the interchange of rotation axes (the 'cut'). This is particularly evident in Supplemental Movie 1, but can also be seen in Fig. 4.9. At 500+ iterations, non-mixing regions A2 and A3 are just touching the circular edge of the flowing layer. Between iteration 500+ and $500\frac{1}{2}$, corresponding to the first 57^{o} rotation of the iteration, non-mixing regions A2 and B1 are stretched as they pass through the flowing layer. At $500\frac{31}{100}$ the flowing layer image shows B1 stretched completely across the the flowing layer while only the trailing portion of A2 is visible as it finishes crossing the flowing layer. In the subsequent half-iteration, A2 and B3 pass through the flowing layer in the direction of the arrow.

Returning to the case of emergent structures that appear only for $\epsilon > 0$, Fig. 4.10 illustrates [using the $(45^{\text{o}}, 45^{\text{o}})$ protocol] that their motion is quite different from that of persistent islands. First, emergent islands periodically land entirely within the flowing layer at the end of a rotation and are stretched in the streamwise direction. Subsequent rotation about the orthogonal axis stretches them in the opposite direction before they return to the

[1]Link to Movie 1
[2]Link to Movie 2

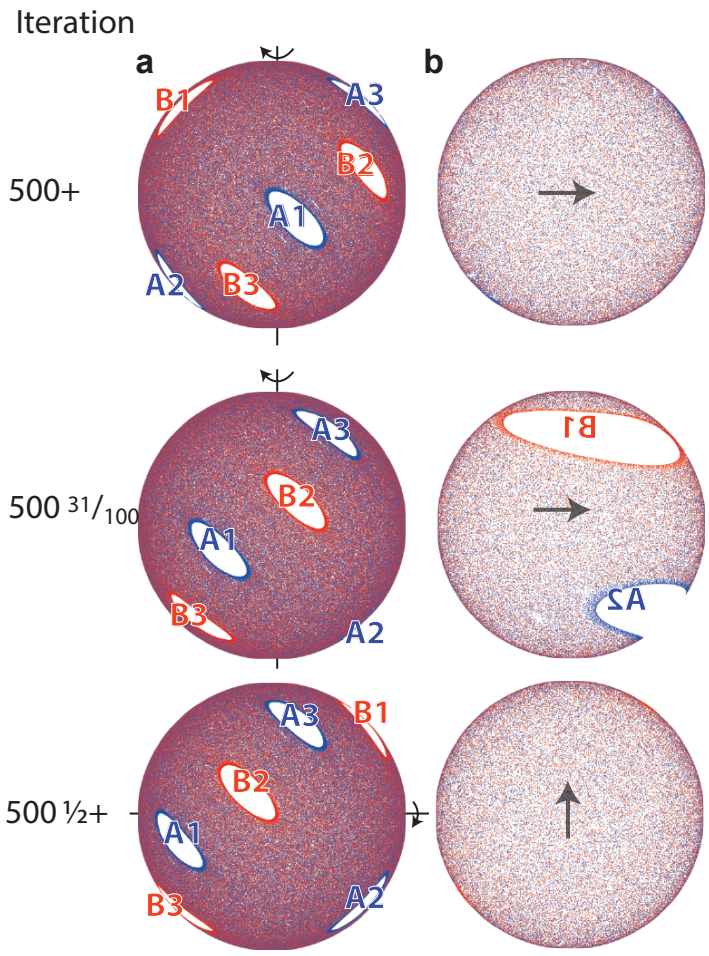

Figure 4.9. Movement of persistent non-mixing regions through the flowing layer. Non-mixing regions (A1-A3, B1-B3) present at $\epsilon = 0$ [see Fig. 4.7(a)] are still present at $\epsilon = 0.15$ and pass fully through the flowing layer after each half-iteration [$(57^o, 57^o)$ protocol]. Views from below of the hemispherical shell (a) and the planar flowing layer (b). Labels of periodic regions illustrate changes in orientation and arrows indicate the direction of flow in the flowing layer. Animations are provided in Supplementary Movie 1.

bulk. Second, their boundaries are not necessarily coincident with the flowing layer boundary at the end of a rotation. Third, the boundary of the mixing barrier (between red and blue 'fingers') maps approximately to the boundary of the flowing layer as shown by the mostly blue flowing layer at 500+ iterations and the mostly red flowing layer at $500\frac{1}{2}+$ iterations. However, the mixing barrier between red and blue regions is less clearly defined than the white non-mixing region boundaries.

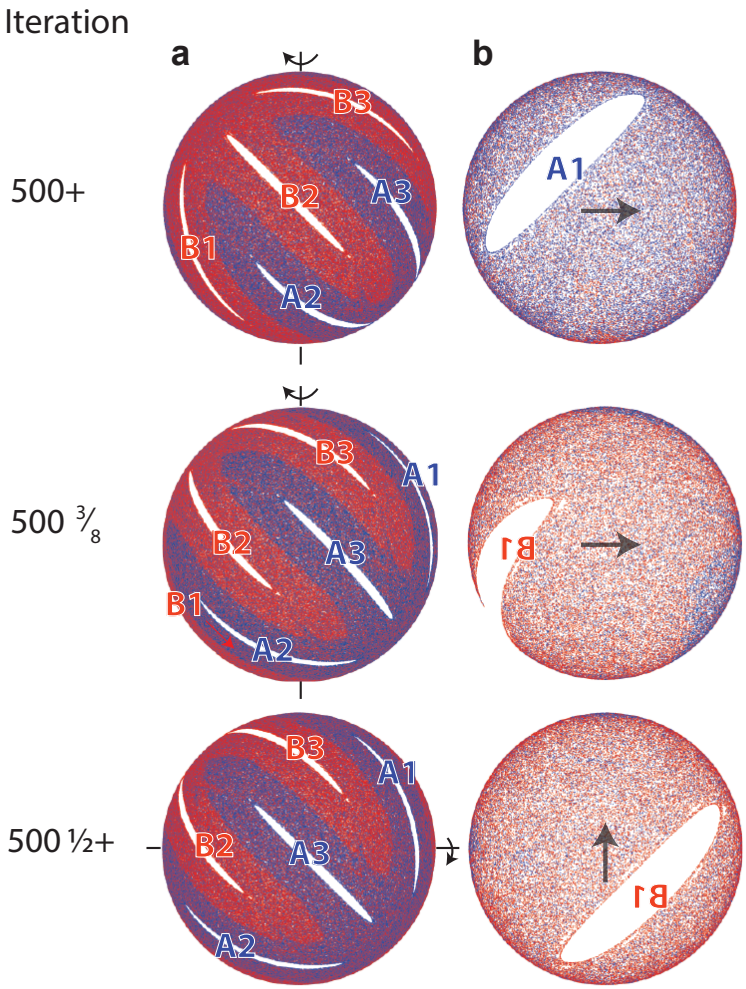

Figure 4.10. Movement of emergent non-mixing regions through the flowing layer. Emergent non-mixing regions (A1-A3, B1-B3) appear only for $\epsilon > 0$ (i.e., non-existent in the PWI model) and their accompanying 'fingers' alternate between being fully contained in the flowing layer or in the bulk after each half-iteration for the $(45^o, 45^o)$ protocol. Views from below of the hemispherical shell (a) and the planar flowing layer (b) for $\epsilon = 0.15$. Labels of periodic regions illustrate changes in orientation. Animations are provided in Supplementary Movie 2. Arrows in (b) indicate the direction of flow in the flowing layer.

4.3. Discussion

Cutting-and-shuffling offers an expanded new framework from which to consider mixing, and of which we have only begun to investigate. Based on this study of mixing in a model system consisting of a spherical tumbler under a biaxial mixing protocol, we show that the

mathematics of piecewise isometries (the PWI model) can accurately predict the mixing and non-mixing regions observed in experiments when the flowing layer depth is sufficiently small. While the mathematical limit of cutting-and-shuffling represented by the PWI model provides a skeleton of the structure of solid-like mixing, fluid-like stretching in the flowing layer modifies the structure. The continuum FL model connects the idealized non-mixing regions evident in the PWI model with the modified non-mixing regions observed in experiments, though without collisional diffusion. In our model system, a deeper flowing layer increases the fraction of particles in the flowing layer and the time they spend there, which then increases the influence of mixing via stretching-and-folding. We expect other 3D dynamical systems with coexisting solid and fluid regions (which include many practical mixing devices such as bladed mixers and plows in addition to tumblers) to exhibit similar complex mixing structures that result from the distinct and competing mixing processes associated with fluid stretching-and-folding and solid cutting-and-shuffling [149]. A deeper understanding of these 'hybrid-mixing' systems based on the structures determined by piecewise isometry theory is expected when the spatial extent of flowing regions is limited or when the flows are weakly shearing.

Finally, the cutting-and-shuffling paradigm for mixing lies at the intersection between the abstract mathematical theory of piecewise isometries and dynamical systems approaches to mixing. While we have shown that non-mixing regions occur under certain conditions, it may be possible to improve both the degree of mixing and the rate of mixing by varying the cut-and-shuffle parameters at each iteration using optimal control strategies to develop 'time-dependent' cut-and-shuffle mixing strategies. Of course, compared to smooth dynamical systems, cutting-and-shuffling uses discrete time steps and generates complex, multi-modal, discontinuous distributions of mixing metrics across the parameter space, all of which present new challenges in optimal control. Furthermore, the cuts can occur anywhere, so the combinatoric methods used to study discrete space shuffling do not necessarily

apply. Nevertheless, combined cutting-and-shuffling and stretching-and-folding strategies offer the potential to actively control the degree and rate of mixing, which may be significant in many physical systems.

CHAPTER 5

Pattern formation in a fully three-dimensional segregating granular flow

SUMMARY

Complex mixing behaviors have been demonstrated for a tracer particle in the BST system for protocols with coexisting flowing and static regions. In this chapter, tumbling a size-bidisperse mixture in the same setup provides insight into the interaction between segregation and mixing dynamics. Experiments show robust segregation patterns over a range of particle sizes and volume ratios. Large particles preferentially accumulate in non-mixing regions while small particles cover the chaotic region. Reconstruction of the 3D locations of large particles using x-ray based particle tracking suggests accumulation of large particles near the tumbler wall, consistent with radial segregation in tumbler flows. The formation of the segregation pattern is hypothesized to be dependent on axial transport of particles in the flowing layer coupled with radial segregation. The protocol-dependent structure of the unstable manifolds of the flow surrounding the non-mixing islands provides further insight into why certain segregation patterns are more robust than others.

This chapter is adapted from "Pattern formation in a fully three-dimensional segregating granular flow" by Mengqi Yu, Paul B. Umbanhowar, Julio M. Ottino, and Richard M. Lueptow, *Phys. Rev. E* **99**, 062905 (2019)

5.1. Introduction

Segregation of flowing granular materials, differing in properties such as density or size, has been studied both experimentally and theoretically in a number of canonical geometries

including chutes [135, 33], quasi-two-dimensional (2D) bounded heaps [40], and annular shear cells [55], where the underlying flow field is relatively simple and develops easily predicted segregation patterns. However, the situation can be more complex when the chaotic dynamics of the underlying flow field interacts with segregation, as can occur in quasi-2D tumblers [67, 83, 44, 100, 101]. Although chaotic flows have been well studied in fluids [60, 113], similar studies with granular systems are few, particularly for three-dimensional (3D) systems.

As an example of the interaction between segregation and chaotic dynamics, consider the case of a quasi-2D tumbler with square cross-section rotated at a constant speed [100], where non-trivial segregation pattern forms due to the competing influences of segregation and the underlying flow. Here, the tumbler is initially half-filled with a uniform mixture of small (diameter $d_S = 0.3$ mm) black glass particles and large ($d_L = 1.2$ mm) clear glass particles. The tumbler is rotated at constant angular speed ($\omega = 1.44$ rpm) so that particles

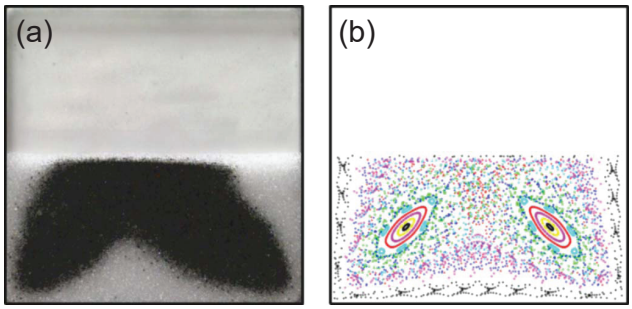

Figure 5.1. (a) Segregation experiment in a half-full square tumbler with 40% small (0.3 mm) black particles and 60% large (1.2 mm) clear particles by weight. Steady-state pattern after ten clockwise revolutions of the tumbler at 1.44 rpm. (b) Poincaré section of a half-full square tumbler derived from model of flow kinematics. Reprinted with permission from Meier et al. [100]

continuously flow down the free surface (rolling/cascading regime [102, 62]). After several revolutions, shown in Fig. 5.1(a), the small black particles accumulate in the two lobes, which extend from the core toward the two corners, while large clear particles occupy the periphery of the tumbler.

The lobed pattern comes from the time-periodic nature of the flow due to the tumbler geometry. That is, the surface flowing layer varies in length periodically from the position

shown in Fig. 5.1(a) to a position where it spans the diagonal of the tumbler. The corresponding Poincaré section, a stroboscopic mapping [152] of points advected by a simple kinematic model of the granular tumbler flow, is shown in Fig. 5.1(b). The Poincaré section captures the time-periodic nature of the flow by recording the positions of points after each period (one quarter revolution). Some points in the Poincaré section are trapped in islands on the diagonals (closed loops), while others are advected throughout the domain [100]. The key point here is that the Poincaré section is based on a continuum model derived purely from the velocity field, without any information concerning the particles used in the experiments or their tendency to segregate. Nevertheless, the correspondence between the two non-mixing elliptic islands along the diagonals (evident as colored ellipses and associated lobes) in the Poincaré section and the lobes of small black particles in the experiment is clear. The segregation pattern is a manifestation of the interplay between segregation of particles in the flowing layer and the dynamics of the time-periodic flow in the tumbler. Segregation drives small particles to percolate to the bottom of the flowing layer where they are influenced by the advection of the underlying flow field to accumulate in the non-mixing elliptic islands [100]. Pattern formation in quasi-2D tumblers occurs in many different tumbler geometries (square, pentagonal, triangular, and elliptical) with a range of particle types, sizes, weight fractions (2.5% to 60%), tumbler fill fractions (50% to 75%), and rotation rates [100, 101]. In other situations, radial streaks of segregated particles as well as lobed patterns can be observed [66, 67, 64, 72, 44, 179, 100].

While the interaction between particle segregation in the quasi-2D square tumbler in Fig. 5.1(a) and the 2D chaotic dynamics of the associated Poincaré section based only on the kinematics of the flow is quite evident, it is not obvious if the same interaction will occur in a fully 3D system. Previous studies of granular flow in 3D tumblers focused on axial segregation in long rotating drums [176, 3, 22, 66] and spherical tumblers [45, 34, 21, 18]. It is only recently that chaotic dynamics in a spherical tumbler has been identified and a

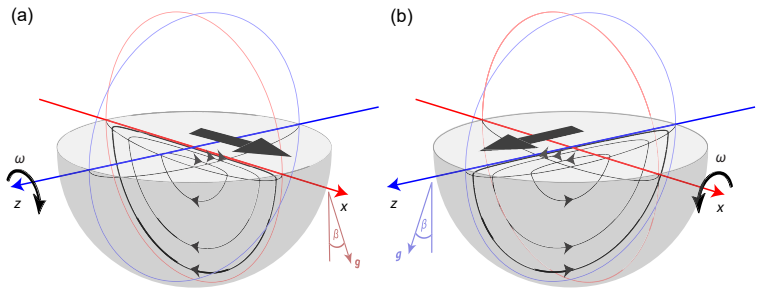

Figure 5.2. Biaxial spherical tumbler flow consists of two alternating single axis rotations about (a) the z-axis and (b) the x-axis, at a rotation speed ω. Material passing through the flowing layer (with a flat free surface at angle β to horizontal) is subsequently deposited downstream and then moves in solid-body rotation with the tumbler until it reenters the flowing layer. Reprinted with permission from Zaman et al. [173]

kinematic continuum model has been proposed [78, 101, 24]. In this chapter, we examine whether or not granular segregation and chaotic dynamics interact in a similar way in a 3D system so as to generate segregation patterns related to non-mixing regions.

To answer this question, we consider segregation patterns in a 3D spherical tumbler that is half-filled with a mixture of small and large millimeter-sized spherical particles. As shown schematically in Fig. 5.2, the tumbler is rotated by angle θ_z about the z-axis and then by angle θ_x about the x-axis, where the z-axis and x-axis both lie in the horizontal plane. In the figure and in most previous studies, the axes are orthogonal, but in general, the angle γ between them can have any value [77, 94]. This latter biaxial rotation protocol is specified by the triple $(\theta_z, \theta_x, \gamma)$ and typically is repeated many times. The segregation patterns described here depend on the specific protocol angles, mixture compositions, and particle sizes. There are other factors that can influence the segregation patterns such as particle density and tumbler wall smoothness, but they are beyond the scope of this study. Christov et al. [24] identified chaotic mixing regions coexisting with regular non-mixing islands based on a continuum model calculation of the underlying flow for certain protocols. An example of the coexisting chaotic region and non-mixing islands in the Poincaré section is shown in the bottom view of the system in Fig. 5.3(a), where the white elliptical regions (labeled A1-A3

and B1-B3) are non-mixing islands surrounded by the chaotic region covered in blue and red tracer points. This Poincaré section is calculated from the continuum model outlined in Christov et al. [24] by tracing points initially seeded on the interface between the bulk and the flowing layer [see Appendices C and D]. The red and blue colors in the continuum model indicate tracer points for the z-axis and x-axis rotations, respectively.

More recently, Zaman et al. [173] experimentally demonstrated that elliptic non-mixing islands in the flow of monodisperse particles serve as barriers to mixing by prohibiting material exchange across their boundaries. Specifically, they showed that a single tracer particle can stay within the non-mixing regions near the tumbler wall, periodically appearing in each of the period-3 non-mixing regions (either A1-A2-A3 or B1-B2-B3), over hundreds of iterations of the protocol in a spherical tumbler rotated about two orthogonal axes. Occasionally, the tracer particle wanders into the chaotic region due to collisional diffusion, but it eventually returns to the non-mixing regions where it can again remain hundreds more iterations. These non-mixing regions also can be predicted by the more abstract mathematical theory of piecewise isometries (PWI) [50, 51], where discontinuities can generate complex dynamical behaviors as seen in various applications [153, 31]. The PWI map, which applies to the limiting case of an infinitely thin flowing layer at the free surface [78, 122, 145], captures the skeleton of the underlying flow generated by the fundamental framework of cutting-and-shuffling, a mechanism for mixing discrete materials [78, 26, 77, 94, 170, 173].

In this chapter, we replace the monodisperse bed particles and single large tracer particle used in our previous work [173] with mixtures of small and large particles to explore if segregation patterns in a fully 3D system match the predictions of the Poincaré section derived from the flow kinematics alone. This would be analogous to the quasi-2D segregation pattern in Fig. 5.1(a) matching the 2D Poincaré section in Fig. 5.1(b). Apart from the fundamental question of whether 3D chaotic dynamics interact with granular segregation, this research has implications for practical devices for mixing granular materials in which

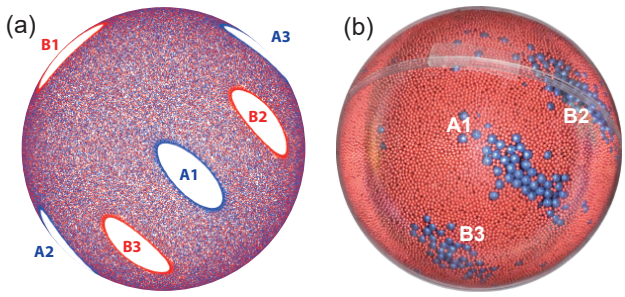

Figure 5.3. (a) Bottom view of the Poincaré section of a half-full spherical tumbler for $r = 0.95$ with protocol $(57°, 57°, 90°)$. (b) Bottom view of a segregation experiment in a half-full spherical tumbler with 15% large ($d_L = 4$ mm) blue particles and 85% small ($d_S = 1.5$ mm) red particles by volume with 30 iterations of the same protocol as in (a). Red and blue colors in experiments and in the continuum model are unrelated.

non-mixing (segregation) regions are detrimental to the mixing process, a critical issue in mixing powders in the pharmaceutical and chemical industries.

The answer to the question of whether or not granular segregation and chaotic dynamics can interact in a 3D system to generate segregation pattern is immediately evident from the bottom view of an experiment with a mixture of initially mixed large blue particles ($d = 4$ mm) and small red particles ($d = 1.5$ mm) for protocol $(57°, 57°, 90°)$, shown in Fig. 5.3(b), taken after 30 iterations. Large blue particles accumulate in the period-3 non-mixing regions at the bottom center of the tumbler, corresponding to A1, B2, and B3 islands in the Poincaré section in Fig. 5.3(a). The red and blue colors in the continuum model indicate tracer points for the z-axis and x-axis rotations, respectively. In the next section we will show that large blue particles also accumulate in the non-mixing regions labeled as A2, A3, and B1 on the periphery of the tumbler, which is not visible in Fig. 5.3(b) due to curvature of the tumbler surface.

Thus, it appears that the same mechanism that leads to pattern formation in the quasi-2D system of Fig. 5.1 also occurs in a fully 3D system. That is, segregation due to particle size difference effectively drives one particle species into the non-mixing features derived from dynamical system models. In the remainder of this dissertation we explore pattern

formation in the 3D spherical tumbler, its relation to chaotic dynamics, and the details of the mechanisms that are involved.

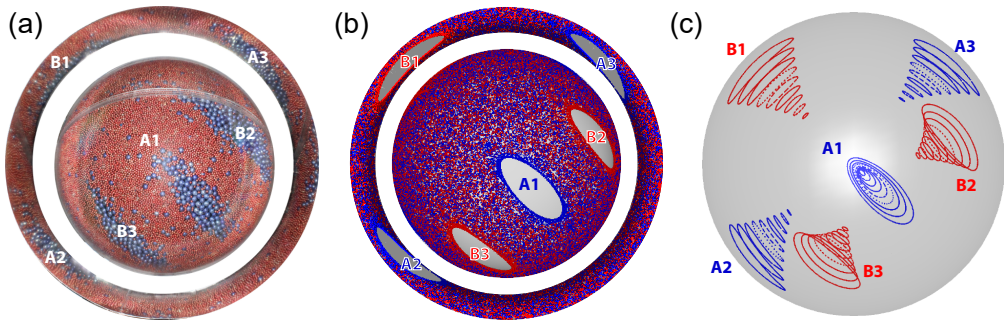

Figure 5.4. (a) Segregation experiment in a half-full spherical tumbler rotated at 2.6 rpm with 10% large blue particles (3 mm) and 90% small red particles (1 mm) by volume showing six distinct large particle islands after 30 iterations of protocol $(57°, 57°, 90°)$. The outer ring is the tumbler reflection in the surrounding cylinder, which shows the periphery of the tumbler. (b) POV-Ray [1] generated view of Poincaré section including a reflective cylinder. Flowing layer edges are tracked for 500 iterations near the tumbler wall at nondimensional radius $r = 0.95$. (c) Bottom view of 3D non-mixing islands from continuum model for $0.55 < r < 0.95$ in increments of 0.05 consist of a pair of period-3 islands for a total of six conical-shaped non-mixing structures (A1-A2-A3 and B1-B2-B3).

5.2. Segregation pattern visualization

Experiments are conducted using the same apparatus and methodology described previously [173]. An acrylic spherical tumbler of diameter $D = 2R_o = 14\,\text{cm}$ half-filled with millimeter-sized spherical glass particles is placed on an apparatus consisting of a set of three rollers mounted on a turntable. The spherical tumbler rests on the rollers, one of which is driven by a motor to rotate the tumbler about a single horizontal axis at 2.6 rpm. To rotate the tumbler about a different axis, a mechanism lifts the tumbler off the rollers, the turntable is rotated, and the tumbler is set back down on the re-oriented rollers. In this way, the tumbler can be repeatedly rotated about two horizontal axes in an alternating fashion to perform a biaxial rotation protocol. In previous work [173], only a single large tracer particle

was tracked. Here, we use a large number of larger diameter particles so that segregation patterns can form.

To qualitatively analyze the segregation pattern, we photograph the tumbler from below. After a desired number of biaxial rotations, the tumbler is removed from the apparatus, placed in a hole in a metal plate having a diameter slightly smaller than that of the tumbler, and photographed from below. Due to the curvature of the spherical tumbler, only the lower portion of the hemisphere is clearly captured in the photo [center circular image in Fig. 5.4(a)]. To view the periphery of the tumbler, a polished circular aluminum cylinder (15.2 cm diameter by 7.6 cm long) is attached to the bottom of the plate concentric with the tumbler. In this way, the reflection of the periphery of the tumbler is also captured in the photo [ring in Fig. 5.4(a)]. The tumbler is illuminated by a point LED light source positioned just to the side of the camera lens. Two photos are taken with the light source on the left and right sides of the camera lens while maintaining the same camera location and settings. The final image is obtained by combining left and right halves of the two photos that do not have glare or shadows. The light-colored arc above the label B2 in Fig. 5.4(a) is the seam between the two halves of the clear spherical tumbler.

Figure 5.4(a) shows pattern formation for the protocol $(57°, 57°, 90°)$. Here, large blue particles accumulate in non-mixing regions surrounded by small red particles. There are six clusters of large blue particles, three in the center circle (A1, B2, and B3) and three reflected in the ring (A2, A3, and B1). These clusters align closely with the six non-mixing islands evident in the Poincaré section in Fig. 5.4(b), which is constructed according to the process outlined in Appendices C and D. The tumbler and the reflected ring in the Poincaré section are constructed using POV-Ray [1] in the same manner the tumbler is photographed in Fig. 5.4(a).

The similarity between the segregation pattern of clusters of large particles in Fig. 5.4(a) and the elliptic (non-mixing) regions in the Poincaré section in Fig. 5.4(b) is a key result of

this dissertation. That is, the Poincaré section, which is based only on a simple kinematic model of the velocity in the flowing surface layer in the tumbler and has no particle segregation model at all, predicts the regions in which segregating particles (large particles in this case) accumulate. Thus, the chaotic dynamics of the system, as represented by the Poincaré section, predicts the segregation pattern for the experimental conditions.

Unlike the quasi-2D systems shown in Fig. 5.1, Poincaré sections in a fully 3D systems are also three dimensional. Figures 5.3 and 5.4 only show the segregation pattern visible at the clear wall of the spherical tumbler and the corresponding Poincaré section at a dimensionless radius of $r = 0.95$ (just adjacent to the wall of the tumbler). These 2D non-mixing islands on different invariant surfaces form a 3D structure around a line of periodic points [107, 101, 130, 105, 24]. To visualize the 3D structure in the spherical tumbler flow, trajectories of the points on the boundaries of non-mixing islands for the (57°, 57°, 90°) protocol in the radius range of $0.55 < r < 0.95$ are isolated and assembled in Fig. 5.4(c) to form six cone-like Kolmogorov-Arnold-Moser (KAM) tubes [130, 24], analogous to 2D KAM islands. The shape of the 3D KAM structure is determined by the protocol. The 3D KAM structures shown here for the $(57°, 57°, 90°)$ protocol are conical with their apex pointing toward the center of the hemisphere. The bases of the cone-like KAM tubes are at the wall of the tumbler and correspond to the islands A1-A3 and B1-B3 in which the large particles accumulate in Fig. 5.4(a). Viewing the hemisphere from the bottom as in Fig. 5.4(c), the A2, A3, and B1 KAM tubes are viewed from the side making their conical shape obvious, while the A1 KAM tube is viewed from its base [leading to the nested ellipses in Fig. 5.4(c)]. KAM tubes B2 and B3 are between these extremes of orientation. The largest ellipse in each of the six KAM tubes, which is the portion of the KAM tubes closest to the wall of the tumbler, corresponds to the elliptical non-mixing regions in Figs. 5.4(a) and 5.4(b).

In Fig. 5.4(a), the mixture consists of 10% large (3 mm) blue particles and 90% small (1 mm) red particles. The large blue particles accumulate into regions that correspond to

color	red				blue	
nominal size (mm)	1	1.5	2	3	2	4
actual size (mm)	1.12 ± 0.09	1.50 ± 0.13	1.90 ± 0.09	3.15 ± 0.14	2.03 ± 0.12	3.99 ± 0.04

Table 5.1. Nominal particle sizes and corresponding actual particle sizes.

non-mixing islands predicted by the continuum model. To fully characterize the pattern formation, experiments are carried out across a range of particle size ratios R and large particle volume fractions f. Figure 5.5 shows experimental results for mixtures of equal-density spherical glass particles with actual particle size ratios 3.56, 2.67, 2.1, 1.27, and 1.69. Nominal and actual particle diameters of the mixtures used in the experiments are listed in Table 5.1. The volume fraction of large particles is 5%, 15%, and 25%. In the first four columns of Fig. 5.5, the large particle size is kept constant at 4 mm to allow a direct visual comparison of the coverage of large particles on the tumbler wall. The rightmost column with $R = 1.69$ and a large particle diameter of $d = 2$ mm provides a comparison to size ratio $R = 2.1$ images with large particle diameter of $d = 4$ mm to assess the effect of the tumbler size relative to particle sizes.

Consider the first row of experiments with $f = 5\%$. The three clusters of blue particles match with non-mixing islands A1, B2, and B3 predicted by the Poincaré section calculated from the continuum model in Fig. 5.4(b). The boundaries of the regions of blue particles become more difficult to discern as the particle size ratio decreases, particularly for $R = 1.27$. This result is expected since a smaller size ratio reduces segregation. Consequently, particles have a greater tendency to remain in a mixed state, resulting in less distinct segregation with a smaller size ratio. It is also evident that the islands of large blue particles are smaller for larger size ratios. This is likely a result of the relatively small fraction of large particles and the large particle size ratio, which allows small particles to populate regions at the wall below the large particles.

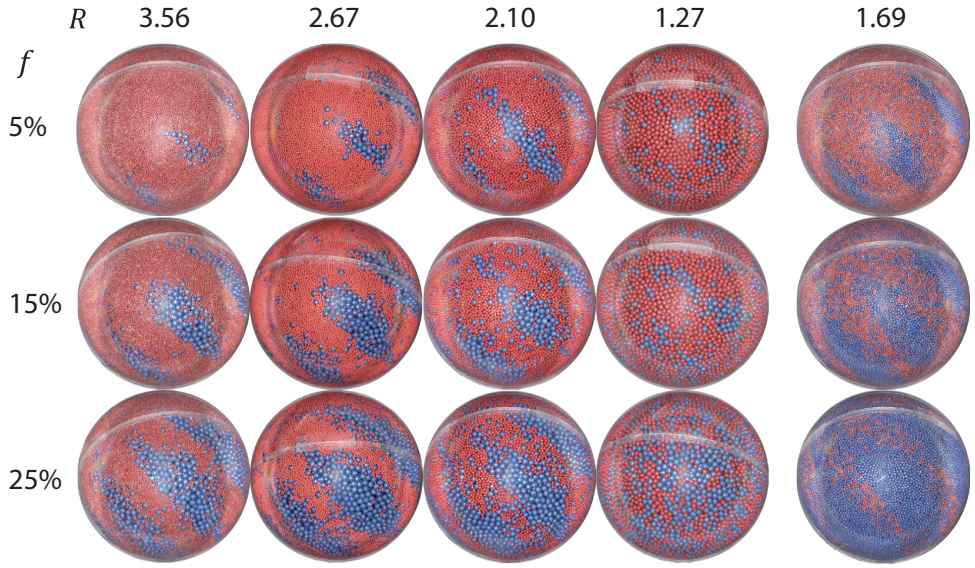

Figure 5.5. Segregation experiments in a half-full spherical tumbler after 30 iterations of protocol $(57°, 57°, 90°)$ rotated at 2.6 rpm for a range of mixtures: 5%, 15%, and 25% volume fraction f of large blue particles with small red particles, for size ratios $R = 3.56$, 2.67, 2.1, 1.27, 1.69. All columns use 4 mm diameter large particles except for the rightmost column where the large particle diameter is 2 mm.

As the volume fraction of large particles increases (rows two and three in Fig. 5.5), the same segregation pattern persists. For all size ratios, the clusters of large particles occupy larger area as f increases from 5% to 25%, growing in both length and width, because more large particles are available to accumulate in the non-mixing regions. In general, accumulation of large particles into the non-mixing regions is more distinct with a larger size ratio, while collisional diffusion and segregation make the patterns less evident with decreasing size ratio so that for a size ratio of $R = 1.27$ and $f = 25\%$ the segregation pattern is no longer evident.

For the four size ratios on the left in Fig. 5.5, the large particle diameter remains constant at 4 mm while the small particle size varies. Consider now the size ratio $R = 1.69$ in Fig. 5.5, where the large particle size is now 2 mm instead of 4 mm. The accumulation of large blue particles into three non-mixing regions is still observed across the different large particle volume fractions. At $f = 25\%$, compared with a similar size ratio $R = 2.1$, the coverage

of large blue particles is much higher with fewer small red particles visible. Yet, it is still obvious that large blue particles accumulate more intensely in the non-mixing regions.

The series of experiments in Fig. 5.5 demonstrates that the segregation pattern for this particular protocol $(57°, 57°, 90°)$ is quite robust and manifests itself across a wide range of particle size ratios and large particle volume fractions, despite the interplay between collisional diffusion and segregation due to particle size difference. The segregation pattern becomes clear after about 15-20 iterations and remains obvious with more iterations (see Fig. F.1 in Appendix F for experiments at 20, 40, and 50 iterations). The protocol $(57°, 57°, 90°)$ exhibits robust and repeatable patterns with every run (see Fig. F.2 in Appendix F for repeated experiments). The period-3 non-mixing structures in protocol $(57°, 57°, 90°)$ segregation pattern are not unique. More generally, similar period-3 segregation patterns also develop after 15 to 20 iterations for a range of rotation angles $(54° - 60°)$ about both axes (see Fig. F.3 in Appendix F for segregation experiments of protocol $(54°, 54°, 90°)$ and $(60°, 60°, 90°)$ and a comparison to corresponding Poincaré sections).

Collisional diffusion tends to disperse particles throughout the domain, as is evident from weaker segregation at smaller R. In previous work on spherical tumbler flow, chaotic advection also drives particles across the entire domain with random paths [173]. Thus, we hypothesize that the segregation between large and small particles traps many large particles in the non-mixing regions resulting in the pattern formation. The details of the features depend on the relative strength of diffusion, segregation and chaotic advection, which is also observed in the structure variation (stratified, segregated, and mixed states) of bounded heap flows [39]. Other factors including rotation rates and fill fractions may also influence pattern formation in a quasi-2D tumbler [100, 67], and are likely to do so in a spherical tumbler.

5.3. Non-mixing structures in 3D

Visualization of the segregation patterns formed at the tumbler wall in the previous section is an intuitive way to qualitatively analyze the pattern formation, but only near the tumbler wall. As shown in Fig. 5.4(c), the non-mixing structures predicted by the Poincaré section are cone-like in three dimensions. Hence, x-ray imaging is employed to examine the 3D nature of particle segregation.

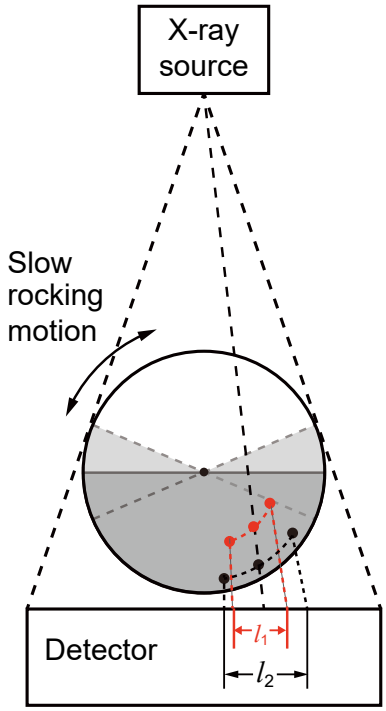

Figure 5.6. Schematic of depth determination. Cone-shaped x-ray beam passes through the tumbler and x-ray images are captured by a detector below the tumbler. Rotating the tumbler between the two extremes defined by the repose angle results in trajectories l_1 and l_2 at the detector that depend on the radial location of the particle in the tumbler.

The x-ray imaging equipment used in this study is the same as used previously [173]. X-ray images of the tumbler are captured by a detector located below the tumbler apparatus as shown in the schematic in Fig. 5.6. The 14 cm diameter tumbler appears as a circular image on the detector with a diameter of 612 pixels. The image is calibrated to remove warping effects in image detection due to the image intensifier and camera optics [173]. The

tracer particle used in this study is about 3 mm in diameter, which is about 13 pixels in the image. The cone-shaped x-ray beam makes it possible to obtain the 3D positions of multiple tracer particles as follows. When the tumbler is slowly rotated to the granular material's angle of repose and back, all particles move in solid body rotation. A sequence of images are taken at one frame per angle of rotation to record the positions of all tracer particles. Then, the 3D trajectories of tracer particles can be tracked. These trajectories project onto the detector image at different trajectory lengths depending on the particle depth, as shown in the schematic side view in Fig. 5.6. For example, the black particle that is closer to the tumbler wall has a longer projected trajectory (l_2) than that of the red particle (l_1), which is located further radially inward. However, the tracer particle positions are projection-distorted because the x-rays that strike the flat detector traverse different distances depending on the depth of the particle and how far it lies from the source-detector central axis. The 3D position of a tracer particle can be calculated iteratively from the sequence of 2D images during the slow rotation where all particles move in solid body rotation (a rocking motion). Based on the tracer particle coordinates in the images, an approximate radial location of the particle in the tumbler can be determined. With the estimated radius, coordinates of the trajectory are adjusted accordingly, and a new value of the radius can be calculated. This process is repeated until the difference in radius between successive iterations is less than 1%. With multiple tracer particles, a particle tracking velocimetry (PTV) algorithm in MATLAB is used to detect and trace particle trajectories [29]. To ensure accurate tracking, only trajectories longer than 65% of the sequence length are used, which also reduces error due to particles overlapping. In this way, the 3D position of many x-ray opaque tracer particles is obtained after each rotation of the protocol.

The apparatus and analysis methods have some limitations. Tracking the trajectories of tracer particles requires accurate detection of the particles in the x-ray image. With a large number of tracer particles, particles often overlap in the x-ray image. Particles at different

depths may be projected to the same neighborhood on the detector image, particularly as particles accumulate into a non-mixing region and overlap. At the same time, when the tumbler is rotated to the angle of repose, the relative particle locations change, so that particles may cross over each other or overlap in the images. Thus, it is challenging to track a large number of particles. To avoid inaccurate detection of particles, experiments are limited to fewer than 200 x-ray opaque tracer particles. With 3 mm particles, this comprises less than 1% of the total particle volume. Thus, for experiments with volume fractions of large particles higher than 1%, both large x-ray opaque tracer particles and large glass beads of similar density are used to provide the appropriate volume of large particles. Nevertheless, the tracer particles still represent the ensemble behavior of all large particles.

The continuum model for the $(57°, 57°, 90°)$ protocol predicts cone-like non-mixing structures, each with its base on the wall of the spherical tumbler and its apex pointing toward the center of the tumbler [Fig. 5.4(c)]. The cone-like non-mixing structure narrows to the size of a typical large particle at a dimensionless radius of about $r = 0.55$. If the particle is larger than the KAM tube, a single particle in a non-mixing region cannot be distinguished from particles dispersed randomly in the chaotic region. Therefore, non-mixing structures in the experiment should only occur for locations in the tumbler where $r > 0.55$. We use this result to explore how particles segregate and patterns form in the tumbler. Two experiments tracking x-ray opaque tracer particles are performed, first targeting particles that start near the center of the bed that should segregate to near the tumbler wall and accumulate in non-mixing regions, and second, targeting particles that start near the tumbler wall that should segregate toward the center of the tumbler where the cone-like non-mixing regions do not extend.

In the first experiment, 400 $d = 3.01 \pm 0.04$ mm, $\rho = 2.5 \pm 0.05\,\mathrm{g\ cm^{-3}}$ hollow silver jewelry beads (Beadcorp) with 0.9 mm holes are used as x-ray tracer particles with $d = 1.84 \pm 0.07$ mm $\rho = 2.45 \pm 0.3\,\mathrm{g\,cm^{-3}}$ glass particles in the bulk. The tracer particles are

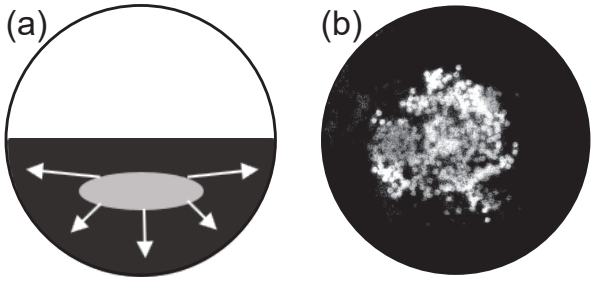

Figure 5.7. Initial condition for tracking particles segregating toward the tumbler wall. Large x-ray opaque 3 mm silver particles (gray region) are seeded in the core of the hemispherical bed of 1.8 mm glass particles (black background) as shown in (a) a side view schematic with arrows indicating that these particles are expected to segregate toward the tumbler wall and (b) a bottom-view x-ray image.

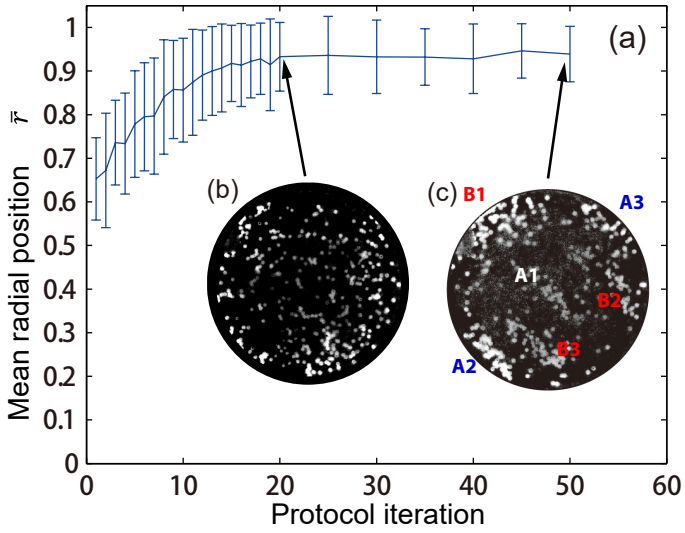

Figure 5.8. (a) Mean normalized radius $\bar{r}$ of large x-ray opaque tracer particles vs. protocol iterations for protocol $(57°, 57°, 90°)$. X-ray images of tracer particles at (b) 20 iterations and (c) 50 iterations. Particles have segregated to near the tumbler wall after 20 iterations, but only at 50 iterations are the tracer particles segregated into non-mixing islands labeled by A1-A2-A3 and B1-B2-B3. Error bars are $+/-$ one standard deviation.

seeded in the core of the tumbler [Fig. 5.7(a)], appearing as a circular cluster in the bottom-view x-ray image [Fig. 5.7(b)]. Thus, the initial blob of large x-ray opaque tracer particles starts at a radial location near the apices of the conical non-mixing structures. Once the rotation protocol starts, the large x-ray opaque particles should migrate to near the wall of the

tumbler due to segregation in the flowing layer, recalling that larger particles preferentially segregate to the surface of the flowing layer and thereby to the periphery of the bed of particles [110]. The question is: Do the large particles accumulate in non-mixing regions before or after they get near the tumbler wall?

To answer this question, in this experiment, after each iteration, the 3D positions of all tracer particles are obtained. The mean tumbler-radius normalized radial position $\bar{r}$ of tracer particles in the tumbler is calculated to quantify the extent of the segregation. In Fig. 5.8(a), the mean normalized radius of tracer particles $\bar{r}$ is plotted against the number of iterations. The mean radius starts around 0.7, increases rapidly in the first 20 iterations, and then stays fairly constant at about 0.9. Thus, the tracer particles segregated to near the wall of the tumbler, as expected. At 20 iterations [Fig. 5.8(b)], tracer particles are dispersed randomly throughout the image but are near the tumbler wall based on Fig. 5.8(a). After 50 iterations [Fig. 5.8(c)], tracer particles form clusters in the non-mixing regions as predicted by the continuum model, labeled as A1-A2-A3 and B1-B2-B3. Note that the the intensity of Figure 5.8(c) is adjusted using adaptive histogram equalization in MATLAB (`adapthisteq`) [126, 177], where the contrast is enhanced in 64 smaller "tiles" across the entire image. The clusters form slowly, becoming more evident toward the end of the experiment. This result demonstrates that large particles accumulate in non-mixing regions consistent with the continuum model but only after they have first segregated to near the wall of the tumbler where the non-mixing regions have significant volume due to their conical shape.

In the second experiment we use a mixture of 400 $d = 3.01 \pm 0.04$ mm hollow silver jewelry beads ($\rho = 2.5 \pm 0.05\,\mathrm{g\,cm^{-3}}$) as tracers with $d = 1.92 \pm 0.04$ mm acrylic particles ($\rho = 1.24 \pm 0.08\,\mathrm{g\,cm^{-3}}$) in the bulk. This combination of size and density differences causes the silver particles to sink to the bottom of the flowing layer during tumbler rotation while the acrylic particles rise to the surface of the flowing layer so they segregate toward the tumbler wall. The silver particles are seeded at the bottom of the tumbler as shown in the

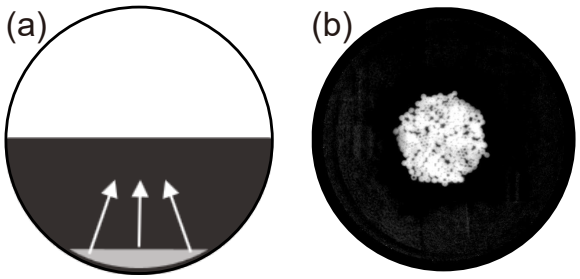

Figure 5.9. Large silver particles (3 mm) are seeded at the bottom of the hemispherical bed of 2 mm acrylic particles as shown in (a) the side view schematic with arrows indicating that these particles are expected to segregate toward the center of the particle bed and (b) a bottom-view x-ray image.

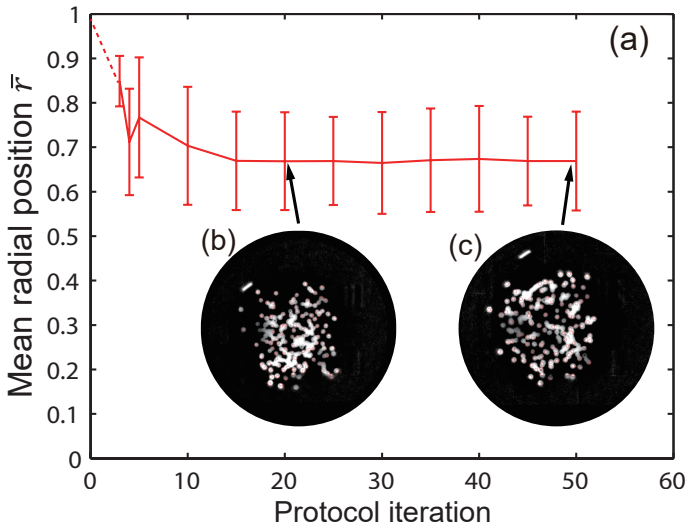

Figure 5.10. (a) Mean normalized radius $\bar{r}$ of x-ray opaque tracer particles vs. number of protocol iterations $(57°, 57°, 90°)$. X-ray image of tracer particles at (b) 20 iterations and at (c) 50 iterations. Error bars are +/- one standard deviation.

side view and bottom view in Figs. 5.9(a) and 5.9(b), respectively. Since silver particles sink to the bottom of the flowing layer, they are expected to segregate toward the core of the hemispherical bed of acrylic particles as the tumbler is rotated. The mean normalized radius of silver particles is plotted as a function of the number of protocol iterations in Fig. 5.10(a). Due to difficulties detecting the silver particles in the first few iterations, a dashed line is drawn to connect the initial condition (particles deposited at the tumbler wall) to subsequent iterations. The mean radius drops quickly to below 0.7 in the first 20 iterations and does

not vary significantly afterwards. The x-ray images at 20 iterations [Fig. 5.10(b)] and 50 iterations [Fig. 5.10(c)] both show x-ray opaque silver tracer particles in the middle portion of the tumbler, meaning that tracer particles relocate from near the tumbler wall to the core of the bed of particles. The dispersion of particles at 50 iterations is very similar to that at 20 iterations, and there is no apparent structure or accumulation of large particles other than near the core of the bed of particles. This result again matches the prediction of the continuum model [Fig. 5.4(c)], where no significant non-mixing structures exist near the core of the particle bed.

This pair of experiments demonstrates that particles form the segregation pattern predicted by the continuum model only close to the tumbler wall. The transport of particles can also be tracked as the volume fraction of large particles increases. Similar size and density glass beads ($d = 3.15$ mm; $\rho = 2.45\,\mathrm{g\,cm^{-3}}$) are used along with 200 silver tracer particles ($d = 3.01$ mm, $\rho = 2.5\,\mathrm{g\,cm^{-3}}$) to make total large particle volume fractions $f =$ 5%, 15%, and 25% mixtures with 1 mm small glass particles. Since the large glass beads and tracer particles have similar size and density, the behavior of tracer particles mirrors the bulk behavior of all large particles. The tracer particles are tracked for 50 iterations of the $(57°, 57°, 90°)$ protocol with large particles initially seeded in the center of particle bed. The mean normalized radius of tracer particles for all volume fractions decreases only slightly with increasing large particle volume fraction, at steady state (46 - 50 iterations), as shown in Table 5.2.

The results in Table 5.2 are consistent with the non-mixing regions expanding in size at the tumbler wall with increasing large particle volume fraction, as is evident in Fig. 5.5. However, the slight reduction in the mean normalized radius in Table 5.2 suggests not all large particles are in the monolayer at the wall. Based on approximating the coverage of a monolayer of large particles at the tumbler wall, we estimate that most large particles are within 3 particle diameters of the wall at the higher larger particle volume fractions.

f	5%	15%	25%
$\bar{r}$	0.9446	0.9358	0.9257
σ_r	0.0629	0.0575	0.0816

Table 5.2. Mean normalized radius $\bar{r}$ and standard deviation of normalized radius σ_r of tracer particles over 46 - 50 iterations of experiments with a mixture of 3 mm large silver tracer particles and glass particles and 1 mm small glass particles with large particle volume fractions $f = 5\%$, 15%, and 25%.

Thus, the large particles do not entirely occupy the conical non-mixing structures predicted by the continuum model in Fig. 5.4(c) but tend to expand the regions of large particles near the tumbler wall. This indicates that the mechanism of pattern formation is closely related to the segregation dynamics that occurs in the flowing layer. The effect of segregation may be so strong that large particles are pushed to the surface of the flowing layer so they never have a chance to fill the subsurface volume of the cone-like non-mixing structures. On the other hand, when segregation is weak, particles tend to mix more uniformly instead of accumulating in the non-mixing structures as occurs for $R = 1.27$ in Fig. 5.5.

5.4. Dependence on rotation protocols

Similarity between the pattern formation in experiments and non-mixing regions in the continuum model can be demonstrated in several other protocols, including those shown in Fig. 5.11: $(90°, 90°, 80°)$, $(90°, 90°, 90°)$, and $(75°, 60°, 90°)$. Large blue particles accumulate in two pairs of period-2 non-mixing islands labeled as A1-A2 and B1-B2 in Fig. 5.11(a) for protocol $(90°, 90°, 80°)$. Note that here the two rotation axes are not orthogonal, but at an angle of 80°. Similarly for the orthogonal axes case $(90°, 90°, 90°)$, large blue particles also accumulate into period-2 non-mixing islands despite more particles appearing in the chaotic region between the non-mixing islands. The period-2 non-mixing structures also occur in combinations of a range of rotation angles α and β with different angles between axes γ (see Fig. F.4 in Appendix F for experiments of protocols also exhibiting period-2 non-mixing structures). For the protocol $(75°, 60°, 90°)$ [Fig. 5.11(c)], where no non-mixing structures

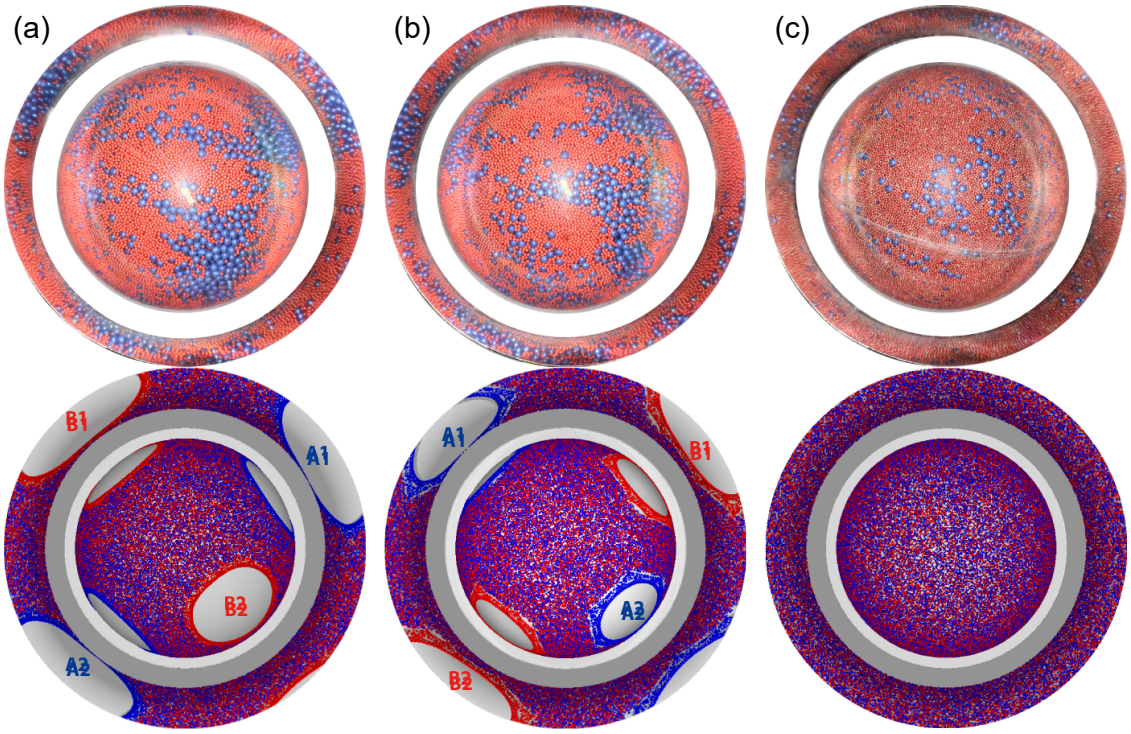

Figure 5.11. Experiments (top) compared to Poincaré sections (bottom) after 30 iterations of protocol $(90°, 90°, 80°)$ in (a) column, $(90°, 90°, 90°)$ in (b) column, and $(75°, 60°, 90°)$ in (c) column. Visualization of tumbler wall for corresponding experiments with 15% large blue particles (4 mm) and 85% small red particles (1 mm).

are predicted by the continuum model, the experiment shows no clear segregation patterns, as expected. Consequently, we speculate that other protocols that exhibit large non-mixing regions will show associated segregation regions in experiments.

The non-mixing islands for protocols $(57°, 57°, 90°)$, $(90°, 90°, 80°)$, and $(90°, 90°, 90°)$ are called persistent [173] in that they correspond to cells in PWI maps [145, 122], which provide a mathematical description of the action of cutting-and-shuffling that forms the foundation for non-mixing regions in spherical tumbler flow with alternating rotations about two axes [173]. Although PWI maps assume a non-physical infinitely thin flowing layer at the surface, the non-mixing structures they generate can persist for a finite-thickness flowing layer [173], as is evident in these experiments. The boundaries of the non-mixing islands are defined by the interface between the flowing layer and the bulk [173, 145].

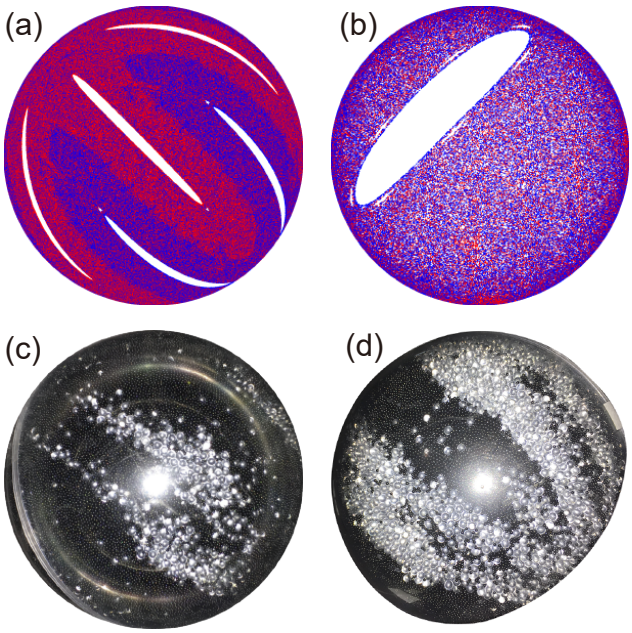

Figure 5.12. Poincaré section of the continuum model in (a) the bottom view of the bulk and (b) the bottom view of the flowing layer for protocol $(45°, 45°, 90°)$. Segregation patterns after 30 iterations in a half-full spherical tumbler with 10% large clear particles (3 mm) and 90% small black particles (1 mm) starting with (c) large particles in the bottom of tumbler (bottom view), and (d) large particles on top of the flowing layer.

In addition to the persistent non-mixing regions described thus far, there is another type of barrier to mixing known as an emergent non-mixing region [173], which are not present in the PWI map but emerge in the continuum model for a finite flowing layer thickness. Unlike persistent non-mixing regions that pass entirely through the flowing layer with each rotation and have boundaries set by the boundary of the flowing layer, emergent non-mixing regions periodically land entirely within the flowing layer, are stretched in the streamwise direction, and have boundaries that are not necessarily coincident with the flowing layer boundary [173]. For a detailed discussion of persistent and emergent non-mixing islands, see Zaman et al. [173]. An example of a Poincaré section exhibiting emergent non-mixing islands is shown in Fig. 5.12(a,b) for protocol $(45°, 45°, 90°)$. The Poincaré section consists of interpenetrating fingers that are primarily red or primarily blue when viewed from the bottom [Fig. 5.12(a)]. The boundaries between the red and blue regions are shown to be

barriers to mixing [173]. The stretching of one of the white non-mixing regions at the centers of the interpenetrating fingers is evident in Fig.5.12(b), which shows a non-mixing region as visualized from below as it lands entirely in the flowing layer between rotations.

To examine the influence of emergent non-mixing islands on segregation, experiments are conducted with the protocol $(45°, 45°, 90°)$ for a mixture of 10% large clear glass particles ($d = 2.97 \pm 0.05$ mm) with 90% small black glass particles ($d = 1.05 \pm 0.05$ mm) with two different initial conditions: large particles initially located in the bottom of the tumbler on the tumbler wall and large particles initially spread on top of the flowing layer. For the first experiment, large particles initially located at the bottom on the tumbler wall, accumulate into three pairs of thin strips, with the most visible pair in the middle [Fig. 5.12(c)]. This pattern corresponds to the red fingers in the continuum model [diagonal from left upper corner to lower right corner and on the left and upper periphery in Fig. 5.12(a)] with a thin non-mixing region in the middle of the fingers. The non-mixing region (white) in the middle of the diagonal finger [Fig. 5.12(a)] corresponds with the central small black particle filled region in Fig. 5.12(c). In the second experiment [Fig. 5.12(d)], large particles initially located in the flowing layer accumulate in the two visible blue fingers of the Poincaré map, again with the central non-mixing region (white) filled with small black particles [a third blue finger is stretched across the flowing layer, consistent with Fig. 5.12(b)]. This result is expected since the blue finger is mapped onto the flowing layer where large particles initially are located [Fig. 5.12(a)]. In both experiments, large particles do not occupy the white non-mixing regions predicted by the continuum model. Instead they accumulate in the colored finger like structures, demonstrating that the mixing barriers between the red and blue dominant regions in the continuum model are physical mixing barriers preventing material exchange [173]. Particles starting in one region are mostly confined in this region even with collisional diffusion. For all of the protocols in this section, the experiments demonstrate robust pattern formation matching features in the Poincaré sections derived from the continuum model.

5.5. Mechanism of pattern formation

5.5.1. Pattern formation in 3D versus quasi-2D

At first glance, segregation patterns in quasi-2D tumbler and 3D spherical tumbler appear similar. In the flowing layer, particles segregate due to differences in size, and at steady state one species accumulates in the predicted non-mixing islands while the other species occupies the rest of the domain. However, a major difference is that large particles occupy the chaotic region in a quasi-2D tumbler, while they accumulate in persistent non-mixing structures in a 3D spherical tumbler. Conversely, small particles accumulate in the non-mixing region in a quasi-2D tumbler, while they occupy the chaotic region in a 3D spherical tumbler.

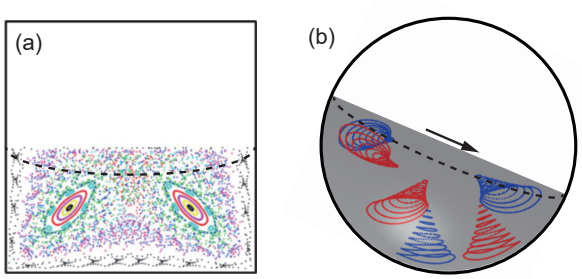

Figure 5.13. Schematic of the boundary of the flowing layer (dashed curve) superimposed onto the Poincaré section for (a) a half-full quasi-2D square tumbler and (b) a half-full 3D spherical tumbler.

To explain this difference, first note that segregation in the flowing layer occurs in the same manner in both quasi-2D and 3D spherical tumbler geometries. Small particles percolate down to the bottom of the flowing layer, while large particles rise to the top. The small particles deposit on the static bed of particles first, while the top layer of large particles continues to flow down the free surface. As a result, small particles are deposited near the middle of the flowing layer, while large particles are deposited further downstream. This deposition pattern is reinforced through periodicity due to the tumbler shape (2D) or due to the biaxial protocol (3D). The key point is that the bottom of the flowing layer consists mostly of small particles, which in the quasi-2D tumbler is where the non-mixing islands overlap the

flowing layer as shown schematically in Fig. 5.13(a). Consequently, small particles fall into the non-mixing islands when they segregate to the bottom of the flowing layer. Even if they segregate to the bottom of the flowing layer, where a non-mixing island is not present, they continue to be advected throughout the chaotic flow region (or via collisional diffusion), and eventually make their way into the non-mixing islands in subsequent rotations.

In contrast, the conical non-mixing structures in a 3D spherical tumbler have significant volume near the tumbler wall [Fig. 5.13(b)]. This means that the conical base of the non-mixing regions is located where large particles tend to segregate. As a result, the large particles tend to fill the non-mixing structures in the 3D spherical tumbler. Thus, how the particle segregation in the flowing layer coincides with the non-mixing islands determines which particles accumulate in non-mixing regions. That is, the interplay between underlying advection field and the particle segregation in the flowing layer determines the ultimate segregation pattern. Whether large particles or small particles accumulate in the non-mixing regions depends on the relative location of non-mixing regions when they pass through the flowing layer.

Another important point is that the accumulation of particles in non-mixing regions is made possible when the radial segregation is in the same plane as the mixing barriers. The segregation-driven material exchange across mixing barriers into the non-mixing regions inherently occurs in a single plane in a quasi-2D tumbler. However, the spherical tumbler is more complicated because of its 3D nature. Along with the radial transport, the large particles that accumulate into the non-mixing regions must also align with the non-mixing regions in the spanwise direction, requiring axial displacement of large particles.

In studies of single axis rotation of a spherical tumbler partially filled with size bidisperse mixtures, two different axial segregation patterns occur for a mixed initial condition depending on the fill fraction, absolute particle sizes, particle size ratio, volume fraction of large particles, and smoothness of the tumbler wall [109, 18, 45, 34]. Large particles either

accumulate in a band at the equator of the tumbler, or in two bands near the poles. For the operating conditions used in this study (rotation speed 2.6 rpm and half-filled tumbler), large particles tend to accumulate at the poles when the tumbler is continuously rotated about a single axis. This is shown in a top view of the free surface after 20 single-axis revolutions in Fig. 5.14. The large particles experience a small axial drift velocity that gradually drives them to concentrate in the bands near the poles, consistent with previous experimental results [18, 34].

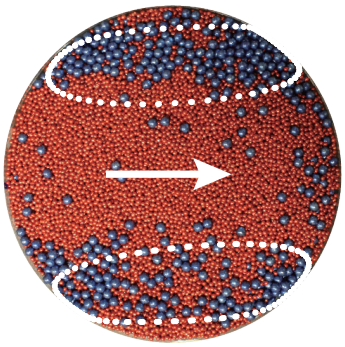

Figure 5.14. Top view of the flowing layer in a tumbler half-filled with 15% large blue particles (4 mm) and 85% small red particles (2 mm) after 20 revolutions about a single axis. White dotted curves represent boundaries of two non-mixing islands predicted by the continuum model for the protocol $(57°, 57°, 90°)$ as they would appear when flowing across the free surface. White arrow indicates the flow direction.

Non-mixing islands predicted by the continuum model for the biaxial (two-axis) rotation protocol as they pass through the flowing layer are shown by the white dotted boundaries overlaid on the single axis experiment result in Fig. 5.14. The axial positions of the non-mixing islands coincide with the regions of large particle accumulation for single axis rotation. Note that the bands formed for the single axis rotation experiment is a steady state result after 20 tumbler revolutions. In the biaxial experiments that we focus on in this dissertation, each single axis rotation action is smaller than 90°. Thus, the axial segregation is small for each iteration, yet the axial segregation is reinforced through repeated iterations. For each single axis action about either the z-axis or x-axis, the large particles segregate toward the

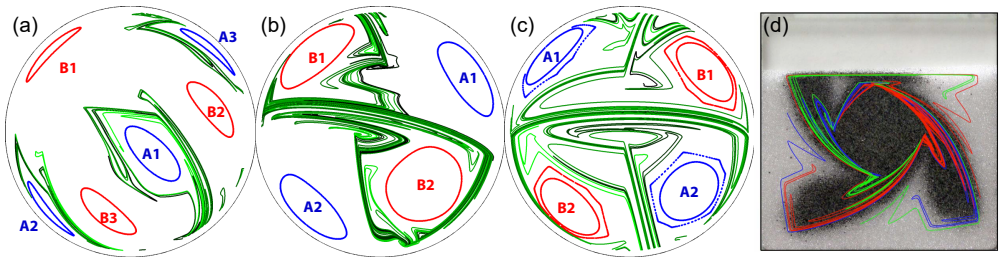

Figure 5.15. Unstable manifolds of period 3 in gradient color from black (dark) to green (light) for protocol (a) $(57°, 57°, 90°)$, (b)$(90°, 90°, 80°)$ in (b), and (c) $(90°, 90°, 90°)$. The blue and red closed curves (labeled as A1-A3 and B1-B3) are boundaries of non-mixing islands. Both the unstable manifolds and non-mixing islands are generated on the $r = 0.95$ surface. (d) Unstable manifolds superimposed onto experiment of a 75%-full quasi-2D tumbler with a mixture of 30% small black particles. Reprinted with permission from Meier et al. [100]

poles and accumulate in the coincident non-mixing islands. Segregation in both the radial and spanwise directions ensures that large particles move to the free surface and toward the poles where non-mixing structures have the largest volume. When this concentrating effect due to segregation is stronger than collisional diffusion, such as in the cases of large size ratios, the segregation pattern is clear and the features have distinct boundaries as shown for large size ratios in Fig. 5.5. Similar to radial segregation of small particles in the quasi-2D square tumbler, both radial and axial segregation aligns the large particles with non-mixing regions in the 3D spherical tumbler. Large particles are concentrated in these regions with repeated rotations. It is precisely the alignment of segregation with non-mixing regions that allows the large particles to accumulate in non-mixing regions.

5.5.2. A dynamical systems perspective

Experiments for protocols $(57°, 57°, 90°)$, $(90°, 90°, 80°)$, and $(90°, 90°, 90°)$ demonstrate robust pattern formation near the tumbler wall [see Figs. 5.4, 5.5, and 5.11(a-b)]. Particle accumulation for protocol $(57°, 57°, 90°)$ is the most compact and has the most well defined boundaries despite the fact that the non-mixing islands predicted by the continuum model are the smallest in size. On the other hand, the patterns for protocols $(90°, 90°, 80°)$ and

particularly protocol $(90°, 90°, 90°)$ have less clearly defined boundaries [Fig. 5.11(a-b)], even though the islands predicted by the continuum model are larger. This result occurs regardless of the large particle fraction, so it cannot be explained on that basis. To explore this contradiction, we examine flow behavior in the chaotic region immediately surrounding the non-mixing islands, neglecting effects of axial segregation and diffusion because they are small compared to the mean flow. The chaotic behaviors are induced by complex structures formed from stable and unstable manifolds, which correspond to contraction and expansion of material around a hyperbolic fixed point [113]. The algorithm used to compute the manifolds is described in Appendix D.

The unstable manifolds calculated from the continuum model for the portion of the tumbler visible from the bottom are shown with the non-mixing islands for protocols $(57°, 57°, 90°)$, $(90°, 90°, 80°)$, and $(90°, 90°, 90°)$ in Fig. 5.15 (a-c). There are two unstable manifolds for each of the three protocols, which correspond to the two sets of periodic points. For simplicity, only one of the two manifolds is shown in Fig. 5.15 (a-c). The separate portions of the manifold shown in each of the images are connected through the flowing layer, which is not shown. As the unstable manifolds stretch from the hyperbolic points, the color progresses from black (dark) to green (light). One unstable manifold of protocol $(57°, 57°, 90°)$ [Fig. 5.15(a)] wraps tightly around one group of the non-mixing islands (A1-A2-A3). Particles that happen to be bumped out of the non-mixing regions by collisional diffusion are advected by the unstable manifold. In subsequent iterations, the chance of the particle diffusing back into the non-mixing regions are high because the manifold wraps tightly around the A1-A2-A3 non-mixing regions. For protocol $(90°, 90°, 80°)$, even though the unstable manifold wraps around the non-mixing islands B1-B2 [Fig. 5.15(b)], the unstable manifold linkage between the two non-mixing islands occupies a larger portion of the domain, spanning the entire tumbler horizontally. Therefore, the accumulation of large particles for protocol $(90°, 90°, 80°)$ is less distinct [Fig. 5.11(a)] than for protocol $(57°, 57°, 90°)$ [Fig. 5.4(a)] because a particle

that starts outside of a non-mixing region or is bumped outside of the non-mixing region by collisional diffusion is more likely to be dispersed by the manifold to positions elsewhere in the chaotic region. For protocol $(90°, 90°, 90°)$ [Fig. 5.15(c)], the unstable manifold spans the entire domain and forms large folds that encompass all four non-mixing islands. Thus, particles are more likely to be dispersed to regions elsewhere in the chaotic sea once they are carried away by the manifolds, as is evident in the less distinctly segregated regions for the experiment of protocol $(90°, 90°, 90°)$ [Fig. 5.11(b)].

The relation between unstable manifolds and the segregation pattern is also evident in the quasi-2D tumbler. As shown in Fig. 5.15(d), the unstable manifolds surrounding the non-mixing islands outline the boundary of the segregation pattern. The unstable manifolds serve as a mixing barrier in that particles follow the manifolds instead of moving across them. This effect is observed in the 3D spherical tumbler for protocol $(57°, 57°, 90°)$. In contrast, for protocol $(90°, 90°, 90°)$, the unstable manifolds fill the entire domain, carrying particles throughout rather than acting as a barrier to mixing. As a result, the unstable manifolds in this case facilitate material transport throughout the domain, resulting in an indistinct segregation pattern [Fig. 5.11(b)].

5.6. Discussion and conclusions

We started this chapter by asking if granular segregation and chaotic dynamics can interact in a fully 3D system to generate segregation patterns, and the answer is clearly "yes" based on the visualization experiments alone. To further understand the relation between the segregation and chaotic dynamics, the segregation patterns of granular flows in a 3D spherical tumbler are examined with both surface visualization and x-ray imaging. Both methods demonstrate that particles of different sizes segregate into patterns predicted by a simple kinematic continuum model, at least for the protocols shown in this study and likely for many other protocols. The detailed characteristics of the segregation pattern depend

on the relative strengths of segregation, diffusion, and chaotic advection, as is evident from experiments with different particle size ratios, mixture fractions, and rotation protocols.

The pattern formation is a result of the coincidence between the non-mixing islands of the underlying flow field and particle segregation for both the quasi-2D square tumbler studied previously [100] and the 3D spherical tumbler examined here. When the direction of accumulation due to segregation aligns with non-mixing structures of the underlying flow field, segregation patterns form.

Other factors can influence the details of the pattern, including the strength of the segregation, collisional diffusion, and unstable manifold transport. These effects can be tuned to change the pattern to various degrees. For example, the relative strength of segregation compared to diffusion can be manipulated in several ways including changing rotation speed, particle to tumbler size ratio, and relative particle sizes. For instance, the pattern becomes weak when segregation is decreased with a smaller particle size ratio and thus a higher relative influence of collisional diffusion. It is also likely that when axial segregation is weaker, manifold driven transport becomes more important. The segregation pattern is perturbed more easily for protocol $(90°, 90°, 90°)$ than protocol $(57°, 57°, 90°)$, because the unstable manifolds are capable of carrying particles further away from the non-mixing regions. Hence, segregation pattern formation depends not only on the structure of dynamical systems features including elliptic non-mixing regions and unstable manifolds, but also on the relative strength of segregation compared to collisional diffusion. The relative strengths of these factors is key to predicting the pattern formation or to optimizing the mixing by avoiding such pattern formation.

It is also important to recognize that the parameter space for protocols is essentially infinite — rotation angles can vary continuously. We have described a handful of protocols in detail here, and we would expect similar results for protocols with rotation angles within a few degrees of those considered here in which similar non-mixing regions exist. We would also

expect similar results for other protocols with relatively large non-mixing regions, though it would be difficult to consider the complete set of non-mixing regions that may occur [122].

In generalizing the segregation pattern formation for other protocols, several factors must be considered. As mentioned earlier, the kinematic continuum model does not include any information about the particles, and axial transport is neglected. However, as shown in Chapter 5.5.1, axial segregation occurs for size-bidisperse particles in spherical tumbler flow (however small compared to bulk flow). Thus, the possibility of unpredicted pattern formation exists as a result of the additional axial transport that is not included in the present kinematic model. The final segregation pattern depends on a complex interplay between segregation, the flow field, and diffusion. We are also conducting discrete element method simulations to verify the mechanism with a statistical approach as well as examining secondary transport in the system.

Furthermore, the 3D flow in this study generates 2D invariant structures on hemispherical shells. Therefore, radial transport occurs only via diffusion and segregation. Fully 3D transport including radial transport can occur via streamline jumping [25, 24], which can be introduced to the experiments, for example, by rotating the tumbler about two axes at different speeds. Thus, 3D spherical tumbler flow can serve as a prototypical system for studying pattern formation and mixing in even more complicated 3D dynamical systems.

CHAPTER 6

Segregation to non-mixing regions driven by weak secondary flow

SUMMARY

The 3D structure of segregation patterns with large particle accumulation in non-mixing regions is analyzed with DEM simulations. Statistical analysis of particle movements in size-bidisperse cases and monodisperse cases demonstrates segregation patterns exist with low diffusion and large size ratios. DEM simulations also provide evidence that weak axial drift, inherent to a rotating spherical tumbler, transports particles across non-mixing barriers predicted by the unperturbed continuum model, which neglects axial transport. A modified continuum model incorporating this weak perturbation alters the periodic dynamics of non-mixing islands turning them into periodic "sinks." Through quantitative analysis of particle transport and comparisons of various size-bidisperse and monodisperse systems, the mechanism behind segregation pattern formation is identified as the interaction of size-driven radial segregation and surface flow dynamics.

This chapter is based on the manuscript "Segregation to non-mixing regions driven by weak secondary flow" by Mengqi Yu, Julio M. Ottino, Richard M. Lueptow, and Paul B. Umbanhowar to be submitted to *Phys. Rev. E*. The DEM simulations utilizing Nvidia GPU enabled computation based on CUDA C++ is adapted from code used in [137, 75].

6.1. Introduction

Segregation in flowing granular materials is prevalent in many industrial settings including pharmaceutical material blending, chemical material transportation, and construction material handling. In a typical mixing device, such as a tumbler, advection, segregation,

and collisional diffusion occur simultaneously. Advection in a tumbler can be generated by rotation about a horizontal axis that results in various flows including avalanching, rolling, and centrifuging, depending on rotation speed [62, 102]. Segregation between species with different physical properties is well studied, where granular materials demix under flow or shear [70, 35]. At the same time individual particles are continuously colliding with one another resulting in diffusion. Experiments and modeling methods have been developed to understand the interaction of these elements in various prototypical geometries. However, in tumblers where the advection field is complex and periodic, the interactions of advection, segregation, and diffusion are often not straightforward.

Many studies of tumbler flows have focused on quasi-2D geometries where the axial dimension is small compared to the radial dimension; this geometry results in an effectively two-dimensional velocity field. Segregation patterns in quasi-2D tumblers correspond to specific dynamics of the system. In a quasi-2D circular tumbler rotating with sufficient speed to avoid avalanching, particles flow continuously in a relatively thin layer near the flat free surface on top of a bed of particles in solid body rotation with the tumbler. When the particles are a size bidisperse mixture, segregation in the flowing layer leads to a radial segregation pattern where large particles migrate to the periphery of tumbler leaving a core of small particles at the center [17, 67, 72, 179, 58]. This process is well understood and can be modeled using a continuum description [138, 57, 159]. When the rotation speed is modified to be slow or modulated, the boundary between large particles on the periphery and the small particle core develops a multi-lobed structure [67, 83, 44]. Similarly, lobed patterns are observed in quasi-2D tumblers having a polygonal cross-section, due to the time-periodicity of the flow induced by the polygonal geometry, and are closely related to the unstable manifolds of the associated dynamical system [83, 100].

Though quasi-2D geometries have provided a useful avenue for study, tumblers used in industries are almost always 3D. In fact, for cylindrical tumblers with a substantial width relative to their radius, segregation can occur additionally along the axial dimensions, leading to a wealth of interesting phenomena including stable or unstable banding [176, 3, 22, 66, 128]; related banding is observed in spherical tumblers [45, 34, 109, 18, 21]. For rotation about a single horizontal axis, the advective flow is simple. Consequently, segregation patterns result from instabilities associated with spatially varying concentrations of the constituent species. Approaches to understanding these phenomena include analogies to spinodal decomposition [176, 22], and amplitude equation analysis [3].

However, in spherical tumblers rotated about multiple axes, the underlying flow can be chaotic [78, 101, 24]. This leads to new flow and segregation phenomena which can be understood using dynamical system approaches that have proven useful in fluid mixing [113]. Chaotic dynamics has been identified in a spherical tumbler to explain granular flow phenomena and a kinematic continuum model has been proposed [78, 101, 24, 173].

To study the complex interaction between advection, segregation, and diffusion, we consider a segregating granular mixture in what is arguably the simplest possible non-trivial 3D geometry, that of a spherical tumbler with periodic flow dynamics. Here we examine the so-called biaxial spherical tumbler (BST), where the spherical tumbler is half-filled with a size-bidisperse dry granular material and rotated alternately about two horizontal axes by angles (θ_z, θ_x) beyond the angle of repose. In experiments with the BST, different segregation patterns can be directly observed at the clear tumbler wall which depend on the values of the parameter pair (θ_z, θ_x). The angle the between two horizontal axes is kept constant at 90° in this work, but can be set to other values [94].

Mixing dynamics in the BST with monodisperse non-cohesive granular materials has a rich complexity [173]. For certain bi-axial spherical tumbler protocols, some particles are trapped for many iterations, M, of the protocol in periodic "non-mixing regions" while

other particles outside of these regions mix aperiodically. At the most fundamental level, the mixing dynamics of the BST can be thought of in terms of a cutting-and-shuffling operation that can be described by the mathematics of Piecewise Isometries (PWI) [78, 173, 77, 122, 121, 145]. Essentially, each change in the rotation axis "cuts" the material while the rotation "shuffles" the material to a different location. While the PWI approach to this problem provides a skeleton of the mixing and identifies the potential for non-mixing regions [78, 173, 77, 145] and invariant ergodic subsets that can result in barriers to mixing [95], its exact predictions are altered by the finite thickness of the flowing layer in physical realization of the BST [78, 24, 173, 77]. The physical flow with finite flowing layer thickness is accurately modeled by a time periodic 3D velocity field [24, 101]. An example of the flow structures predicted by the continuum flow model for the protocol $(57°, 57°)$ at a radius of $r = 0.95$ for a unit hemisphere is shown in Fig. 6.1(a) using a Poincaré section [152]. The Poincaré section is a stroboscopic map of points advected by flow in the tumbler (see Appendix C). The 3D kinematics are determined by decomposing the sphere into non-interacting 2D slices, neglecting axial velocity. For the $(57°, 57°)$ protocol, the continuum model predicts two groups of periodic non-mixing islands, A1-A2-A3 and B1-B2-B3. The chaotic region surrounding the non-mixing islands, illustrated by a scatter of points, is where chaotic mixing occurs [101, 24]. The boundaries separating the non-mixing islands and the chaotic region are intersections of the $r = 0.95$ shell (an invariant surface since the velocity field produces no radial displacement in the bulk) with six 3D Kolmogorov-Arnold-Moser (KAM) tubes. To visualize the 3D structures, non-mixing boundaries are isolated and assembled with invariant surfaces in the range $0.65 \leq r \leq 0.95$, as shown in Fig. 6.1(b). When viewed from the bottom of the tumbler, KAM tubes A2-A3 and B1-B2-B3 appear in obvious cone shapes, while KAM tube A1 appears as a set of nested ellipses. The cone-like KAM tubes, are widest near the tumbler wall [corresponding to the island boundaries shown in Fig. 6.1(a)] and their apexes point toward the core of the hemisphere. The shapes of the KAM tubes

vary with the protocol [24]. Previous experiments using an x-ray opaque tracer particle among otherwise monodisperse particles supported the existence of the 3D non-mixing regions [173, 171]. When the tracer particle is initially placed in A1, it periodically appears in regions labeled A1-A2-A3 for hundreds of iterations, occasionally jumping out and back into these non-mixing islands due to collisional diffusion, but otherwise corresponding closely to the continuum model where no material crosses the non-mixing island boundaries.

When a size-bidisperse mixture of particles is used instead of monodisperse particles, experiments show that segregation in the thin flowing layer near the free surface results in the large particle species accumulating in the non-mixing regions [171]. For example, a mixture of 5% large blue particles ($d_L = 4$ mm) and 95% small red particles ($d_S = 2$ mm) results in a segregation pattern that can be observed at the tumbler wall at $M = 30$ as shown in Fig. 6.1(c). Though only the middle portion of the tumbler can be easily imaged due to the steep curvature of the tumbler wall, it is apparent that large particles accumulate into non-mixing regions A1, B2, B3 corresponding to those in the Poincaré section Fig. 6.1(a,b) [171]. Furthermore, this segregation phenomenon is also observed in DEM simulations of size-bidisperse mixtures (see Appendix G for DEM simulation details), as shown in Fig. 6.1(d). The bottom view of the DEM simulation at iteration $M = 30$ is rendered in the same way as the photograph from experiment in Fig. 6.1(c) to allow easy comparison. Similar to the experiments, large blue particles accumulate into non-mixing islands labeled as A1, B2, and B3 in the DEM simulation. The curious aspect of this result, and the phenomenon that is the focus of this study, is that the non-mixing islands defined by their barriers to transport in the continuum model act as "attractors" for the large particles in a size bidisperse mixture.

Previously, we hypothesized that a secondary axial flow in the flowing layer of particles in a spherical tumbler [172] was a key element of the observed segregation patterns [171]. In this work, using DEM simulations, we aim to understand the complex interplay between the underlying advection field and segregation to uncover the mechanism behind the segregation

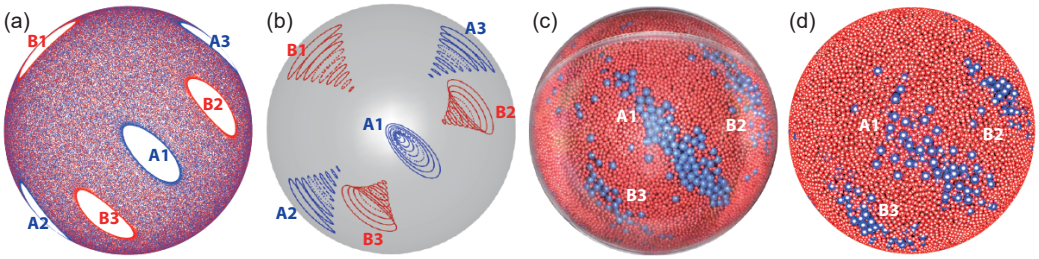

Figure 6.1. (a) Poincaré section of a half-full spherical tumbler for $r = 0.95$ with the $(57°, 57°)$ protocol. (b) Three-dimensional non-mixing KAM tubes visualized by transport barriers from continuum model for $0.55 \leq r \leq 0.95$ in increments of 0.05. The six conical-shaped non-mixing regions (A1-A2-A3 and B1-B2-B3) have period-3. (c) Segregation experiment in a half-full spherical tumbler ($D = 14$ cm) with 5% large blue particles ($d_L = 4$ mm) and 95% small red particles ($d_S = 2$ mm) after 30 iterations ($\omega = 2.6$) of the $(57°, 57°)$ protocol. (d) DEM simulation under identical conditions. All figures are viewed from below.

of large particles into the non-mixing regions. The 3D structure of the segregation patterns are examined in Chapter 6.2 using DEM simulations. The transport of particles in these non-mixing regions and the chaotic sea is discussed in detail to demonstrate the complex interplay between segregation, advection, and diffusion. Based on Chapter 6.2 and previous work [172, 173, 171], we propose that axial transport is a key element leading to segregation pattern formation that is missing from the original continuum model [24, 173]. To prove this hypothesis, axial transport is incorporated into the continuum model to effectively represent large particle movement in Chapter 6.3. Comparison of predictions of this modified continuum model with those from the unmodified model (no axial flow) demonstrates fundamental differences in the dynamical systems behavior related to accumulation of large particles in non-mixing regions. Finally, several examples of segregation in the BST for other protocols are provided to show that pattern formation can be predicted based on the same mechanism.

6.2. Non-mixing structures in 3D

Throughout this chapter, we consider a spherical tumbler that is half-filled with initially mixed size-bidisperse mixtures of non-cohesive mm-sized particles. The tumbler is repeatedly rotated about orthogonal axes by angles θ_z followed by θ_x, a protocol of (θ_z, θ_x). For each rotation, the granular bed is first rotated from horizontal to its angle of repose, then rotated by the specified angle, then rotated back to horizontal. Typically, 15-30 iterations of the protocol result in pattern formation [171]. Segregation patterns from DEM simulation with protocol $(57°, 57°)$ are compared to results from experiments [171] for the same conditions in Fig. 6.2. The rotation speed of tumbler in the DEM simulation is 3 rpm, similar to 2.6 rpm in experiments. The associated Froude number is about 6×10^{-4}, at the lower end of the rolling/cascading regime in tumbler flow where we expect a flat free surface with continuous flow [132, 102]. The DEM simulation is rendered using POV-Ray [1] in the same manner as the experiment is photographed from below. Similar to the experiment in Fig. 6.1(c), three distinct large particle regions are observed, corresponding to A1, B2, and B3 regions. The segregation patterns qualitatively match the experiments for a range of large particle fractions, shown in Fig. 6.2.

6.2.1. Trajectory of non-mixing regions and internal rotations

The validated DEM simulations allow us to better understand the movement of particles into and out of the non-mixing structures, shown in Fig. 6.2. For the example $(57°, 57°)$ protocol considered in detail here, each non-mixing structure returns to its starting position after three iterations (the periodicity of the non-mixing structure depends on the details of the protocol [122, 121, 145, 149, 94, 171]). For example in Fig. 6.1(a)-(b), A1 moves to the position of A2 after one iteration, to the position of A3 after two iterations, and returns to A1 after three iterations [145, 173]. During each rotation, one non-mixing island from each group (A and B) flows across the free surface where it is stretched due to the higher velocities

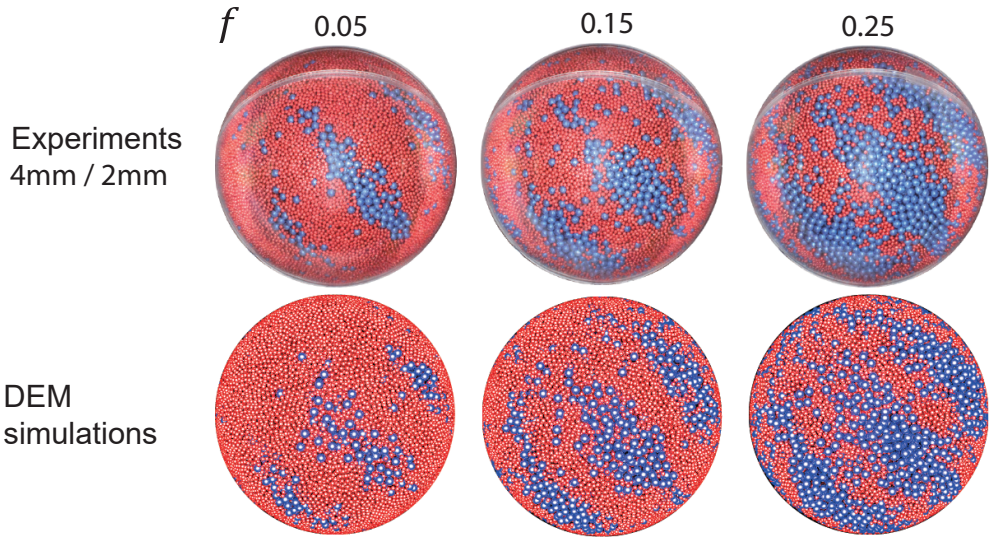

Figure 6.2. Comparison of segregation patterns in experiment (2.6 rpm) [171] and DEM simulation (3 rpm) at $M = 30$ for the $(57°, 57°)$ protocol using mixtures of 4 mm blue and 2 mm red particles with different large particle fraction f (columns).

in the flowing layer. When particles return to the bulk after flowing down the free surface, the non-mixing islands recover their unstretched shape. The transformation of non-mixing islands as they cross the free surface can be visualized by tracking the large particle clusters, as shown by snapshots of the DEM simulation in Fig. 6.3. This process is also illustrated in Video.[1] Side views of the DEM simulation highlight the movement of non-mixing region A3 as it spreads and then contracts on successive passes across the flowing surface layer corresponding to θ_z and θ_x rotations. Large particles are shown as blue spheres while small particles are transparent. The orientation of the tumbler is offset by the angle of repose to simplify visualization. Particles associated with cluster A3 are colored gold and the region around them is manually highlighted to aid visualization. The direction of flow on the free surface is indicated by the red arrow.

As shown in Fig. 6.3, the large particles mostly accumulate in the six non-mixing regions with a smaller number scattered elsewhere throughout the domain. During the z-axis rotation (left column), region A3 is rotated up from the solid body region into the flowing

[1]Link to Video

layer. At 2/3 of the z-axis rotation (third row), region A3 is stretched out in the flowing layer. At the same time, although it is not highlighted, the non-mixing region B1 on the far left side is also stretched as it also flows down the free surface. At the end of the z-axis rotation, both regions A3 and B1 land on the opposite side of the flowing layer across the z-axis. In the subsequent x-axis rotation, region B1 is buried in the bulk and undergoes solid body rotation, while the highlighted region A3 enters the flowing layer again. At 1/3 of the x-axis rotation, region A3 spreads out but condenses itself at 2/3 rotation as it nears the end of flowing layer. Region B3 also flows down the surface during this portion of the iteration. After this bi-axial iteration, region A3 lands on the far left corner of the surface where A2 had started at the beginning of this iteration. The motion of A3 is different during the two rotations that define the protocol. The stretching of region A3 happens mostly in the latter 2/3 of the first rotation (θ_z), while it occurs in the first 2/3 of the second rotation (θ_x). This is because A3 is closer to the free surface at the end of the first rotation than at the start. Regions A2, A3, and B2 do not pass through the flowing layer at all during this iteration, but do so during subsequent iterations. With two additional iterations of the protocol, all non-mixing regions pass through the flowing layer and return to their starting positions. However, only the center of the non-mixing regions is periodic as the rest of the region rotates about this fixed point [145]. The amount of internal rotation is determined by the protocol and particle fill level [149]. This internal rotation becomes important as we explore large particle accumulation into the non-mixing regions.

6.2.2. Distribution of large particles in non-mixing regions

The structures of the large particle accumulations in non-mixing regions can be analyzed quantitatively from the DEM simulations and compared with non-mixing regions predicted by the continuum model. The average concentration of large particles at the surface of the tumbler after the segregation pattern fully develops is shown in Fig. 6.4 by projecting the

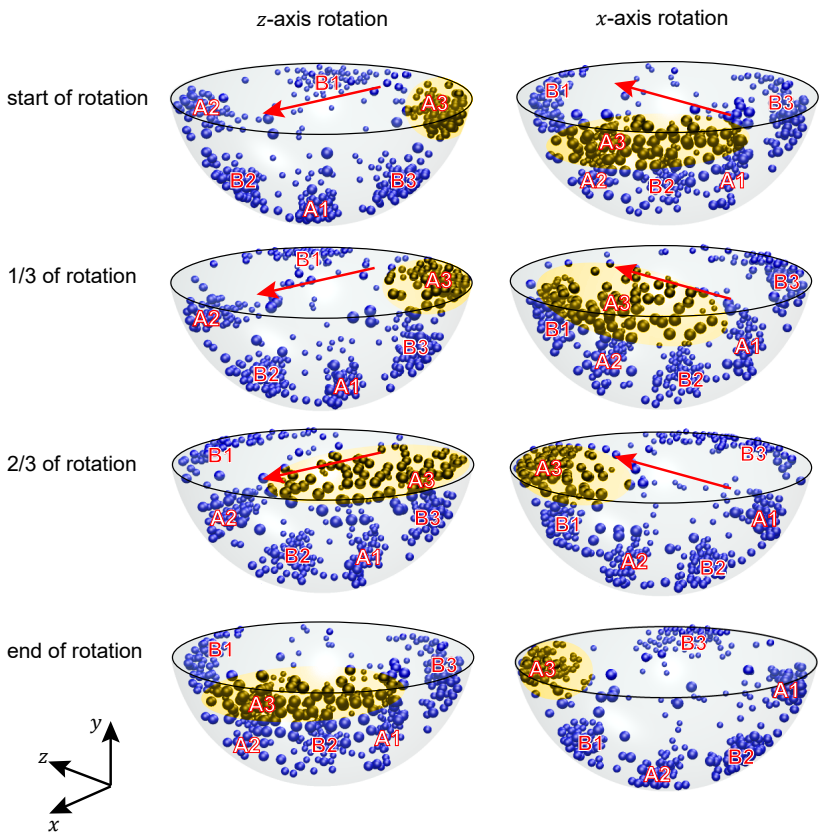

Figure 6.3. Illustration of large particle movement in a DEM simulation during the $M = 31$ iteration of the $(57°, 57°)$ protocol for an initially mixed mixture of 15% 4 mm particles and 85% 2 mm particles of equal density. The free surface edge boundary is indicated by the black ellipse. Arrows indicate direction of flow on the top of the flowing layer. After one iteration, two groups of non-mixing clusters A1-A2-A3 and B1-B2-B3 rearrange their locations as indicated by labels. Tumbler is visualized so that free surface is horizontal.

position of all particles in a hemispherical shell of thickness $0.9 < r < 1$ onto a 2D plane using a Lambert azimuthal projection [150] with equal discrete areas [164, 121]. Large particle concentrations are high in the six dark elliptical regions associated with non-mixing regions A1-A3 and B1-B3 for all three large particle fractions, f. The boundaries of non-mixing islands predicted by the continuum model are also projected to the 2D plane in the same manner, as shown by the closed red curves. For f=0.05 [Fig. 6.4(a)], almost all large particles accumulate in the non-mixing regions predicted by the continuum model. At $f = 0.15$ [Fig. 6.4(b)], the high concentration regions increase in size and remain elliptical. At $f = 0.25$

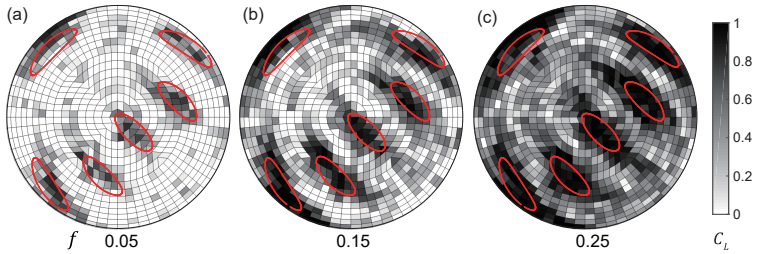

Figure 6.4. Large particle concentration averaged over iterations ($25 \leq M \leq 35$) and dimensionless radius ($0.9 < r < 1$) under the protocol $(57°, 57°)$ for increasing (left to right) large particle fraction $f =$ as indicated. Concentration fields are visualized using a Lambert azimuthal projection which preserves area between the 3D hemisphere and the 2D plane. Boundaries of non-mixing islands predicted by continuum model are indicated by red closed curves.

[Fig. 6.4(c)], the high concentration regions cover much of the domain, because there are too many large particles to fit within the non-mixing regions due to radial segregation (discussed below). Nevertheless, the non-mixing regions are higher in concentration of large particles compared to the rest of the domain, meaning large particles still prefer to accumulate around non-mixing regions. The concentration map (and associated segregation) pattern remains stable for the entire simulation after it initially develops, which takes about 15 iterations of the protocol.

The continuum model results indicate that, in the absence of segregation, non-mixing regions extend radially inward from the wall of the spherical tumbler in a conical shape, as shown in Fig. 6.5. To examine the 3D structure of the particle accumulations in the non-mixing regions, we examine a slice through the particle bed that cuts through non-mixing regions A1 and B1 as shown schematically in Fig. 6.5 (a). The images in column (b) are snapshots of DEM simulations at $M = 30$. Compared to the boundaries of the non-mixing regions of A1 and B1 based on the continuum model (white dotted curves), the large particles roughly fall into the same area, but only occupying regions near the tumbler wall. This is readily explained by size segregation. Large particle tend to rise to the surface when they cascade down the flowing layer to end up near the wall of the tumbler, while small particles

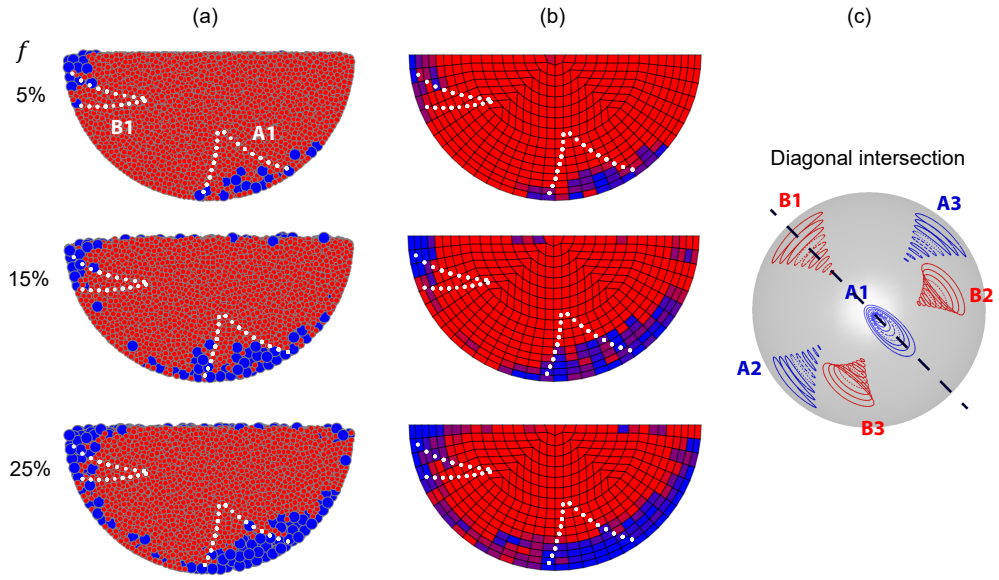

Figure 6.5. Particles ($M = 30$) (a) and average concentration ($25 \leq M \leq 35$) (b) showing segregation patterns for different large particle fractions viewed on the intersecting plane indicated by dashed line in (c) under the $(57°, 57°)$ protocol. Dashed curves in (a,b) indicate boundaries of the 3D cone-like non-mixing regions (KAM tubes) illustrated in (c).

tend to fall to the bottom of the flowing layer to deposit before they reach the tumbler wall at the downstream end of the flowing layer. Consequently, there is a natural tendency for large particles to be near the tumbler wall and small particles further inward. As the large particle fraction is increased from 0.05 to 0.25, the non-mixing regions are packed more densely with large particles, yet still only in a 3-4 particle diameter thick layer near the tumbler wall. Meanwhile, large particle accumulation expands tangentially along the tumbler wall, while also occupying the free surface. With a higher fraction of large particles, the tendency for them to reside inside non-mixing regions competes with their tendency to segregate to the top of the flowing layer and then deposit near the tumbler wall. When the non-mixing regions near the tumbler wall become more fully occupied at greater large particle fractions, large particles eventually accumulate near the tumbler wall but outside the non-mixing regions. Concentration fields averaged over iterations $25 \leq M \leq 35$ in column

(c) show the distribution for large particles is within and near the non-mixing regions at the wall, but does not extend far into the core of the particle bed.

6.2.3. Relating flow dynamics and segregation patterns

Having confirmed that the DEM simulations reproduce the robust segregation patterns observed in experiments, the outstanding question is why do large particles that segregate to the surface of the bed accumulate within the non-mixing islands? First, recall that the six non-mixing regions predicted from the continuum model consist of two groups of period-3 regions, namely A1-A3, and B1-B3, as labeled for the 3D conical shaped non-mixing structures in Fig. 6.5(a). Particles within these structures follow a periodic itinerary that, at each iteration, passes sequentially through each region (A or B). For example, a particle starting in region A2 moves to A3, A1, and then back to A2 with each iteration of the protocol. Thus, the periodic dynamics can be quantified by the net angular displacement over iterations of integer multiples of the periodicity, namely $3n$ iterations for period-three behaviors. Here, we measure net angular displacement of particles (maximum of π), denoted as S, as a function of starting locations over two periods (6 M) in Fig. 6.6 and six periods (18 M) in Fig. 6.7. The results are shown in bottom views of the spherical tumbler presented in Lambert equal area projections as mentioned above. Particles with $0.8 < r < 1$ are sampled after the initial transient, for iterations $13 \leq M \leq 35$ of DEM simulations starting with a mixed initial condition of various f. In both figures, results are shown for large particles in the top row and small particles in the bottom row for $f = \{0,\ 0.05,\ 0.15,\ 0.25,\ 1\}$. Note that $f = 0$ and 1 cases are size monodisperse systems with only small or large particles, respectively, and thus the concentration for the other species is zero and the corresponding figures are not shown.

Over the two periods of the flow shown in Fig. 6.6, six distinct regions of small displacement (dark areas) are apparent for both large and small particles. These regions correlate

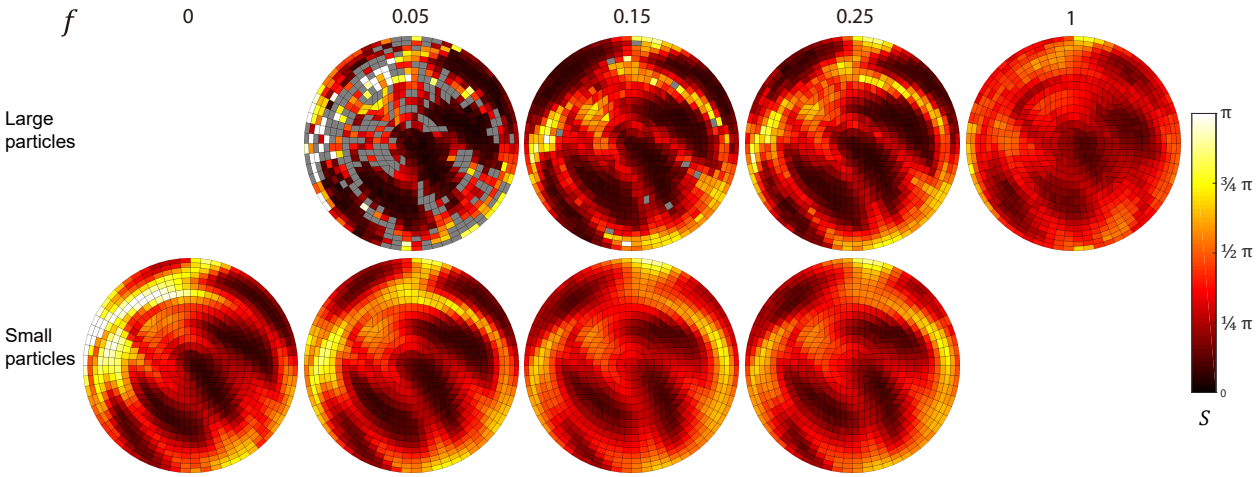

Figure 6.6. Net angular displacement (S) of larger 4 mm particles (top row) and smaller 2 mm particles (bottom row) over two flow periods during iterations ($13 \leq M \leq 35$) of protocol $(57°, 57°)$ for mixtures with large particle fraction varying from 0 to 1. Grid cells which never contain a large particle occurrence are indicated in gray.

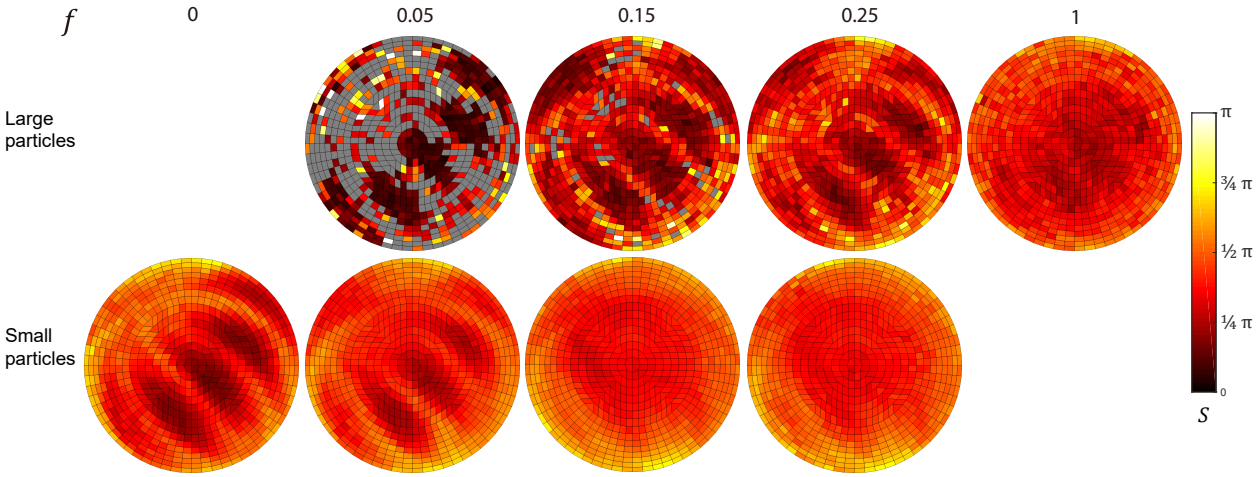

Figure 6.7. Net angular displacement (S) of larger 4 mm particles (top row) and smaller 2 mm particles (bottom row) over six flow periods during iterations ($13 \leq M \leq 35$) of protocol $(57°, 57°)$ for mixtures with large particle fraction varying from 0 to 1. Grid cells which never contain a large particle occurrence are indicated in gray.

with large particle clusters and non-mixing regions in the continuum model and indicate that particles tend to return to their local neighborhoods near the non-mixing regions after every six iterations. The two groups of period-3 regions (A and B) do not differ from each

other since they are mirror images of each other one-half iteration apart. They have the same periodicity and, consequently, the same net angular displacement.

The variations in the details of these patterns across different compositions can be explained by the associated dynamics of the mixture in the system. In size-bidisperse cases ($f = \{0.05, 0.15, 0.25\}$), regions of small displacement for large particles are similar in size despite increasing numbers of large particles. Note that for $f = \{0.05, 0.15\}$, gray bins indicate regions where no large particles were present due to the low fraction of large particles in the mixture. With a higher large particle fraction ($f = 0.25$), large particles tend to stay close to the tumbler wall but cannot all accumulate in the small angular displacement regions. As a consequence, large particles outside non-mixing regions are dispersed into the rest of the domain leading to higher concentrations away from the low displacement regions [Fig. 6.4(c)]. More interestingly, small particles also exhibit a similar robust pattern for small displacement regions. The reason that only large particle clusters are observed in Fig. 6.2 is because large particles radially segregate to the tumbler wall. When particles are sampled in a 3-4 particle diameter layer close to the tumbler wall, the non-mixing regions near the wall are mostly covered by large particles. However, under the first layer of large particles, there are small particles as well, as is clear in Fig. 6.5. Thus, both small and large particles tend to stay in the period-3 non-mixing regions over two periods. Even in the two monodisperse cases ($f = \{0, 1\}$), similar periodic dynamics are observed. The pattern is arguably clearer for $f = 0$, likely due to the smaller collisional diffusion of small particles (which scales with the square of the particle diameter [13, 161, 46]) to bump particles in or out of non-mixing regions. However, for both bidisperse and monodisperse mixtures, the regions of lowest angular displacement differ slightly for small and large particles. For example, in size bidispserse cases, the central low displacement region resides close to the center for large particles but is closer to the periphery for small particles. This slight shift in periodic features is likely a consequence of the slight difference in the flow of the two particle species in

the flowing layer (i.e. small particles re-enter the bulk before large particles). Nevertheless, these results demonstrate that periodic dynamics of non-mixing regions are observed in both size-bidisperse and -monodisperse systems and that they are consistent across different particle species over short time periods. Thus, the underlying mechanism for pattern formation is inherent to the tumbler dynamics and not a result of the bidispersity of the mixture. The segregation pattern formation is made visible with large particles on the tumbler wall, but non-mixing structures exist independently of the bidispersity of the granular system.

While Fig. 6.6 shows that the periodic dynamics of particles in the non-mixing regions are robust across various mixtures, behavior over larger numbers of iterations is also of interest. Net angular displacement results over six flow periods (18 M) are shown in Fig. 6.7for the same set of simulations. In size-bidisperse cases with $f = \{0.05, 0.15, 0.25\}$, a similar pattern of six low displacement regions is observed compared to Fig. 6.6. Due to collisional diffusion between particles that bumps particles in and out of the non-mixing regions over the longer period of time, the displacements at the centers of the region is larger. The pattern of low displacement regions is weaker for small particles in bidisperse mixtures even though the periodic dynamics of non-mixing regions persist for monodisperse small particles ($f = 0$). This is likely because of two reasons. First, in size-bidisperse cases, small particles are pushed away from the tumbler wall and down to the hemisphere core where the non-mixing region decreases in size [Fig. 6.5(a)]. Thus, compared to $f = 0$ where small particles are right against the tumbler wall, fewer small particles follow the periodic movement of the non-mixing region. Secondly, in size-bidisperse cases in the non-mixing region, small particles are dispersed among large particles in the 3-4 particle diameter layer near the tumbler wall so that the diffusion is higher than for monodisperse small particles. The influence of diffusion is also obvious for large particles at $f = 1$, where the low displacement regions disappear.

Thus, flow in the spherical tumbler under the $(57°, 57°)$ protocol manifests periodic behaviors regardless of whether the mixture is monodisperse or bidisperse. The underlying

flow is elemental for segregation pattern formation, and the periodic dynamics is inherent to the flow independent of segregation driven by particle size differences. However, why large particles accumulate in the non-mixing regions remains unanswered.

6.3. Pattern formation mechanism

In Chapter 5 describing experiments like those in Fig. 6.2 [171], the correspondence between experimental segregation patterns and the location of non-mixing regions based on continuum model analysis suggests that material transport across boundaries of non-mixing regions is hindered. The monodisperse cases shown in Fig. 6.6 and Fig. 6.7partially confirm this result. The material transport that occurs across the mixing barriers is readily explained by collisional diffusion in the monodisperse cases. However, in size-bidisperse cases, there is preferential clustering of large particles in these non-mixing regions, which seemingly contradicts the barriers to transport evident in the continuum model. The question is how do the large particles preferentially accumulate in the non-mixing regions, given that both experiments and simulations begin with mixed particles? Clearly, the large particles must somehow preferentially cross the barriers to mixing during an initial transient phase to cluster in the non-mixing regions evident in Figs. 6.1 and 6.2. While the motion of these clusters of larger particles is evident in Fig. 6.4, this does not explain the mechanism that creates them. Moreover, Figs. 6.6 and 6.7indicate that the segregation patterns and the flow dynamics are similar in monodisperse and bidisperse systems, but they do not provide insight into how large particles accumulate in the non-mixing regions in the first place.

We propose that the explanation for why large particles accumulate in non-mixing regions lies in the weak axial transport that occurs in spherical tumbler flows [172]. What is missing from the continuum model used to generate Fig. 6.1 (a,b) is the axial transport that we hypothesized in our previous study [171] as an important driving force for the segregation pattern. This hypothesis was based on previous studies of axial drift in a spherical tumbler

under single axis rotation with monodisperse particles [172], as well as the axial segregation pattern that occurs in spherical tumblers with size-bidisperse mixtures rotating continuously about a single axis [34, 18, 45]. In this section, the role of axial transport in forming segregation patterns is discussed in further detail.

6.3.1. Axial transport

During each rotation of the bi-axial protocol, the flow is fully 3D. Particles are advected not only in the streamwise direction but also in the axial direction. This axial transport is often neglected because it is so small compared to the streamwise transport or plays no significant role in the segregation, for example in quasi-2D tumblers due to the narrow width of the tumbler. However, for tumblers of significant width, including long cylinders, spherical tumblers, and double cone tumblers rotating about their axes, the effects of axial transport can be significant [66, 18, 172, 34, 21]. For example, Zaman et al. measured axial transport of monodisperse granular materials in a half-filled spherical tumbler rotating continuously about a single axis in a similar setup to that used here [172]. They found that particles move toward the poles when they are near the surface of the flowing layer and toward the equator when they are deep in the flowing layer. The axial drift of particles on the free surface is on the order of one particle diameter (about 2% of the tumbler diameter) per pass through the flowing layer, a result which they confirmed with DEM simulations.

To characterize the magnitude of the axial drift in the size-bididsperse system considered here, we measure the axial drift per pass of all of the large particles in the flowing layer as a function of axial position for $1 \leq M \leq 15$ during the initial transient phase starting from a fully mixed initial condition, as shown in Fig. 6.8. The data points indicate instances of measured drift per flowing layer pass in the axial position, Δ, divided by large particle diameter, while the yellow curve shows the average of these measurements (averaged over bins of width of one large particle diameter in the axial direction). The average axial drift is

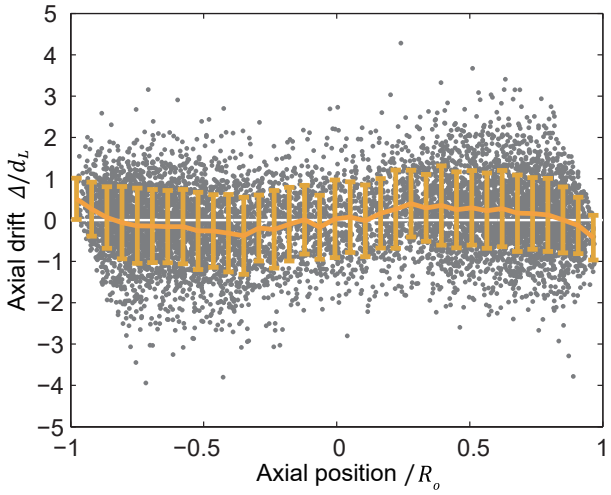

Figure 6.8. Axial drift per flowing layer transit of large particles scaled by large particle diameter vs. axial position scaled by tumbler radius R_o for DEM simulation with initially mixed large (4 mm) particles and small (2 mm) particles under the $(57°, 57°)$ protocol during the initial transient phase $(1 \leq M \leq 15)$. Gray points represent individual data points, while the yellow curve represents the binned average value and its standard deviation (error bars).

anti-symmetric with respect to the equator. Large particles move toward the poles (negative drift to the left of the equator and positive drift to the right of the equator) except near the pole where large particles move away from the poles, since only small particles can sustain contact with the tumbler wall in the thin flowing layer at the poles [18, 45, 34]. The magnitude of the axial drift in Fig. 6.8 is about half that found by Zaman et al. [172]. The smaller magnitude is likely due to a slower rotation speed and consideration of all large particles in the flowing layer rather than just those visible at the tumbler wall in solid body rotation [172]. The change of rotation axes in the biaxial protocol could also contribute to a smaller axial drift than that measured for single axis rotation since particles dilate during flow.

6.3.2. Modified continuum model

Given the axial drift that is evident in Fig. 6.8, it is logical to modify the continuum model to include axial transport as an essential element to segregation pattern formation. In the previous continuum model [24, 173], the 3D geometry was simplified by considering non-interacting 2D slices in the axial direction with velocities in the streamwise direction only. In the modified continuum model, we also include the axial drift. We do not consider particle mass or size, but only velocities according to the tracer point positions. In this way, by incorporating the measured axial velocity of large particles, we effectively track large particles in the flow of a size-bidisperse mixture after large particles segregate to the free surface. Note that the flow is not strictly incompressible in the modified continuum model, because we only track large particles while neglecting small particles that migrate in the opposite direction. Nevertheless, this allows us to quantitatively illustrate the propensity for large particle movement under the influence of both the bi-axial protocol and the weak axial drift.

The axial velocity is obtained from DEM simulations by tracking large particles in the flowing layer and recording the axial velocity of each particle as it progresses in the flowing layer on a 30×30 grid, where each grid cell is about one large particle diameter (d_L) in both x and z directions. Large particles that travel for at least half of the rotation action are tracked to exclude those that are only briefly in the flowing layer (i.e. at the beginning or end of the rotation). The tracking sequence starts with any large particle that is within d_L of the free surface, noting that large particles readily segregate to near the free surface of the flowing layer. The tracking sequence ends when the streamwise velocity reverses sign, which corresponds to when a particle deposits into the bulk. Axial velocities of particles are recorded in each grid cell every 0.1 s (corresponds to a tumbler rotating of 1.8 ° at a 3 rpm rotation rate) over the entire tracking sequence (one flowing layer pass consists of about 18-20 recordings of axial velocity). The axial velocities are sampled over the initial 15

iterations of the simulation for eight different simulations with $f = 0.15$, and then averaged. The axial flow is localized in four distinct 3 to 4 particle diameter wide regions located along the curved tumbler wall near the poles on both the upstream and downstream sides. This observation agrees with the conclusion in a previous study that axial drift is a result of the axial slope of the bounding wall [172].

The modified continuum model, including the velocity field in the streamwise and depthwise directions from the original continuum model and the additional axial drift velocity in the flowing layer, is described in Appendix C. The effect of the axial velocity is illustrated in Fig. 6.9 for an example particle starting to the left of the equator at $\boldsymbol{x}_o$. A particle flowing down the free surface with only streamwise velocity $\boldsymbol{v}_{st}$ reaches point $\boldsymbol{x}_f$, maintaining a constant axial position. When an axial velocity $\boldsymbol{v}_{ax}$ is added to the streamwise velocity, the particle follows a curved trajectory (as $\boldsymbol{v}_{ax}$ changes along the trajectory) and arrives at $\boldsymbol{x}'_f$. The curvature of the trajectory in the sketch is exaggerated and collisional diffusion is not included for easier visualization. Depending upon where a particle enters the flowing layer, the curvature of the trajectory will vary. The axial drift toward the poles occurs at the surface of the flowing layer [172], so in a bidisperse system where large particles naturally segregate to the surface, they tend to preferentially drift toward the poles except within a few particle diameters of the poles. In addition to the axial velocity, the effect of diffusion is included in the modified continuum model as noted using a random walk approach in which a multiple of the standard deviation σ_{ax} of the measured axial velocity is, with equal probability, added to or subtracted from the mean axial velocity at each time step. Hence, the imposed diffusion is not related to concentration gradient or other possible diffusion mechanisms, such as Taylor dispersion. Although this model is simple, it captures the major elements of the flow dynamics including advection by the streamwise and axial velocities and diffusion. Segregation is implicitly included in the model. First, the axial velocity is based on the large particle motion only. Second, large particles segregate to the surface of

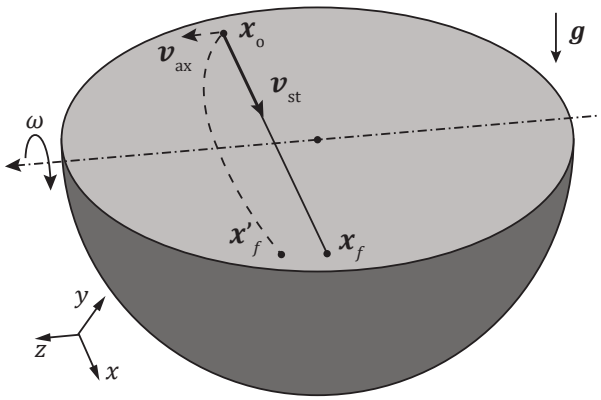

Figure 6.9. Sketch of flowing layer trajectories with axial velocity, $\boldsymbol{v}_{ax}$ and streamwise velocity, $\boldsymbol{v}_{st}$ (dashed curve) and model with streamwise velocity, $\boldsymbol{v}_{st}$ only (straight line) showing net poleward displacement of the former. Trajectory curvature is exaggerated for clearer visualization.

the flowing layer and, hence, remain near the tumbler wall when embedded in the bed of particles undergoing solid body rotation. It is near the tumbler wall where the non-mixing islands appear, as shown in Fig. 6.5.

6.3.3. Dynamics of the modified continuum model

Continuum model tracking of tracer points for the protocol $(57°, 57°)$ with implementation of measured axial velocities is shown as viewed from the bottom of the spherical tumbler in Fig. 6.10. The initial condition in the top row consists of 2000 tracer points randomly distributed on a hemispherical shell of dimensionless radius $r = 0.95$ (d_L from the tumbler wall). The advection scheme used in the modified continuum model ensures that the tracer points stay on this hemispherical shell so that they represent large particles close to the tumbler wall due to segregation. Distributions of tracer points at $M = 30$ are shown in the middle row of Fig. 6.10, and cumulative tracer point positions ($30 \leq M \leq 45$) are shown in the bottom row along with red closed curves corresponding to the non-mixing islands reproduced from the original continuum model without axial velocity. We compare results for the original continuum model without axial velocity or diffusion in the left column

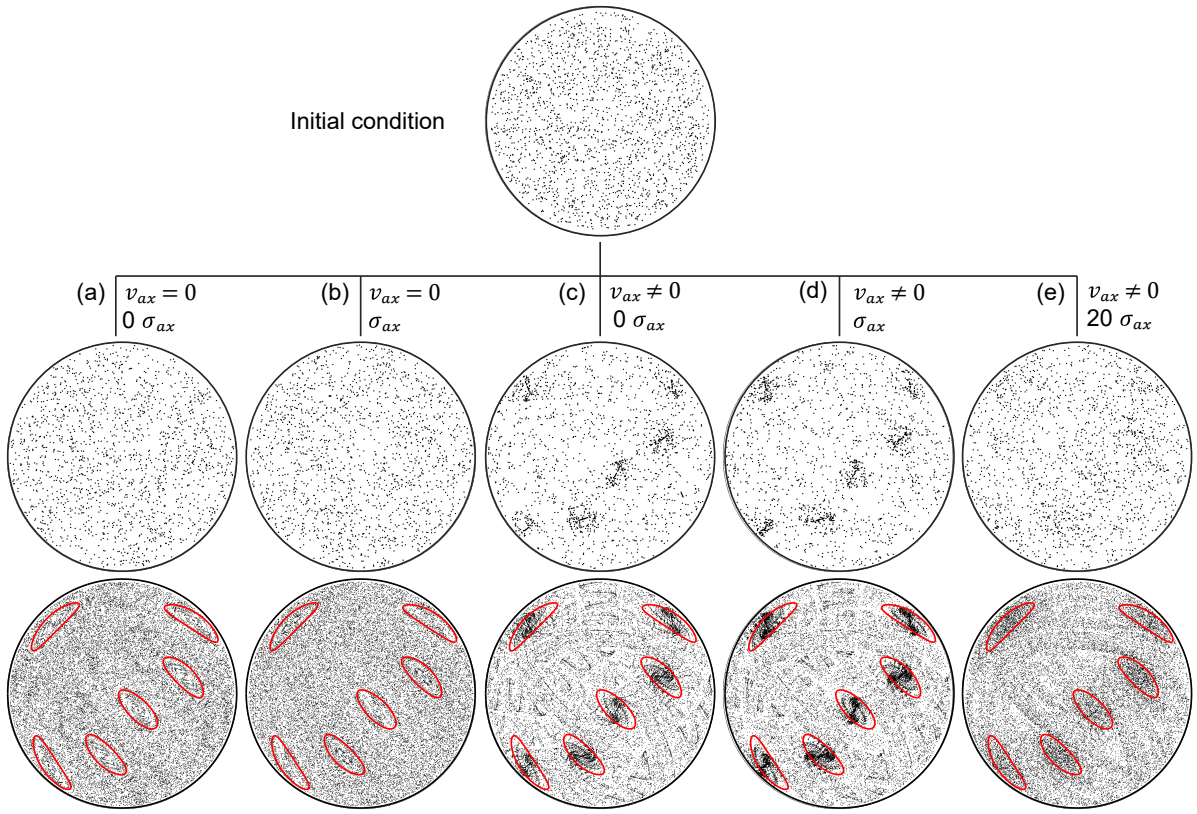

Figure 6.10. Continuum model simulation of $(57°, 57°)$ protocol: (a) without axial drift or diffusion; (b) random walk diffusion only; (c) with axial velocity but no additional diffusion; (d) with axial velocity and diffusion of σ_{ax}; (e) with axial velocity and diffusion of 20 σ_{ax}. (Top row) Initial random distribution of tracer points. (middle row) Tracer point distribution at $M = 30$ showing clustering in (c,d). (bottom row) Cumulative tracer point positions for $30 \leq M \leq 45$.

(a) with the modified continuum model incorporating only a random-walk diffusion of σ_{ax} (b), the measured axial velocity field only v_{ax} (c), and combined axial velocity and higher levels of as well as additional diffusion of σ_{ax} (d) and 20 σ_{ax} (e). Immediately obvious in column (a) is that tracer points remain randomly distributed everywhere in the domain for the continuum model without axial velocity or diffusion. The distribution of tracer points remains random after adding diffusion as shown in column (b), indicating that diffusion alone does not cause large particles to accumulate in non-mixing regions. Including the axial velocity in the modified continuum model in (c) results in a non-uniform distribution of

tracer points with a fraction of them accumulating in non-mixing regions (red closed curves) after 30 iterations, while the rest distribute randomly in the domain at a lower density than in (a) and (b). Thus, axial velocity drives tracer points into the non-mixing regions and is a necessary component for segregation pattern formation in bi-axial spherical tumbler flows.

With diffusion, σ_{ax}, in column (d), tracer point clusters are slightly larger and less dense compared to no diffusion in (c), because diffusion redistributes them more broadly in the non-mixing regions. The greater diffusion also results in the randomly distributed tracer points in the remainder of the domain to be at a slightly higher density than in (c). At 20 σ_{ax} in column (e), the accumulation of tracer points is not obvious at $M = 30$ (middle row), though it is slightly discernible cumulatively over the next 15 iterations (bottom row). In this case, the attraction of points into non-mixing regions is weak compared to redistribution by diffusion, consistent with the effect of diffusion on net angular displacements (Fig. 6.6 and 6.7), where the mean angular displacement increases with increasing iterations due to collisional diffusion.

Although the modified continuum model is ad hoc, it clearly demonstrates the importance of two factors necessary for pattern formation. First, the modified continuum model predicts accumulation of tracer points in the non-mixing islands found from the original continuum model without an axial velocity component, suggesting the importance of the overall flow dynamics in forming the non-mixing islands themselves. Second, comparing the continuum models with and without axial velocity demonstrates that the axial velocity of the large particles is necessary for large particles to be transported across nominal mixing barriers and accumulate in the non-mixing regions. Moreover, additional diffusion in the system prevents the accumulation of tracer points in the non-mixing islands as it forces tracer points across barriers to mixing, which is consistent with observation of large diffusion and disappearance of segregation pattern in systems with small size ratios where segregation is weak [171].

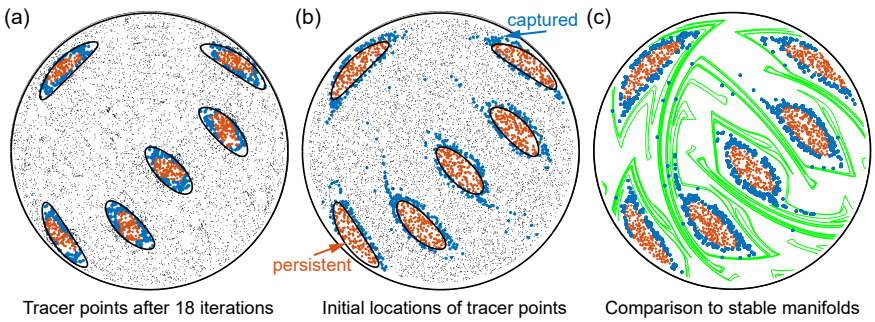

Figure 6.11. (a,b) Tracking tracer points through barriers to mixing over six periods of $(57°, 57°)$ protocol for the modified continuum model with axial transport and no diffusion. Tracer points remain in (orange) or enter (blue) the non-mixing regions or stay in the chaotic region (small black dots). (c) Tracer points entering the non-mixing regions (blue) tend to follow the stable manifolds (green).

The next question is how does the axial velocity enable particles to form clusters? To answer this question, we track tracer points that enter non-mixing regions over multiple iterations as shown in bottom views of the hemispherical tumbler in a Lambert azimuthal projection Fig. 6.11. Here, we focus on demonstrating the effect of the axial velocity without diffusion. Tracer points are initiated evenly distributed on a hemispherical shell of $r = 0.95$ and in the corresponding portion of the flowing layer and advected for six periods (18 iterations) of the $(57°, 57°)$ protocol. Tracer points in the non-mixing islands are identified and highlighted by larger markers with color to differentiate them from points in the chaotic region [Fig. 6.11(a)]. Although the density of tracer points appears to decrease after 18 iterations, this is merely a consequence of some tracer points condensing into small regions throughout the flow domain. The initial locations of tracer points that end up in the non-mixing islands are indicated in Fig. 6.11(b). Tracer points that start in non-mixing islands and persist in the islands are highlighted in orange. They tend to be in the center of non-mixing islands at $M = 18$ [Fig. 6.11(a)] and fill the entire non-mixing islands initially [Fig. 6.11(b)], suggesting that they move toward the center of the islands with increasing iterations. Tracer points at the periphery of non-mixing islands at $M = 18$ are highlighted in blue. Initially, they start outside of the non-mixing islands in Fig. 6.11(b) and are captured

into the non-mixing islands over 18 iterations. Although most blue tracer points initially surround non-mixing islands, a few originate from within the chaotic region [Fig. 6.11(b)].

The trails of blue tracer point initial locations extending from the non-mixing islands into the chaotic region resemble manifolds found previously [171]. Stable manifolds based on the original continuum model shown by the green curves in Fig. 6.11(c) almost perfectly overlay the initial locations of many of the blue tracer points. This correspondence suggests stable manifolds persist even with the additional axial velocity and play an important role in facilitating the accumulation of tracer points. We speculate that tracer points on these stable manifolds approach the non-mixing islands and when in the vicinity of non-mixing islands, they are then pushed into the island by the axial velocity. If stable manifolds did not encompass the non-mixing islands, tracer points would take longer to get there or simply not get close enough to enter the non-mixing islands at all. Additionally, the internal rotation of non-mixing regions may play a role in sustaining the material inflow from the longitudinal ends. As mentioned in Chapter 6.2.1, each non-mixing region rotates about its periodic fixed point every period, the rotation is close to π for the $(57°, 57°)$ protocol in this example. Thus, tracer points approach the elliptical non-mixing islands from both ends over two periods.

6.3.4. A similar bi-axial protocol

Although we have focused much of this study on the $(57°, 57°)$ protocol, segregation patterns appear in the bi-axial spherical tumbler for other protocols [171]. For example, the $(90°, 90°)$ protocol shown in Fig. 6.12, results in non-mixing regions of period 2. The average concentration of large particles near the tumbler wall ($0.9 \leq r \leq 1$) in a DEM simulation for this case is shown in Fig. 6.12(c). Dark regions representing high large particle concentrations match well with continuum model prediction of non-mixing islands, shown as red closed curves. Again, the implementation of axial velocity in the modified continuum model results in tracer points accumulating in non-mixing regions, as shown in Fig. 6.13.

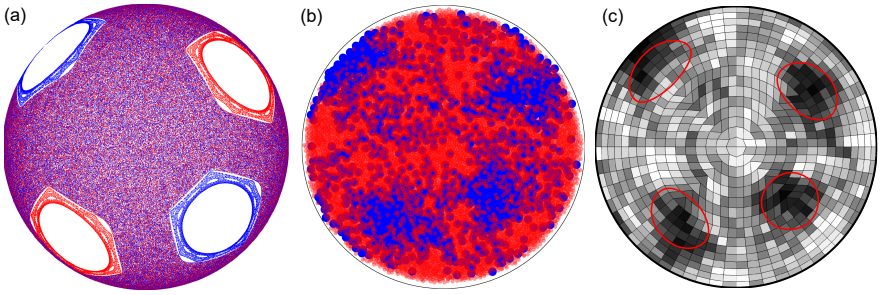

Figure 6.12. (a) Bottom view of the Poincaré section of a half-full spherical tumbler at $r = 0.95$ with protocol $(90°, 90°)$. (b) Lambert projection of distribution of particles $(0.9 \leq r \leq 1)$ in DEM simulation of a half-filled spherical tumbler with a mixture of 15% 4 mm large particles and 85% 2 mm small particles at $M = 30$ of the same protocol. The red particles are semi-transparent to make blue particles visible. (c) Average concentration of large particles $(0.9 \leq r \leq 1)$ in the DEM simulation for $0 < M < 30$. Boundaries of non-mixing islands predicted by the continuum model are indicated by red curves.

That is, axial velocity with moderate diffusion results in tracer points accumulating in the non-mixing regions.

Tracking tracer points in the modified continuum model over multiple iterations shown in Fig. 6.14 demonstrates again that axial velocity enables transport of tracer points through mixing barriers, both those in the immediate vicinity of the island and those far away in the chaotic region [Fig. 6.14(b)]. The internal rotation in this case is close to 144° (equivalent to $4/5\ \pi$), thus giving rise to the slightly pentagonal shape of blue tracer points surrounding the non-mixing islands. As in the previous case, the blue tracer points approaching the non-mixing islands follow the stable manifolds shown by the green curves in Fig. 6.14(c). Like the $(57°, 57°)$ protocol, tracer points under the $(90°, 90°)$ protocol that initially occupy the entire non-mixing island (orange) [Fig. 6.14(b)] are compressed into the island centers at $M = 18$ [Fig. 6.14(a)]. Since the movement of tracer points in the continuum model is independent of concentration (i.e., tracer points can overlap), the blue tracer points that occupy the periphery of non-mixing islands at $M = 18$ will continue to migrate toward the island center as well.

For both the $(57°, 57°)$ and $(90°, 90°)$ protocols, the original continuum model predicts non-mixing islands that have significant size and can influence mixing and segregation. The boundaries of these non-mixing islands were understood as barriers to mixing in previous studies [173, 171]. By considering axial velocity in a modified continuum model, which effectively tracks large particles in the transient phase of a segregating mixture, the periodic fixed points in the center of the periodic non-mixing islands become sinks [152]. Therefore, during the initial transient, the barriers to mixing are disrupted. Tracer points in the chaotic region follow stable manifolds to approach the original non-mixing islands and cross the barriers under the influence of the axial velocity. In experiments, because particles cannot overlap, large particles accumulate in the original non-mixing islands and can even expand outward from the non-mixing island in some cases. Once large particles have migrated into these regions, axial transport is balanced by diffusion and contact forces which limit the density of particles, and the system reaches a stable state.

6.3.5. A global transport barrier

Another case we consider is the $(45°, 45°)$ protocol which differs from previous examples in that there are no large non-mixing islands. Similar to Fig. 6.1(a) and Fig. 6.12, a Poincaré map is generated by tracking points seeded on the interface between the bulk and flowing layer intersecting the hemispherical shell at $r = 0.95$. The blue and red points correspond to points initially seeded at the start of the z-axis and x-axis rotations, respectively. Unlike the distinct non-mixing islands obtained in previous examples, the Poincaré map shows interpenetrating fingers separated by a global mixing barrier [173, 171], as shown in Fig. 6.15(a). Though thin strips of non-mixing islands exist in each "finger" structure, they occupy a relatively small area that does not influence mixing. In the figure, the blue dominated region has two of the three "finger" structures in the bulk, and the other one is in the flowing layer (not visible from the bottom of the tumbler), with its edge extending into the bulk, just

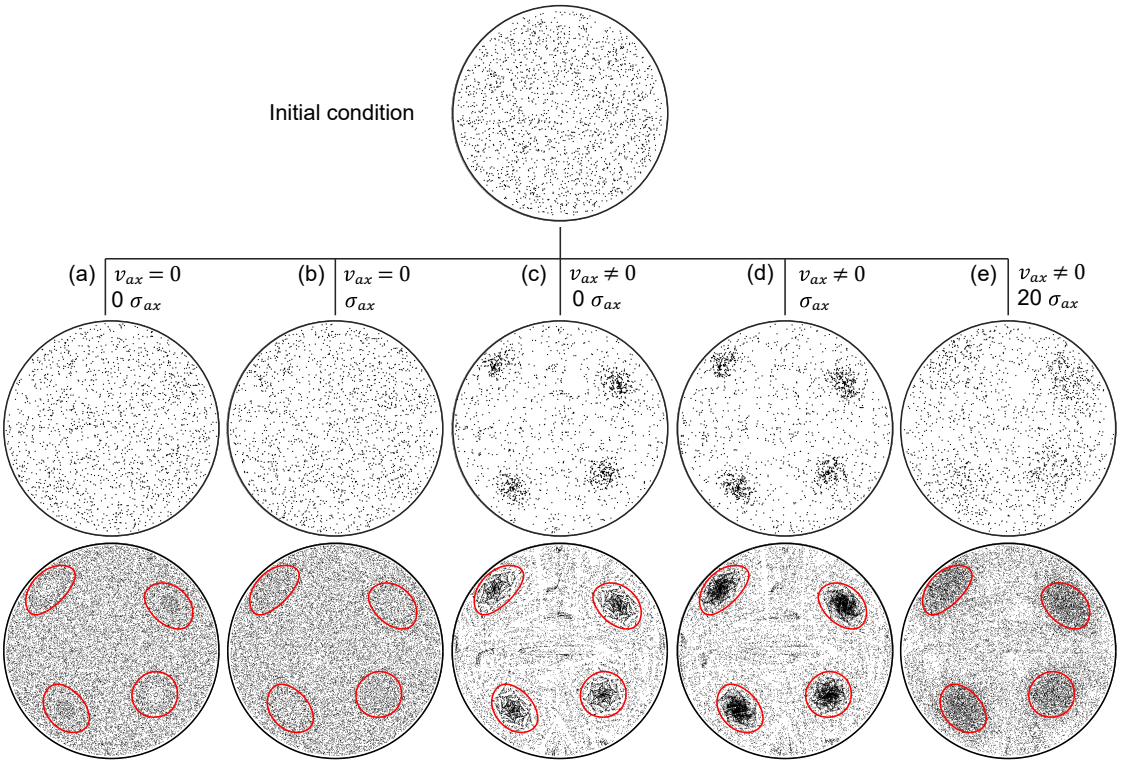

Figure 6.13. Continuum model simulation of $(90°, 90°)$ protocol: (a) without axial drift or diffusion; (b) random walk diffusion only; (c) with axial velocity but no diffusion; (d) with axial velocity and diffusion of σ_{ax}; (e) with axial velocity and diffusion of 20 σ_{ax}. (Top row) Initial random distribution of tracer points. (middle row) Tracer point distribution at $M = 30$ showing clustering in (c,d). (bottom row) Cumulative tracer point positions for $30 \leq M \leq 45$.

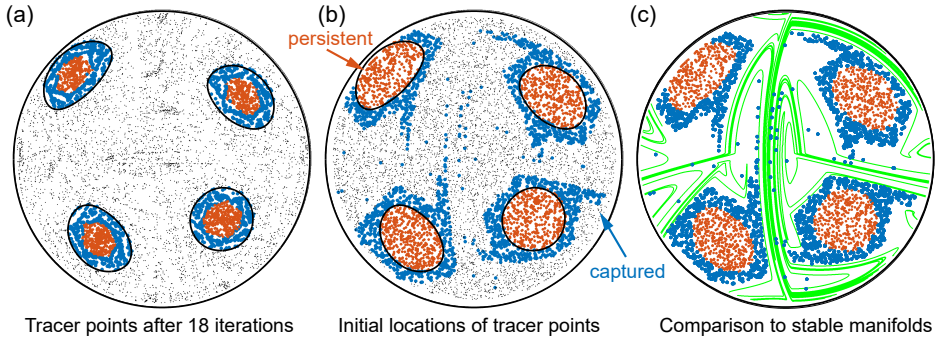

Figure 6.14. (a,b) Tracking tracer points through barriers to mixing over six periods of the $(90°, 90°)$ protocol for the modified continuum model with axial transport and no diffusion. Tracer points remain in (orange) or enter (blue) the non-mixing regions or stay in the chaotic region (small black dots). (c) Tracer points entering the non-mixing regions (blue) tend to follow the stable manifolds (green).

barely visible on the top and left periphery. Specifically, the red and blue dominated regions are separated by a boundary, a "leaky" barrier to mixing. This is a result of complicated interactions between the flowing layer and the underlying dynamical system related to the bi-axial protocol [78, 24, 173, 77] as well as invariant ergodic structures that result in barriers to mixing [95].

Figure 6.15(b) demonstrates how these barriers to mixing result in pattern formation for a mixture of 15% large (4 mm) blue particles and 85% small (2 mm) red particles in the DEM simulation. The initial condition in this DEM simulation is a tumbler filled to slightly less than half with small red particles and topped with a layer of large blue particles to fill the tumbler to half full, resulting in an overall fraction of 85% small particles and 15% large particles. The blue large particles in the initial configuration effectively correspond to the blue dominated flowing layer (one of the three "fingers") in the original continuum model [Fig. 6.15(a)]. At 30 iterations, these large particles occupy the entire blue dominated region as a result of diffusion and chaotic mixing in this region, with very few large particles in the small particle (red) dominated regions. Compared to the previous protocol examples of $(57°, 57°)$ and $(90°, 90°)$, where large particles migrate into periodic non-mixing islands from the chaotic region, here, large particles only infrequently cross the global mixing barrier and instead mainly disperse in the blue dominated region.

A comparison of the original continuum model with the modified continuum model for the $(45°, 45°)$ protocol demonstrates that there is a persistent global barrier to mixing, as shown in Figure 6.16. Similar to the initial condition in the DEM simulation [Fig. 6.15(b)], tracer points are initially distributed uniformly in the flowing layer only, corresponding to one of the three blue "fingers" in the continuum model. Note that this initial condition is different from that for the Poincaré map shown in Fig. 6.15(a) but the same for the DEM simulations in Fig. 6.15(b), with the primary purpose to illustrate the mixing barrier. In all cases with or without axial velocity and additional diffusion, the tracer points in Fig. 6.16 are

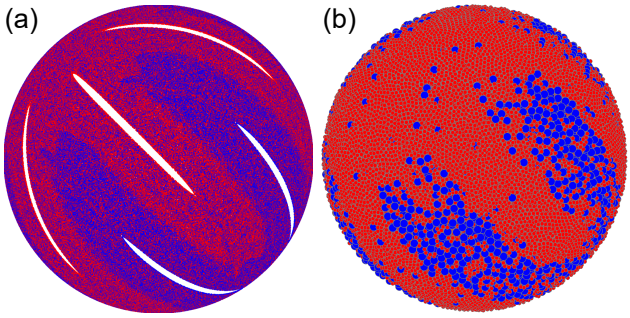

Figure 6.15. A mixing barrier spanning the tumbler exists for the $(45°, 45°)$ protocol (bottom view). (a) Poincaré section advected by the continuum model without axial velocity shows large interlocking finger-like structures. (b) Large blue particles remain primarily in the half of the domain they are initially placed in at $M = 30$ of a DEM simulation with 15% large blue particles and 85% small red particles.

mostly distributed in the blue dominated region with only a few crossing the mixing barrier. A higher level of diffusion only slightly increases density of tracer points in the red dominated region and blurs the boundary between the two regions [Figure 6.16(d,e)], but it does not alter the overall distribution of tracer points. The global mixing barrier is surprisingly persistent even with an axial velocity and a relatively high level of diffusion. There are two reasons that may explain this persistence. First, the global mixing barrier in this example wraps around two regions that are similarly chaotic themselves, while the barriers to mixing associated with the non-mixing islands in previous examples separate periodic regions from the chaotic region. Therefore, the global mixing barrier does not bound a sink under the influence of axial velocity as it does for the $(57°, 57°)$ and $(90°, 90°)$ protocols. Second, the direction of axial transport aligns with the tangent direction of the boundary between the red and blue dominated regions when it crosses the flowing layer so that axial transport redistributes large particles along the boundary with a much higher probability than across it.

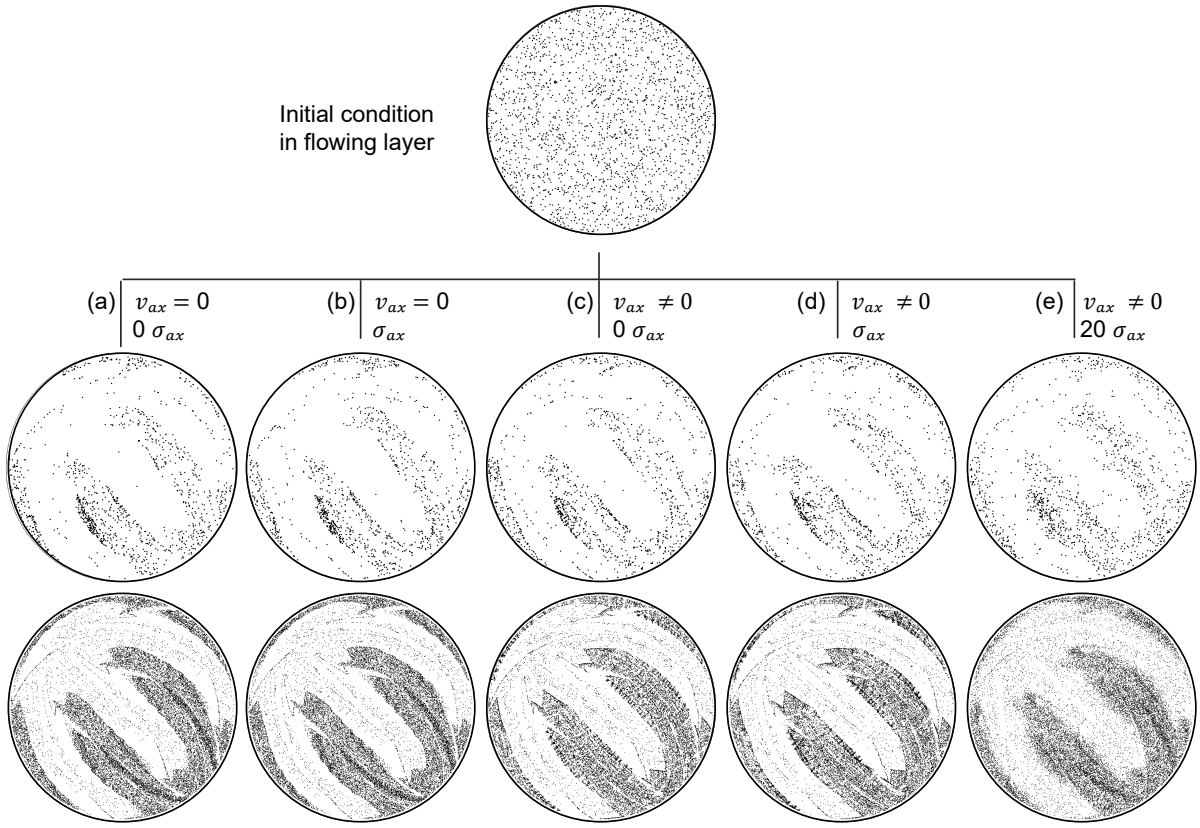

Figure 6.16. Continuum model simulation of $(45°, 45°)$ protocol: (a) without axial drift or diffusion; (b) random walk diffusion only; (c) with axial velocity but no diffusion; (d) with axial velocity and diffusion of σ_{ax}; (e) with axial velocity and diffusion of 20 σ_{ax}. (Top row) Initial random distribution of tracer points. (middle row) Tracer point distribution at $M = 30$. (bottom row) Cumulative tracer point positions for $30 < M < 45$. Tracer points only cross barriers to mixing occasionally in all cases.

6.3.6. Density segregation

Results up to this point describe the formation of segregation patterns driven by size differences. However, it is well-known that density differences for particles of the same size can also result in segregation. The question is do density-bidisperse mixtures in the BST system form patterns and, if so, are they similar to those for size-driven segregation. To achieve a similar propensity for segregation strength as in the size-bidisperse mixture, the density ratio $R_\rho = \rho_1/\rho_2$ between the two species needs to be fairly large $8 < R_\rho < 10$ [137, 168]. Two simulations are performed using equal diameter particles (2 mm) but with $R_\rho = 3$ (2

vol.% of $\rho_1 = 2000\,\mathrm{kg\,m^{-3}}$ and 98 vol.% of $\rho_2 = 6000\,\mathrm{kg\,m^{-3}}$) and $R_\rho = 8$ (2 vol.% of $\rho_1 = 1000\,\mathrm{kg\,m^{-3}}$ and 98 vol.% of $\rho_2 = 8000\,\mathrm{kg\,m^{-3}}$). In both cases, light particles segregate to the tumbler wall, similar to large particles in the size-bidisperse cases, but only a weak segregation pattern occurs for $R_\rho = 3$, and no significant pattern is evident for $R_\rho = 8$. This unexpected result is easily explained. For $R_\rho = 3$, the segregation is relatively weak, thereby explaining the weak pattern formation. Although the higher value of $R_\rho = 8$ produces stronger segregation of light particles to the tumbler wall, significant bouncing of light particles at the downstream end of the flowing layer occurs as they hit the downstream wall of the tumbler. As a result, the collisional diffusion disrupts the pattern formation. Thus, pattern formation can occur for density-bidisperse cases, but it is difficult to detect for small values of R_ρ because segregation is weak and disrupted by collisional diffusion at large values of R_ρ where segregation is stronger.

6.4. Discussion and conclusions

We previously showed that segregation patterns in size-bidisperse granular materials can form in a three-dimensional system via experiments and that these patterns can be predicted from the Poincaré map that depends on the details of the mixing protocol [173, 171]. However, the way in which the segregation of the two particle species interacts with the non-mixing regions evident in the Poincaré map, which inherently has no segregation information, was not evident. All that was understood was that the tumbler starts to rotate, randomly distributed large particles segregate to the free surface as they pass through the flowing layer and subsequently deposit near the tumbler wall into the fixed bed of particles in solid body rotations. At the same time, large particles gradually accumulate in non-mixing regions. It was also understood that large particle clusters do not expand further. Large particles leaving a particular cluster are, on average, balanced by other large particles entering the

cluster. However, the mechanism for the accumulation of the large particles into the non-mixing regions was unclear.

Here we have shown that axial transport is a necessary component for the accumulation of large particles in non-mixing regions. Evidence of this weak axial drift was provided by Zaman et al. for a spherical tumbler in single axis rotation [172]. Before the particles segregate, both small particles and large particles have the same probability to visit periodic non-mixing regions in the domain. However, as radial segregation takes place, large particles rise to the surface of the flowing layer. This has two consequences. First, this causes the large particles to deposit near the tumbler wall when they enter the fixed bed of particles. This is at the radius where the non-mixing regions are the largest [see Fig. 6.5 (c)]. Second, particles on the surface of the flowing layer drift axially into non-mixing islands. These two effects cause the large particles to preferentially accumulate in the non-mixing islands identified by the original continuum model. Small particles fall to lower levels of the flowing layer, and tend to reside beneath the large particle layer in the non-mixing regions. The segregation pattern can only be observed for concentration of large particles less than about 0.3. Otherwise, radial segregation causes the entire tumbler wall to be fully covered by large particles.

The tendency for accumulation of surface particles (large particles in this case) having a small axial drift toward the poles of the spherical tumbler can be predicted qualitatively using a continuum model incorporating the axial velocity measured from particles in the top layer of the flowing layer in DEM simulation. While the continuum model without axial drift predicts mixing barriers prohibiting material transport across the non-mixing boundaries, the modified continuum model not only predicts material transport through the boundaries, but also that the centers of these non-mixing regions act as sinks drawing material (specifically large particles at the surface of the flowing layer) into them. Note that the modified continuum model only accounts for flux near the free surface, neglecting flux

lower in the flowing layer. This approach predicts the segregation pattern because segregation causes the large particles to stay near the surface of the flowing layer and deposit close to the tumbler wall. If the material flow deeper in the flowing layer were to be tracked, it would balance that in the top layer. However, this flow consists mostly of small particles, which are lower in the flowing layer due to segregation, so it does not contribute to the segregation pattern visible at the wall of the tumbler. The axial drift, even though relatively small compared to streamwise flow, significantly changes the dynamical system features and is crucial to the segregation pattern formation.

A second category of non-mixing barriers exist that is different from those considered in detail in this chapter up until now [173, 171]. Instead of separating non-mixing from chaotic regions, these barriers separate different chaotic regions. Evidence of particles confined in regions separated by the barriers for a size-bidisperse system was reported, but was not previously understood. Here we show that these segregation structures are independent of any axial velocity. Instead, they appear to be a consequence of invariant ergodic subsets that have only recently been considered [95].

The appearance of segregation patterns in the biaxial spherical tumbler flow, which is one of the simplest 3D tumbler geometries that can be considered, suggests that analogous segregation patterns can occur in industrial mixers used in the pharmaceutical, chemical, and agricultural processing industries. In these cases, the goal is usually to avoid segregation and assure mixing, something that may be critical to the process. In an attempt to effectively mix granular components in industry, a variety of unusual tumbler geometries are used such as V-blenders, double-cone blenders [14], and dual-axis cylindrical tumblers [97, 99]. However, the results in this chapter suggest that using a 3D tumbler geometry does not assure mixing. In fact, the combined effects of the velocity field, which can result in barriers to mixing and non-mixing regions, can interact with segregation in surprising ways to frustrate attempts at mixing in 3D tumblers rather than assuring mixing.

CHAPTER 7

Summary and extensions

Mixing and segregation are two sides of the same coin. Their relationship is complex in granular systems because granular materials that differ in physical properties often inherently segregate when agitated. This dissertation draws upon past research in both mixing and segregation, and examines their interaction in a 3D granular flow system. Complex structures resulting from the flow dynamics and segregation are captured and analyzed from dynamical systems perspectives. The dynamical system approaches provide insight into understanding many aspects of the granular flow system. Key features include non-mixing regions, barriers to mixing, mixing regions that correspond to mixing efficacy of physical systems, and sinks that determine segregation patterns. At the same time, physical processes that are often thought to be of secondary importance, including diffusion and weak secondary velocities are shown to be critical in understanding and explaining the phenomena.

The research described in this dissertation starts with mixing in one of the simplest piecewise isometries that can be studied: the interval exchange transformation (IET) in which a line segment is cut into pieces and rearranged to reform the line segment (Chapter 3). While this system has been studied previously, the implications of the practical problem of accuracy in the position of iterative cuts of the line segment on mixing is addressed in my work for the first time. For permutation orders that are irreducible non-rotational, the variation in cut locations prevents reordering of material that leads to periodic behavior (non-mixing), thus improving mixing. However, the improvement decreases as the length ratio of the cuts becomes closer to irrational (i.e., having a longer continued fraction representation).

Compared to stretching-and-folding, cutting-and-shuffling produces comparable mixing at short times.

Motivated by a dynamical systems viewpoint of the IET and previous analysis of dynamical system features of continuum models of quasi-2D granular tumblers, a continuum model of the flow in the three-dimensional bi-axial spherical tumbler is devised in Chapter 4. This model builds upon the flow kinematics of the constant shear rate flow in the flowing layer and solid body rotation in the bulk. Using the continuum model, dynamical systems structures are found including non-mixing islands, barriers to mixing, and chaotic regions. The continuum model perspective not only captures the rearrangements of materials from the cutting-and-shuffling framework, but also the stretching in the flowing layer that is critical to mixing. Based on the features of non-mixing regions and barriers to mixing identified using the continuum model of the BST, the influence of these features on dynamics and mixing is examined in experiments. Observations based on x-ray flow visualization demonstrate that periodic regions serve as barriers to mixing by limiting particle movement within them, while chaotic regions promote mixing. In some cases, a global barrier to mixing matching that found in the continuum model results is observed as a result of interaction between stretching in the flowing layer and the underlying cutting-and-shuffling framework. The continuum approach provides an understanding of the physics by considering key elements including the flow dynamics, diffusion, and stretching in the flowing layer, while avoiding the burden of needing to resolve microscopic details. Segregation pattern formation was observed experimentally in the BST system is described in Chapter 5, where one species of particles preferentially accumulates in non-mixing regions predicted solely based on kinematics of the flow. In a size-bidisperse system, large particles accumulate into the non-mixing regions as a result of the radial segregation and flowing layer dynamics.

Chapter 6 builds upon this understanding of mixing dynamics to examine the interaction of mixing in 3D tumblers and segregation between species of granular particles. Using DEM

simulations, the 3D structures of the non-mixing regions are observed and found to be influenced by competition between radial segregation and diffusion. One of the critical components that drives large particles to accumulate in non-mixing islands is a weak axial velocity. Implementing the axial velocity field as a perturbation to the original continuum model demonstrates that non-mixing islands are transformed into "sinks," which correspond to accumulation of one of the particle species. Specifically, when large particles pass through the flowing layer on the free surface, they move axially toward the poles, and into the non-mixing regions. Hence, the non-mixing regions become sinks for large particles. This evidence not only demonstrates complex dynamics of interaction between mixing protocol and segregation of granular materials, but also suggests that even weak perturbation to a flow can be significant in determining long term system behaviors in other systems with nominal barriers to transport.

Although this dissertation has provided answers to and insights into many questions regarding mixing and segregation in the BST flow, there are aspects that can be explored further. Most examples of the mixing and non-mixing behaviors in this dissertation considers protocols that predict large non-mixing KAM islands. As demonstrated previously, axial transport, though small, can lead to segregation pattern formation. In that regard, there may also be pattern formation for protocols that do not show discernible structures from unperturbed continuum model description. The segregation pattern showns in Chapter 6 are for protocols with large non-mixing KAM islands located near the tumbler poles during passage through the flowing layer. It would be interesting to see if segregation patterns were suppressed when non-mixing KAM islands are located near the equator of rotation, since in that case, axial drift would not drive large particles into the islands.

There are many other possible directions for future studies. First, the influence of interaction between mixing and segregation on barriers to mixing was primarily studied in the periodic non-mixing regions and only briefly addressed with respect to the global barriers to

mixing. The global mixing barriers are described as emerging structures from the flowing layer in [173], but Lynn et al. have recently demonstrated their roots in the PWI in terms of invariant ergodic subsets [95]. With this new understanding of the origin and existence of global barriers in PWI, the study of how mixing barriers transform under the influence of combined mixing and segregation could be an interesting area for future inquiry. This dissertation shows that with weak perturbation, periodic regions change to "sinks." The nature of the transition deserves further exploration. Moreover, by understanding how and why periodic regions and "sinks" occur, predicting the segregation pattern where higher order periodic points exist may be possible.

The framework used here to describe the interaction of complex flow dynamics and segregation can be applied in other geometries. However, applying the framework to other geometries could be complicated. As a simple example, keep in mind that small particles accumulate in non-mixing regions in the quasi-2D geometry of a square tumbler while large particles accumulate in analogous non-mixing regions of the 3D BST geometry. Furthermore, the 3D segregation observed in the BST results from a weak axial velocity in an otherwise dominant velocity field down the surface of the material. In more complex geometries, the interaction between the complex flow dynamics and the segregation can be even more complicated. Nevertheless, the continuum modeling, experiments, and DEM simulation results in this dissertation provide a coherent physical explanation of the interaction between the stretched cutting-and-shuffling flow dynamics in a 3D system and granular segregation.

References

[1] POV-Ray, the persistence of vision raytracer. `http://www.povray.org/`, cited August 2020.

[2] D. Aldous and P. Diaconis. Shuffling cards and stopping times. *Am. Math. Mon.*, 93:333, 1986.

[3] I. S. Aranson and L. S. Tsimring. Dynamics of Axial Separation in Long Rotating Drums. *Phys. Rev. Lett.*, 82:4643–4646, 1999.

[4] I. S. Aranson and L. S. Tsimring. Patterns and collective behavior in granular media: Theoretical concepts. *Rev. Mod. Phys.*, 78:641–692, 2006.

[5] H. Aref. Stirring by chaotic advection. *J. Fluid Mech.*, 143:1–21, 1984.

[6] P. Ashwin. Elliptic behaviour in the sawtooth standard map. *Phys. Lett. A*, 232:409–416, 1997.

[7] P. Ashwin and A. Goetz. Invariant curves and explosion of periodic islands in systems of piecewise rotations. *SIAM J. Appl. Dyn. Syst.*, 4:437, 2005.

[8] P. Ashwin, M. Nicol, and N. Kirkby. Accleration of one dimensional mixing by discontinuous mappings. *Physica A*, 310:347–363, 2002.

[9] A. Avila and G. Forni. Weak mixing for interval exchange transformations and translation flows. *Ann. Math.*, 165:637–664, 2007.

[10] J. Berkovitz, R. Frigg, and F. Kronz. The ergodic hierarchy, randomness and Hamiltonian chaos. *Stud. Hist. Philos. M. P.*, 37:661–691, 2006.

[11] J. Boujlel, F. Pigeonneau, E. Gouillart, and P. Jop. Rate of chaotic mixing in localized flows. *Phys. Rev. Fluids*, 1:1–8, 2016.

[12] S. E. Boyer and D. Elliott. Thrust Systems. *AAPG Bull.*, 66:1196–1230, 1982.

[13] J. Bridgwater. Self-diffusion coefficients in deforming powders. *Powder Technol.*, 25:129–131, 1980.

[14] J. Bridgwater. Mixing of powders and granular materials by mechanical means - A perspective. *Particuology*, 10:397–427, 2012.

[15] E. Brown and H. M. Jaeger. Shear thickening in concentrated suspensions: Phenomenology, mechanisms and relations to jamming. *Rep. Prog. Phys.*, 77:046602, 2014.

[16] M. E. Buzzi. Piecewise isometries have zero topological entropy. *Ergod. Theor. Dyn. Syst.*, 21:1371–1377, 2001.

[17] F. Cantelaube and D. Bideau. Radial Segregation in a 2d Drum: An Experimental Analysis. *Europhys. Lett.*, 30:133, 1995.

[18] P. Chen, B. J. Lochman, J. M. Ottino, and R. M. Lueptow. Inversion of band patterns in spherical tumblers. *Phys. Rev. Lett.*, 102:148001, 2009.

[19] P. Chen, J. M. Ottino, and R. M. Lueptow. Subsurface granular flow in rotating tumblers: A detailed computational study. *Phys. Rev. E*, 78:1–12, 2008.

[20] P. Chen, J. M. Ottino, and R. M. Lueptow. Onset mechanism for granular axial band formation in rotating tumblers. *Phys. Rev. Lett.*, 104:188002, 2010.

[21] P. Chen, J. M. Ottino, and R. M. Lueptow. Granular axial band formation in rotating tumblers: a discrete element method study. *New J. Phys.*, 13:055021, 2011.
[22] K. Choo, M. W. Baker, T. C. A. Molteno, and S. W. Morris. Dynamics of granular segregation patterns in a long drum mixer. *Phys. Rev. E*, 58:6115–6123, 1998.
[23] I. C. Christov, R. M. Lueptow, and J. M. Ottino. Stretching and folding versus cutting and shuffling: An illustrated perspective on mixing and deformations of continua. *Am. J. Phys.*, 79:359–367, 2011.
[24] I. C. Christov, R. M. Lueptow, J. M. Ottino, and R. Sturman. A study in three-dimensional chaotic dynamics: Granular flow and transport in a bi-axial spherical tumbler. *SIAM J. Appl. Dyn. Syst.*, 13:901–943, 2014.
[25] I. C. Christov, J. M. Ottino, and R. M. Lueptow. Chaotic mixing via streamline jumping in quasi-two-dimensional tumbled granular flows. *Chaos*, 20:023102, 2010.
[26] I. C. Christov, J. M. Ottino, and R. M. Lueptow. From streamline jumping to strange eigenmodes: Bridging the Lagrangian and Eulerian pictures of the kinematics of mixing in granular flows. *Phys. Fluids*, 23, 2011.
[27] L. O. Chua and T. Lin. Chaos in digital filters. *IEEE T. Circuits Syst.*, 35:648, 1988.
[28] E. Clément, J. Rajchenbach, and J. Duran. Mixing of a Granular Material in a Bidimensional Rotating Drum. *Europhys. Lett.*, 30:7–12, 1995.
[29] J. C. Crocker and D. G. Grier. Methods of digital video microscopy for colloidal studies. *J. Colloid Interf. Sci.*, 179:298 – 310, 1996.
[30] P. A. Cundall and O. D. L. Strack. A discrete numerical model for granular assemblies. *Géotechnique*, 29:47–65, 1979.
[31] J. H. B. Deane. Piecewise isometries: Applications in engineering. *Meccanica*, 41:241–252, 2006.
[32] A. Dogangun, Z. Karaca, A. Durmus, H. Sezen, and M. Asce. Cause of damage and failures in silo structures. *J. Perform. Constr. Fac.*, 23:65–71, 2009.
[33] V. N. Dolgunin and A. A. Ukolov. Segregation modeling of particle rapid gravity flow. *Powder Technol.*, 83:95–103, 1995.
[34] U. D'Ortona, N. Thomas, and R. M. Lueptow. Influence of rough and smooth walls on macroscale granular segregation patterns. *Phys. Rev. E*, 93, 2016.
[35] J. Duran. *Sands, Powders, and Grains*. Springer, New York, 2000.
[36] C. M. Dury and G. H. Ristow. Radial segregation in a two-dimensional Rotating Drum. *J. Phys. II*, 7:737–745, 1997.
[37] C. M. Dury, G. H. Ristow, J. L. Moss, and M. Nakagawa. Boundary effects on the angle of repose in rotating cylinders. *Phys. Rev. E*, 57:4491–4497, 1998.
[38] T. Elperin and A. Vikhansky. Granular flow in a rotating cylindrical drum. *Europhys. Lett.*, 42:619–623, 1998.
[39] Y. Fan, Y. Boukerkour, T. Blanc, P. B. Umbanhowar, J. M. Ottino, and R. M. Lueptow. Stratification, segregation, and mixing of granular materials in quasi-two-dimensional bounded heaps. *Phys. Rev. E*, 86:051305, 2012.
[40] Y. Fan, K. V. Jacob, B. Freireich, and R. M. Lueptow. Segregation of granular materials in bounded heap flow: A review. *Powder Technol.*, 312:67–88, 2017.
[41] Y. Fan, C. P. Schlick, P. B. Umbanhowar, J. M. Ottino, and R. M. Lueptow. Modelling size segregation of granular materials: the roles of segregation , advection and diffusion. *J. Fluid Mech.*, 741:252–279, 2014.

[42] Y. Fan, P. B. Umbanhowar, J. M. Ottino, and R. M. Lueptow. Kinematics of monodisperse and bidisperse granular flows in quasi-two-dimensional bounded heaps. *Proc. R. Soc. A*, 469, 2013.
[43] G. Félix, V. Falk, and U. D'Ortona. Granular flows in a rotating drum: the scaling law between velocity and thickness of the flow. *Eur. Phys. J. E*, 22:25–31, 2007.
[44] S. J. Fiedor and J. M. Ottino. Mixing and segregation of granular matter: Multi-lobe formation in time-periodic flows. *J. Fluid Mech.*, 533:223–236, 2005.
[45] T. Finger, F. Von Rüling, S. Lévay, B. Szabó, T. Börzsönyi, and R. Stannarius. Segregation of granular mixtures in a spherical tumbler. *Phys. Rev. E*, 93:1–9, 2016.
[46] A. M. Fry, P. B. Umbanhowar, J. M. Ottino, and R. M. Lueptow. Diffusion, mixing, and segregation in confined granular flows. *AIChE J.*, 65:875–881, 2019.
[47] X. C. Fu and J. Duan. On global attractors for a class of nonhyperbolic piecewise affine maps. *Physica D*, 237:3369, 2008.
[48] O. S. Galaktionov, P. D. Anderson, G. W. M. Peters, and H. E. H. Meijer. Analysis and Optimization of Kenics Static Mixers. *Int. Polym. Proc.*, 18:138–50, 2003.
[49] J. F. Gilchrist and J. M. Ottino. Competition between chaos and order: mixing and segregation in a spherical tumbler. *Phys. Rev. E*, 68:061303, 2003.
[50] A. Goetz. Dynamics of a piecewise rotation. *Discrete Continu. Dynam. Syst.*, 4:593, 1998.
[51] A. Goetz. Dynamics of piecewise isometries. *Illinois J. Math.*, 44:465–478, 2000.
[52] A. Goetz. Stability of piecewise rotations and affine maps. *Nonlinearity*, 14:205, 2001.
[53] A. Goetz. Piecewise isometries - an emerging area of dynamical systems. In P. Grabner and W. Woess, editors, *Fractals in Graz 2001.Trends in Mathematics*, pages 135–144. Birkhäuser,Basel, 2003.
[54] A. Goetz and G. Poggiaspalla. Rotations by p/7. *Nonlinearity*, 17:1787, 2004.
[55] L. A. Golick and K. E. Daniels. Mixing and segregation rates in sheared granular materials. *Phys. Rev. E*, 80:1–4, 2009.
[56] J. Gollub. Continuum mechanics in physics education. *Phys. Today*, 56:10, 2003.
[57] J. M.N. T. Gray. Particle Segregation in Dense Granular Flows. *Annu. Rev. Fluid Mech.*, 50:407–33, 2018.
[58] J. M.N. T. Gray and C. Ancey. Multi-component particle-size segregation in shallow granular avalanches. *J. Fluid Mech.*, 678:535–588, 2011.
[59] P. K. Haff. Grain flow as a fluid-mechanical phenomenon. *J. Fluid Mech.*, 134:401–430, 1983.
[60] G. Haller and G. Yuan. Lagrangian coherent structures and mixing in two-dimensional turbulence. *Physica D*, 147:352–370, 2000.
[61] H. Haller. Rectangle exchange transformations. *Mh. Math.*, 91:215–232, 1981.
[62] H. Henein, J. K. Brimacombe, and A. P. Watkinson. Experimental study of transverse bed motion in rotary kilns. *Metall. Trans. B*, 14:191–205, 1983.
[63] J. M. Hertzsch, R. Sturman, and S. Wiggins. DNA microarrays: Design principles for maximizing ergodic, chaotic mixing. *Small*, 3:202–218, 2007.
[64] K. M. Hill, G. Gioia, D. Amaravadi, and C. Winter. Moon Patterns, Sun Patterns, and Wave Breaking in Rotating Granular Mixtures. *Complexity*, 10:79–86, 2005.
[65] K. M. Hill, N. Jain, and J. M. Ottino. Modes of granular segregation in a noncircular rotating cylinder. *Phys. Rev. E*, 64:4, 2001.

[66] K. M. Hill and J. Kakalios. Reversible axial segregation of binary mixtures of granular materials. *Phys. Rev. E*, 59, 1994.

[67] K. M. Hill, D. V. Khakhar, J. F. Gilchrist, J. J. McCarthy, and J. M. Ottino. Segregation-driven organization in chaotic granular flows. *Proc. Natl. Acad. Sci. USA*, 96:11701–11706, 1999.

[68] T. P. Hunt, D. Issadore, and R. M. Westervelt. Integrated circuit/microfluidic chip to programmably trap and move cells and droplets with dielectrophoresis. *Lab Chip*, 8:81–87, 2007.

[69] Austin B. Isner. *A quantitative study of size segregation in free surface granular flows.* PhD dissertation, Northwestern University, 2017.

[70] H. M. Jaeger, S. R. Nagel, and R. P. Behringer. Granular solids, liquids, and gases. *Rev. Mod. Phys.*, 68:1259–1273, 1996.

[71] N. Jain, J. M. Ottino, and R. M. Lueptow. An experimental study of the flowing granular layer in a rotating tumbler. *Phys. Fluids*, 14:572, 2002.

[72] N. Jain, J. M. Ottino, and R. M. Lueptow. Regimes of segregation and mixing in combined size and density granular systems: An experimental study. *Granul. Matter*, 7:69–81, 2005.

[73] A. Janda, D. Maza, A. Garcimartín, E. Kolb, J. Lanuza, and E. Clément. Unjamming a granular hopper by vibration. *Europhys. Lett.*, 87:24002, 2009.

[74] G. A. Jimenez and S. C. Jana. Electrically conductive polymer nanocomposites of polymethylmethacrylate and carbon nanofibers prepared by chaotic mixing. *Compos. Part A*, 38:983–993, 2007.

[75] R. P. Jones, A. B. Isner, H. Xiao, J. M. Ottino, P. B. Umbanhowar, and R. M. Lueptow. Asymmetric concentration dependence of segregation fluxes in granular flows. *Phys. Rev. Fluids*, 3:094304, 2018.

[76] S. W. Jones and H. Aref. Chaotic advection in pulsed source-sink systems. *Phys. Fluids*, 31:469, 1988.

[77] G. Juarez, I. C. Christov, J. M. Ottino, and R. M. Lueptow. Mixing by cutting and shuffling 3d granular flow in spherical tumblers. *Chem. Eng. Sci.*, 73:195 – 207, 2012.

[78] G. Juarez, R. M. Lueptow, J. M. Ottino, R. Sturman, and S. Wiggins. Mixing by cutting and shuffling. *Europhys. Lett.*, 91:20003, 2010.

[79] B. Kahng. Dynamics of symplectic piecewise affine elliptic rotation maps on tori. *Ergod. Theor. Dyn. Syst.*, 22:483–505, 2002.

[80] B. Kahng. Singularities of two-dimensional invertible piecewise isometric dynamics. *Chaos*, 19:023115, 2009.

[81] M. Keane. Interval exchange transformations. *Math. Z.*, 141:25–31, 1975.

[82] D. V. Khakhar, J. G. Franjione, and J. M. Ottino. A case study of chaotic mixing in deterministic flows : the partitioned-pipe mixer. *Chem. Eng. Sci.*, 42:2909–2926, 1987.

[83] D. V. Khakhar, J. J. McCarthy, J. F. Gilchrist, and J. M. Ottino. Chaotic mixing of granular materials in two-dimensional tumbling mixers. *Chaos*, 9:195–205, 1999.

[84] D. V. Khakhar, J. J. McCarthy, and J. M. Ottino. Radial segregation of ternary granular mixtures in rotating cylinders. *Phys. Fluids*, 9:3600, 1997.

[85] D. V. Khakhar, J. J. McCarthy, T. Shinbrot, and J. M. Ottino. Transverse flow and mixing of granular materials in a rotating cylinder. *Phys. Fluids*, 9:31–43, 1997.

[86] D. V. Khakhar, A. V. Orpe, P.D. Anderson, and J. M. Ottino. Surface flow of granular materials: model and experiments in heap formation. *J. Fluid Mech.*, 441:255–264,

2001.

[87] D. V. Khakhar, H. Rising, and J. M. Ottino. Foundations of chaotic mixing. *J. Fluid Mech.*, 172:419–451, 1986.

[88] A. Ya. Khinchine. *Continued fractions*. P. Noordhoff, Groningen, 1963.

[89] M. K. Krotter, I. C. Christov, J. M. Ottino, and R. M. Lueptow. Cutting and shuffling a line segment: mixing by interval exchange Transformations. *Int. J. Bifurcat. Chaos*, 22:1230041, 2012.

[90] A. Kudrolli. Size separation in vibrated granular matter. *Rep. Prog. Phys.*, 67:209–247, 2004.

[91] H. A. Kusch and J. M. Ottino. Experiments on mixing in continuous chaotic flows. *J. Fluid Mech.*, 236:319–348, 1992.

[92] H. Li and J. J. McCarthy. Phase diagrams for cohesive particle mixing and segregation. *Phys. Rev. E*, 71:021305, 2005.

[93] D. V. Louzguine-Luzgin, L. V. Louzguina-Luzgina, and A. Y. Churyumov. Mechanical properties and deformation behavior of bulk metallic glasses. *Metals-Basel*, 3:1–22, 2013.

[94] T. F. Lynn, J. M. Ottino, and P. B. Umbanhowar. Cutting and shuffling a hemisphere: Nonorthogonal axes. *Phys. Rev. E*, 99:032204, 2019.

[95] T. F. Lynn, J. M. Ottino, P. B. Umbanhowar, and R. M. Lueptow. Identifying invariant ergodic subsets and barriers to mixing by cutting and shuffling: Study in a birotated hemisphere. *Phys. Rev. E*, 101:012204, 2020.

[96] H. A. Makse. Continuous avalanche segregation of granular mixtures in thin rotating drums. *Phys. Rev. Lett.*, 83:3186–3189, 1999.

[97] M. Marigo, M. Davies, T. Leadbeater, D. L. Cairns, A. Ingram, and E. H. Stitt. Application of positron emission particle tracking (PEPT) to validate a discrete element method (DEM) model of granular flow and mixing in the Turbula mixer. *Int. J. Pharm.*, 446:46–58, 2013.

[98] G. Mathew, I. Mezić, and L. Petzold. A multiscale measure for mixing. *Physica D*, 211:23–46, 2005.

[99] C. Mayer-Laigle, C. Gatumel, and H. Berthiaux. Mixing dynamics for easy flowing powders in a lab scale Turbula® mixer. *Chem. Eng. Res. Des.*, 95:248–261, 2015.

[100] S. W. Meier, S. E. Cisar, R. M. Lueptow, and J. M. Ottino. Capturing patterns and symmetries in chaotic granular flow. *Phys. Rev. E*, 74:1–11, 2006.

[101] S. W. Meier, R. M. Lueptow, and J. M. Ottino. A dynamical systems approach to mixing and segregation of granular materials in tumblers. *Adv. Phys.*, 56:757–827, 2007.

[102] J. Mellmann. The transverse motion of solids in rotating cylinders-forms of motion and transition behavior. *Powder Technol.*, 118:251–270, 2001.

[103] M. Mendes and M. Nicol. Periodicity and recurrence in piecewise rotations of euclidean spaces. *Int. J. Bifurcat. Chaos*, 12:2353–2361, 2004.

[104] G. Metcalfe and D. Lester. Mixing and heat transfer of highly viscous food products with a continuous chaotic duct flow. *J. Food Eng.*, 95:21–29, 2009.

[105] N. R. Moharana, M. F. M. Speetjens, R. R. Trieling, and H. J. H. Clercx. Three-dimensional Lagrangian transport phenomena in unsteady laminar flows driven by a rotating sphere. *Phys. Fluids*, 25, 2013.

[106] J. Moser. *Stable and Random Motions in Dynamical Systems*. Princeton University Press, Princeton, 1973.
[107] P. Mullowney, K. Julien, and J.D. Meiss. Blinking rolls: Chaotic advection in a three-dimensional flow with an invariant. *SIAM J. Appl. Dyn. Syst.*, 4:159–186, 2005.
[108] F. J. Muzzio, T. Shinbrot, and B. J. Glasser. Powder technology in the pharmaceutical industry: the need to catch up fast. *Powder Technol.*, 124:1–7, 2002.
[109] L. Naji and R. Stannarius. Axial and radial segregation of granular mixtures in a rotating spherical container. *Phys. Rev. E*, 79:1–8, 2009.
[110] N. Nityanand, B. Manley, and H. Henein. An analysis of radial segregation for different sized spherical solids in rotary cylinders. *Metall. Trans. B*, 17:247–257, 1986.
[111] P. D. Olmsted. Perspectives on shear banding in complex fluids. *Rheol. Acta*, 47:283–300, 2008.
[112] A. V. Orpe and D. V. Khakhar. Scaling relations for granular flow in quasi-two-dimensional rotating cylinders. *Phys. Rev. E*, 64:13, 2001.
[113] J. M. Ottino. *The Kinematics of mixing: Stretching, chaos, and transport*. Cambridge University Press, Cambridge, 1989.
[114] J. M. Ottino. The mixing of fluids. *Sci. Am.*, 260:56–67, 1989.
[115] J. M. Ottino. Mixing, chaotic Advection, and rurbulence. *Annu. Rev. Fluid Mech.*, 22:207–53, 1990.
[116] J. M. Ottino and D. V. Khakhar. Mixing and segregation of granular materials. *Annu. Rev. Fluid Mech.*, 32:55–91, 2000.
[117] J. M. Ottino and D. V. Khakhar. Mixing and segregation of granular materials. *Annu. Rev. Fluid Mech.*, 32:55–91, 2000.
[118] J. M. Ottino, C. W. Leong, H. Rising, and P. D. Swanson. Morphological structures produced by mixing in chaotic flows. *Nature*, 333:419–425, 1988.
[119] J. M. Ottino, W. E. Ranz, and C. W. Macosko. A lamellar model for analysis of liquid-liquid mixing. *Chem. Eng. Sci.*, 34:877–890, 1979.
[120] J. M. Ottino and S. Wiggins. Introduction: Mixing in microfluidics. *Philos. T. Roy. Soc. A*, 362:923–935, 2004.
[121] P. P. Park, T. F. Lynn, P. B. Umbanhowar, J. M. Ottino, and R. M. Lueptow. Mixing and the fractal geometry of piecewise isometries. *Phys. Rev. E*, 95:042208, 2017.
[122] P. P. Park, P. B. Umbanhowar, J. M. Ottino, and R. M. Lueptow. Mixing with piecewise isometries on a hemispherical shell. *Chaos*, 26:073115, 2016.
[123] E. L. Paul, V. A. Atiemo-Obeng, and S. M. Kresta. *Handbook of industrial mixing: Science and practice*. John Wiley & Sons, Inc., 2004.
[124] D. Perugini, G. Poli, and R. Mazzuoli. Chaotic advection, fractals and diffusion during mixing of magmas: evidence from lava flows. *J. Volcanol. Geoth. Res.*, 124:255–279, 2003.
[125] R. T. Pierrehumbert. Large-scale horizontal mixing in planetary atmospheres. *Phys. Fluids A*, 3:1250, 1991.
[126] S. M. Pizer, E. P. Amburn, J. D. Austin, R. Cromartie, A. Geselowitz, T. Greer, B. ter Haar Romeny, J. B. Zimmerman, and K. Zuiderveld. Adaptive histogram equalization and its variations. *Comput. Vision Graph.*, 39:355–368, 1987.
[127] N. A. Pohlman, S. W. Meier, R. M. Lueptow, and J. M. Ottino. Surface velocity in three-dimensional granular tumblers. *J. Fluid Mech.*, 560:355, 2006.

[128] N. A. Pohlman, J. M. Ottino, and R. M. Lueptow. End-wall effects in granular tumblers: From quasi-two-dimensional flow to three-dimensional flow. *Phys. Rev. E*, 74:1–13, 2006.

[129] N. A. Pohlman, B. L. Severson, J. M. Ottino, and R. M. Lueptow. Surface roughness effects in granular matter: Influence on angle of repose and the absence of segregation. *Phys. Rev. E*, 73:1–9, 2006.

[130] Z. Pouransari, M. F. M. Speetjens, and H. J. H. Clercx. Formation of coherent structures by fluid inertia in three-dimensional laminar flows. *J. Fluid Mech.*, 654:5–34, 2010.

[131] S. V. Prants. Dynamical systems theory methods to study mixing and transport in the ocean. *Phys. Scripta*, 87:38115, 2013.

[132] J. Rajchenbach. Flow in powders: From discrete avalanches to continuous regime. *Phys. Rev. Lett.*, 65:2221–2225, 1990.

[133] G. H. Ristow. *Pattern Formation in Granular Materials*. Springer, Berlin Heidelberg, 2000.

[134] A. Rosato, K. J. Strandburg, F. Prinz, and R. H. Swendsen. Why the Brazil nuts are on top: Size segregation of particulate matter by shaking. *Phys. Rev. Lett.*, 58:1038–1040, 1987.

[135] S. B. Savage and C. K. K. Lun. Particle size segregation in inclined chute flow of dry cohesionless granular solids. *J. Fluid Mech.*, 189:311–335, 1988.

[136] C. P. Schlick, I. C. Christov, P. B. Umbanhowar, J. M. Ottino, and R. M. Lueptow. A mapping method for distributive mixing with diffusion: Interplay between chaos and diffusion in time-periodic sine flow. *Phys. Fluids*, 25:052102, 2013.

[137] C. P. Schlick, Y. Fan, A. B. Isner, P. B. Umbanhowar, J. M. Ottino, and R. M. Lueptow. Modeling segregation of bidisperse granular materials using physical control Parameters in the Quasi-2D Bounded Heap. *AIChE J.*, 61:1524–1534, 2015.

[138] C. P. Schlick, Y. Fan, P. B. Umbanhowar, J. M. Ottino, and R. M. Lueptow. Granular segregation in circular tumblers: theoretical model and scaling laws. *J. Fluid Mech.*, 765:632–652, 2015.

[139] C. P. Schlick, A. B. Isner, B. J. Freireich, Y. Fan, P. B. Umbanhowar, J. M. Ottino, and R. M. Lueptow. A continuum approach for predicting segregation in flowing polydisperse granular materials. *J. Fluid Mech.*, 797:95–109, 2016.

[140] A. Schultz, I. Papautsky, and J. Heikenfeld. Investigation of laplace barriers for arrayed electrowetting lab-on-a-chip. *Langmuir*, 30:5349–5356, 2014.

[141] A. Scott. Hamiltonian mappings and circle packing phase spaces: Numerical investigations. *Physica D*, 181:45, 2003.

[142] A. Scott, C. Holmes, and G. Milburn. Hamiltonian mappings and circle packing phase spaces. *Physica D*, 155:34–50, 2001.

[143] J. Shäfer, S. Dippel, and D. Wolf. Force schemes in simulations of granular materials. *J. Phys. I.*, 6:5–20, 1996.

[144] L. E. Silbert, G. S. Grest, R. Brewster, and A. J. Levine. Rheology and contact lifetimes in dense granular flows. *Phys. Rev. Lett.*, 99:1–4, 2007.

[145] L. D. Smith, P. P. Park, P. B. Umbanhowar, J. M. Ottino, and R. M. Lueptow. Predicting mixing via resonances: Application to spherical piecewise isometries. *Phys. Rev. E*, 95:062210, 2017.

[146] L. D. Smith, M. Rudman, D. R. Lester, and G. Metcalfe. Bifurcations and degenerate periodic points in a three dimensional chaotic fluid flow. *Chaos*, 26:053106, 2016.
[147] L. D. Smith, M. Rudman, D. R. Lester, and G. Metcalfe. Mixing of discontinuously deforming media. *Chaos*, 26:023113, 2016.
[148] L. D. Smith, M. Rudman, D. R. Lester, and G. Metcalfe. Localized shear generates three-dimensional transport. *Chaos*, 27, 2017.
[149] L. D. Smith, P. B. Umbanhowar, J. M. Ottino, and R. M. Lueptow. Mixing and transport from combined stretching-and-folding and cutting-and-shuffling. *Phys. Rev. E*, 96:042213, 2017.
[150] J. P. Snyder. Map projections: A working manual. Technical report, 1987.
[151] H. A. Stone, A. D. Stroock, and A. Ajdari. Engineering flows in small devices. *Annu. Rev. Fluid Mech.*, 36:381–411, 2004.
[152] S.H. Strogatz. *Nonlinear Dynamics and Chaos: With Applications to Physics, Biology, Chemistry, and Engineering*. Studies in Nonlinearity. CRC Press, 2nd edition, 2014.
[153] R. Sturman. The role of discontinuities in mixing. *Adv. Appl. Mech.*, 45:51–90, 2012.
[154] R. Sturman, S. W. Meier, J. M. Ottino, and S. Wiggins. Linked twist map formalism in two and three dimensions applied to mixing in tumbled granular flows. *J. Fluid Mech.*, 602:129–174, 2008.
[155] R. Sturman, J. M. Ottino, and S. Wiggins. *The Mathematical Foundations of Mixing: The Linked Twist Map as a Paradigm in Applications Micro to Macro, Fluids to Solids*. Cambridge University Press, 2006.
[156] J. Tang and R. P. Behringer. How granular materials jam in a hopper. *Chaos*, 21:041107, 2011.
[157] L. N. Trefethen and L. M. Trefethen. How many shuffles to randomize a deck of cards? *Proc. R. Soc. Lon. A*, 456:2561, 2000.
[158] A. Tsuda, R. A. Rogers, P. E. Hydon, and J. P. Butler. Chaotic mixing deep in the lung. *Proc. Natl. Acad. Sci. USA*, 99:10173–10178, 2002.
[159] P. B. Umbanhowar, R. M. Lueptow, and J. M. Ottino. Modeling segregation in granular flows. *Annu. Rev. Chem. Biomol. Eng.*, 10:129–53, 2019.
[160] G. S. Upadhyaya. *Powder Metallurgy Technology*. Cambridge International Science Publishing, Cambridge, 1997.
[161] B. Utter and R. P. Behringer. Self-diffusion in dense granular shear flows. *Phys. Rev. E*, 69:031308, 2004.
[162] M. Viana. Ergodic Theory of Interval Exchange Maps. *Rev. Mat. Complut.*, 19:7–100, 2006.
[163] F. R. Villatoro. La fisica de la loteria de Navidad. `http://francis.naukas.com/2015/12/22/la-fisica-de-la-loteria-de-navidad/`, 2015. Accessed: 2018-01-03.
[164] L. Wan, T.-T. Wong, and C.-S. Leung. Isocube : Exploiting the cubemap dardware. *IEEE T. Vis. Comput. Gr.*, 13:720–731, 2007.
[165] S. Wiggins. The dynamical systems approach to lagrangian transport in oceanic flows. *Annu. Rev. Fluid Mech.*, 37:295–328, 2005.
[166] S. Wiggins. Coherent structures and chaotic advection in three dimensions. *J. Fluid Mech.*, 654:1–4, 2010.
[167] S. Wiggins and J. M. Ottino. Foundations of chaotic mixing. *Philos. T. R. Soc. A*, 362:937–970, 2004.

[168] H. Xiao, P. B. Umbanhowar, M. J. Ottino, and R. M. Lueptow. Modelling density segregation in flowing bidisperse granular materials. *Proc. R. Soc. A*, 472:20150856, 2016.

[169] K. Yamane, M. Nakagawa, S. A. Altobelli, T. Tanaka, and Y. Tsuji. Steady particulate flows in a horizontal rotating cylinder. *Phys. Fluids*, 10:1419–1427, 1998.

[170] M. Yu, P. B. Umbanhowar, J. M. Ottino, and R. M. Lueptow. Cutting and shuffling of a line segment: Effect of variation in cut location. *Int. J. Bifurc. Chaos*, 26:1630038, 2016.

[171] M. Yu, P. B. Umbanhowar, J. M. Ottino, and R. M. Lueptow. Pattern formation in a fully three-dimensional segregating granular flow. *Phys. Rev. E*, 99:062905, 2019.

[172] Z. Zaman, U. D'Ortona, P. B. Umbanhowar, J. M. Ottino, and R. M. Lueptow. Slow axial drift in three-dimensional granular tumbler flow. *Phys. Rev. E*, 88:012208, 2013.

[173] Z. Zaman, M. Yu, P. P. Park, J. M. Ottino, R. M. Lueptow, and P. B. Umbanhowar. Persistent structures in a three-dimensional dynamical system with flowing and non-flowing regions. *Nat. Commun.*, 9:3122, 2018.

[174] Zafir Zaman. *An Experimental Study of Mixing Dynamics in 3D Granular Flows*. PhD dissertation, Northwestern University, 2016.

[175] R. Zhao and C. W. Macosko. Slip at polymer-polymer interfaces: Rheological measurements on coextruded multilayers. *J. Rheol.*, 46:145–167, 2002.

[176] O. Zik, D. Levine, S. G. Lipson, S. Shtrikman, and J. Stavans. Rotationally induced segregation of granular materials. *Phys. Rev. Lett.*, 73:644, 1994.

[177] K. Zuiderveld. Contrast limited adaptive histogram equalization. In P. Heckbert, editor, *Graphics Gems IV*, pages 474–485. Academic Press, 1994.

[178] D. A. Zumbrunnen and S. Inamdar. Novel sub-micron highly multilayered polymer films formed by continuous flow chaotic mixing. *Chem. Eng. Sci.*, 56:3893, 2001.

[179] I. Zuriguel, J. M. N. T. Gray, J. Peixinho, and T. Mullin. Pattern selection by a granular wave in a rotating drum. *Phys. Rev. E*, 73:71–74, 2006.

APPENDIX A

Realization of cutting-and-shuffling a line segment

(1) The subsegment lengths L_i are calculated by raising r to the $(i-1)$ power and normalized by the sum of total length:

$$L_i = \frac{r^{i-1}}{\sum_{j=1}^{N} r^{j-1}}$$

.

(2) The line segment extends from $x = 0$ to $x = 1$. A 1D array records the positions of all of the right side boundaries of subsegments, meaning all interfaces and the right boundary of the line segment ($x = 1$), so the number of elements in the interface array is N. The position of the i^{th} interface x_i on the right of the i^{th} subsegment is the cumulative sum of subsegment lengths from the left boundary ($x = 0$) to the interface. For $1 \leq i \leq N$,

$$x_i = \sum_{k=1}^{i} L_k.$$

Note that the position of the last interface (x_N) is the right boundary $x = 1$, since it is just the sum of all subsegment lengths. Thus, the array $[x_1 x_2 \ldots x_N]$ contains the "exact" cut locations and also represents the initial configuration for the multicomponent initial condition. For the protocol ($N = 4$, and $r = 1.5$) in Fig. 3.1(a), the interface array is [0.1231 0.3077 0.5846 1].

In contrast, the interface array of the two component initial condition in Fig. 3.9 is [0.5 1], which does not depends on the cut locations. However the "exact" cut location array for the two component case is still [0.1231 0.3077 0.5846 1] if the same N and r are used.

(3) A 1D array records integer numbers denoting the component (color) of the interval on the left of each interface. For a multicomponent initial condition (Fig. 3.1(a)), the component array is just [1 2 3 4]. The two component initial condition only has two components so the component array is just [1 2].

(4) In each iteration, a new array of cut locations is generated if $\sigma > 0$. σ must be smaller than x_1, the shortest subsegment length. Variations are generated by *randn* times σ as a (1 by $N-1$) array. Effectively, only $N-1$ cuts are performed so the last element of the cut location array is always 1. Then the perturbed cut locations are obtained by adding variations to the array of "exact" cut locations. Now the cut location array becomes

$$x_i^{cut} = \sum_{k=1}^{i} L_k + \sigma \cdot randn.$$

If the positions of the cuts overlap or exceed [0 1] boundaries, a new set of variation is generated until the cuts are in the right sequence and contained in [0 1].

(5) When the line segment is *cut*, all interfaces including the new cuts are obtained by taking the union of the interface array (the initial condition or the output from previous iteration) and the cut location array. The output position of all the interfaces is then determined by adding an offset ($x_{\Pi(i)}^{cut} - x_i^{cut}$) to the interfaces inside the i^{th} subsegment. This procedure is repeated for $i = 1, 2, \ldots, N$ to complete the *shuffling*.

(6) Meanwhile, the component array is also transformed accordingly. When a new interface is introduced by a cut, the element denoting the interval is copied. Then the elements in each subsegment are moved simultaneously with the interface array to the same output positions, so that component array match the interface array.

(7) After shuffling, if two consecutive elements are the same in the component array, meaning two intervals of the same component contact at an interface, one element is deleted in the component array, and the interface is deleted in the interface array.

(8) The longest component interval length U_n is determined by finding the maximum of interval lengths between interfaces. The number of interfaces C_n is the number of elements in the component array minus one.

(9) Steps (4)-(8) are repeated for n iterations to reach the final configuration. The outputs are an array of interfaces and the component array for the corresponding intervals.

APPENDIX B

Experiments with x-ray imaging

The x-ray imaging system consists of an x-ray source, the tumbling apparatus, and image detection equipments. The x-ray source (Spellman XRB80N100/10000) operates a cone shape beam with 25° open angle, which is suitable for viewing a spherical tumbler with a circular projection. For image detection, an x-ray image intensifier (Thales TH9428 HP2) and a high speed camera (Point Grey Blackfly BFLY-PGE-12A2M) are housed in the cabinet on the bottom. The system is connected with a lab computer for automated control and image storage. The x-ray equipment is described in detail elsewhere [174].

Particle tracking of a single x-ray opaque tracer particle in Chapter 4 is performed using $d = 1.89 \pm 0.09\,\mathrm{mm}$ diameter soda-lime glass beads (SiLiglit Deco Beads, Sigmund Lindner GmbH, Germany) in a half-filled $D = 14\,\mathrm{cm}$ diameter acrylic spherical tumbler. A density-matched ($\rho = 2.5\,\mathrm{g\,cm^{-1}}$) $d_{\mathrm{tracer}} = 4\,\mathrm{mm}$ diameter x-ray opaque tracer particle constructed from two 3D-printed plastic hemispherical shells with a Pb-Sn solder sphere in the center was used to visualize the flow. The larger diameter of the tracer particle caused the particle to flow at the surface of the flowing layer and near the tumbler wall in the solid bed. Components of the spherical tumbler apparatus within the x-ray beam path consist of x-ray transparent materials (aluminum and plastic) to ensure an image suitable for particle tracking.

For each rotation about the z-axis and the x-axis of the BST protocol, the sphere was rotated about a single axis for protocol angle (θ_z or θ_x) by three wheels driven by a motor mounted on a turntable at rotation speed $\omega = 2.6\,\mathrm{rpm}$, see Fig. B.1. Since an initially static particle bed only starts to flow when tilted beyond its static angle of repose β_s with respect

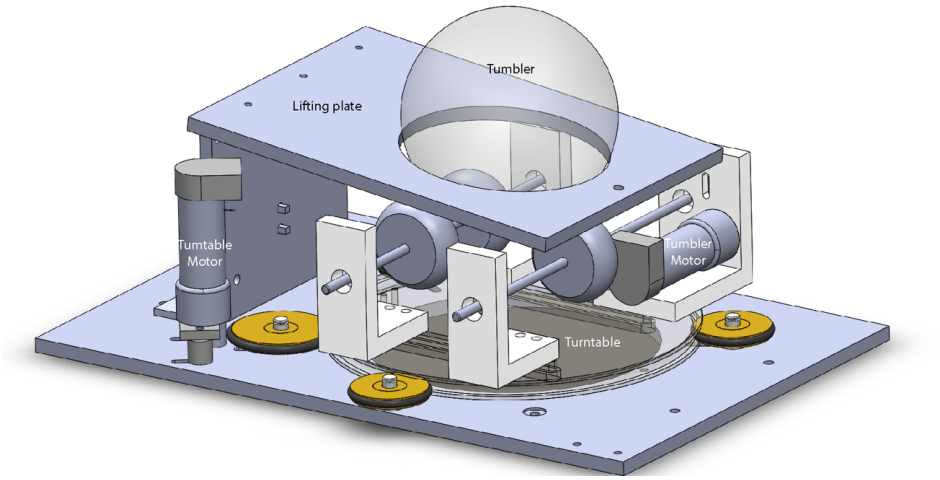

Figure B.1. Tumbling apparatus consisting of a spherical tumbler driven by three wheels mounted on a turntable that can orient the wheels to perform bi-axial protocols. A lifting plate lifts the tumbler off the wheels when changing the rotation axis. Reprinted from Zaman et al. [173] with permission ©2018 with permission of Springer Nature.

to the horizontal, the sphere was slowly rotated so that the free surface was just below β_s prior to each action. Then, when a protocol action (rotation) was initiated, there was a small avalanche at the start of flow as the free surface relaxed to the dynamic angle of repose $\beta < \beta_s$, after which the flow was continuous. After each action, the tumbler was rotated in the reverse direction to ensure the free surface was horizontal before switching the rotation axis. The apparatus reoriented the drive wheels for the next rotation by raising the tumbler off the wheels, rotating the turntable to make the wheel axes parallel to the next tumbling axis, and then lowering the tumbler back down onto the wheels. To minimize accumulated error from executing the protocol over many iterations, a position sensor was used to ensure that the turntable returned to the original axis after each iteration. Additionally, a thin X-ray opaque fiducial marker (lead tape) was mounted on the interior wall of the spherical tumbler to track any tumbling deviations. With these measures in place, the system has an angular displacement error of less than 1° per protocol iteration. The errors are not systematic and, hence, average to zero.

Images were acquired prior to each tumbling action: the first frame, when the free surface was horizontal and subsequent frames while the tumbler was slowly rotating to the angle of repose. The direction and magnitude of tracer particle displacement in these frames identified whether the particle was at the free surface or in the bulk near the tumbler wall. Image distortion due to image intensifier and camera optics was corrected using the MATLAB Image Processing Toolbox function `imwarp`. The geometric transformation required by the function `imwarp` was a 4th order polynomial model generated from applying the function `fitgeotrans` to an image obtained from a Cartesian hole pattern (diameter 3.5 mm with 5.1 mm spacing). The corrected hole pattern image was used to generate the matrix transformation from the hole pattern's pixel spacing to the physical grid dimensions. To track the tracer particle and the fiducial indicator, each image was divided by a background image generated from the average of all iterations from a particular run to reveal the two features of interest. The tracer particle and the fiducial indicator were distinguishable from each other by their eccentricity and were tracked automatically using 2D feature finding MATLAB algorithms developed by the Kilfoil group [1] using methods from Crocker et al. [29].

[1]Code repository hosted at `http://people.umass.edu/kilfoil/tools.php`

APPENDIX C

The continuum model and modification with axial velocity

The continuum model [101, 24] assumes that the flow is primarily two-dimensional in the streamwise direction and confined to a thin lenticular flowing layer with a constant depthwise shear rate $\dot{\gamma}$ for each rotation about the z-axis and the x-axis. Using a Cartesian coordinate system with origin at the center of the radius R_o spherical tumbler, rotation is clockwise about the z-axis and x-axis at a rotation speed ω for an angular displacement θ_z and θ_x, respectively. For convenience, all variables are dimensionless—length scales (x, y, z, r, and flowing layer depth δ) are normalized by R_o and rotation period T is normalized by $1/\omega$. The interface between the flowing layer and the bulk is given by $\delta(x,z) = \epsilon\sqrt{1-x^2-z^2}$, where $\epsilon = \sqrt{\omega/\dot{\gamma}}$ is the maximal dimensionless flowing layer depth (at the center $x = z = 0$). The shape of the flowing layer is formulated based on several assumptions. First, the flow adjusts instantaneous to the flowing layer length [101], so that the flow is steady and time dependence of surface velocity is neglected. Second, the surface velocity is maximum at the middle of the flowing layer where the flowing layer thickness is also maximum. This leads to a constant shear rate regardless of streamwise position. For a spherical tumbler, this flowing layer shape offers computation efficiency and relatively accurate description of flow in experiment. The velocity $\mathbf{u} = (u, v, w)$ is piecewise defined for the flowing layer and the bulk. For rotation about the z-axis, the flowing layer ($y \geq -\delta$) velocity is $\mathbf{u}_{\mathrm{fl}} = ((\delta+y)/\epsilon^2, xy/\delta, 0)$ and the bulk ($y < -\delta$) is in solid body rotation with velocity profile $\mathbf{u}_{\mathrm{b}} = (y, -x, 0)$. The assumption of no axial flow and incompressibility also allows the flow to be described with a stream function $\psi_{fl} = \frac{1}{\epsilon_z^2}\left[\delta_z(x,z)y + \frac{1}{2}y^2\right]$ for $y > -\delta_z(x,z)$ in the flowing layer, and $\psi_b = \frac{1}{2}(x^2+y^2)$

for solid body rotation in the fixed bed. Analogously, the velocity field for the x-axis action is obtained by interchanging x- and z-components.

In each single axis rotation about the z-axis and the x-axis, the ordinary differential equations consist an integrable dynamical system [155]. Thus, tracer trajectories can be solved directly given initial conditions. Moreover, because the flow is piecewise defined, the ordinary differential equations can be solved for alternate rotation actions. Tracer positions are calculated based on the analytical solutions given by Christov et al. [24]. A flowing layer depth at the midpoint of the flowing layer, $\delta(0,0)$, of $\epsilon = 0.15$ matches the experiments ($\omega =$ 2.6 rpm) based on the tracer particle flowing layer passage time. To investigate the impact of the flowing layer depth, conditions with $0 \leq \epsilon \leq 0.20$ were also simulated. For context, previous studies on quasi-2D flows reported flowing layer depth of $\epsilon \approx 0.1$ [43], depending on the particle to tumbler diameter ratio d/D.

The implementation of the measured axial velocity changes the w component of $\mathbf{u}_{\text{fl}}$. For a tracer point in grid cell (i,j) (see text), $w = v_{ax}(i,j)$. The random walk diffusion is included as a 50% probability of adding or subtracting the standard deviation of the axial velocity in the corresponding grid cell ($\sigma_{ax}(i,j)$). In MATLAB, this is done using an integer random number generator on the domain [1 2], as $w = v_{ax}(i,j) + c(-1)^{\texttt{randi}([1,2],1)}\sigma_{ax}(i,j))$, where c is a weighting term that adjusts the strength of diffusion. Tracer positions are generated by integrating the velocity field using the Runge-Kutta (RK4) method in the flowing layer and the semi-implicit Euler method in the bulk [101, 24]. The dimensionless time step is $\Delta t/T = 5 \cdot 10^{-5}$ to ensure stability.

APPENDIX D

Poincaré sections and dynamical systems features

Stroboscopic maps (also known as Poincaré sections or discrete time maps) of 500 iterations were used to investigate mixing and non-mixing behavior and to provide direct comparison to experiments. The stroboscopic maps utilized tracer points seeded at the intersection of the flowing layer boundary and the $r = 0.95$ hemispherical shell at zero iterations (blue points) and at the first half-iteration (red points). Regions avoided by the tracer particles correspond to elliptic regions (islands). The outer boundary orbits of these elliptic regions were obtained by finely seeding initial conditions near the boundary in successive stroboscopic maps until the boundary orbits were extracted. The periodicity of these elliptic regions was determined by tracking tracers seeded in these regions. In the 3D spherical tumbler rotated with the same speed about both the z-axis and the x-axis, the Poincaré section exists on invariant surfaces parametrized by the radius of hemispherical shells [24]. In other words, tracer points have trajectories that lie on the same radial surfaces they start on.

Periodic fixed points are classified by the eigenvalues of the Jacobian matrix $D\Delta = \left(\frac{\partial \Delta_i}{\partial x_j}\right)$ for a period-n mapping of $\Delta^n(\boldsymbol{x}) = \boldsymbol{x}$ [24, 146]. For the volume-preserving map studied here, the three eigenvalues have a product of $\lambda_1\lambda_2\lambda_3 = 1$. There is a null direction at each periodic point providing a local invariant, corresponding to the eigenvalue of 1, $\lambda_1 = 1$ [146]. An elliptic point has two eigenvalues that form a complex conjugate pair with $\lambda_2 = \overline{\lambda_3}$ and $|\lambda_2| = |\lambda_3| = 1$. Therefore, they can be expressed in trigonometric form as $\lambda_{2,3} = \cos\phi \pm i \sin\phi$, where ϕ is related to the internal rotation angle of the elliptic region surrounding the elliptic point. A hyperbolic point has two real eigenvalues, $\lambda_2 = 1/\lambda_3$. Material expands along the

direction corresponding to eigenvalue $\lambda > 1$, and contracts along the direction corresponding to eigenvalue $\lambda < 1$ [106]. The stable manifolds consist of all points that converge to the hyperbolic point as number of iteration approaches infinity, while the unstable manifolds consist of all points that converge to the hyperbolic point in the reverse time. Therefore, the stable manifolds and unstable manifolds can be traced by tracking points seeded on the corresponding eigenvectors in backward time and forward time, respectively. The unstable manifolds are traced by tracking points seeded on a short line segment of length $0.001R_o$. Positions of tracer points are recorded after every iteration, and the resulting manifolds shown for each protocol in Chapter 5 Fig. 5.15(a-c) are trajectories of tracer points advected for 15 iterations. In order to maintain a uniform density tracing in the presence of fast manifold stretching, new points are back inserted in intervals between consecutive points that are $5 \times 10^{-5}R_o$ apart or further after each iteration. Similarly, the stable manifolds in Chapter 6 Fig. 6.11(c) and 6.14(c) are trajectories advected for 14 and 28 iterations, respectively.

APPENDIX E

Piecewise isometry model

The PWI model is applicable in the infinitely thin flowing layer (ITFL) limit ($\epsilon = 0$) of the continuum model [78, 77, 122]. Like the continuum model, stroboscopic maps were used to investigate mixing and non-mixing regions. Because the flow dynamics are radially invariant with an ITFL, tracer positions are mapped by their angular displacements on the hemispherical shell. When tracers reach the free surface, they are instantaneously reflected across the ITFL in the streamwise direction. The initial positions of the passive tracers in the stroboscopic maps were selected to lie along the isometry partitions at zero iterations (blue points in figures) and the first half-iteration (red points in figures) and mapped for 10,000 iterations to assure convergence.

APPENDIX F

Segregation experiments

Segregation experiments of size-bidisperse BST systems under few other protocols beyond those in Chapter 5.2 demonstrate accumulation of large particles into non-mixing regions.

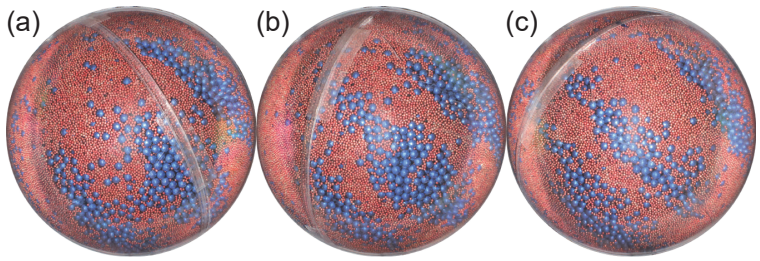

Figure F.1. Segregation experiments in a half-full spherical tumbler under protocol $(57°, 57°, 90°)$ rotated at 2.6 rpm for particle size ratio $R = 3.56$ and $f = 15\%$ after (a) 20 iterations, (b) 40 iterations, and (c) 50 iterations. Segregation pattern forms at approximately 15 iterations and persists with further iterations.

Figure F.2. Five segregation experiments in a half-full spherical tumbler after 30 iterations of protocol $(57°, 57°, 90°)$ rotated at 2.6 rpm for particle size ratio $R = 3.56$ and $f = 15\%$. Segregation pattern for $(57°, 57°, 90°)$ is repeatable.

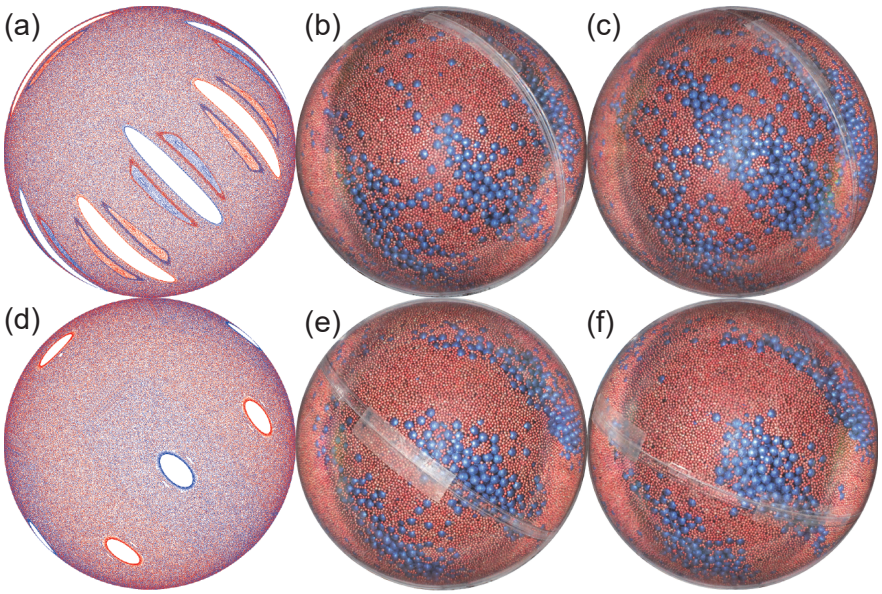

Figure F.3. Poincaré sections (left column) compared to experiments (right columns) after 30 iterations of protocol $(54°, 54°, 90°)$ in (a-c) and $(60°, 60°, 90°)$ in (d-f) with two experiments for each. Period 3 segregation pattern is obvious for protocols with rotation angles in the range of $(54° - 60°)$.

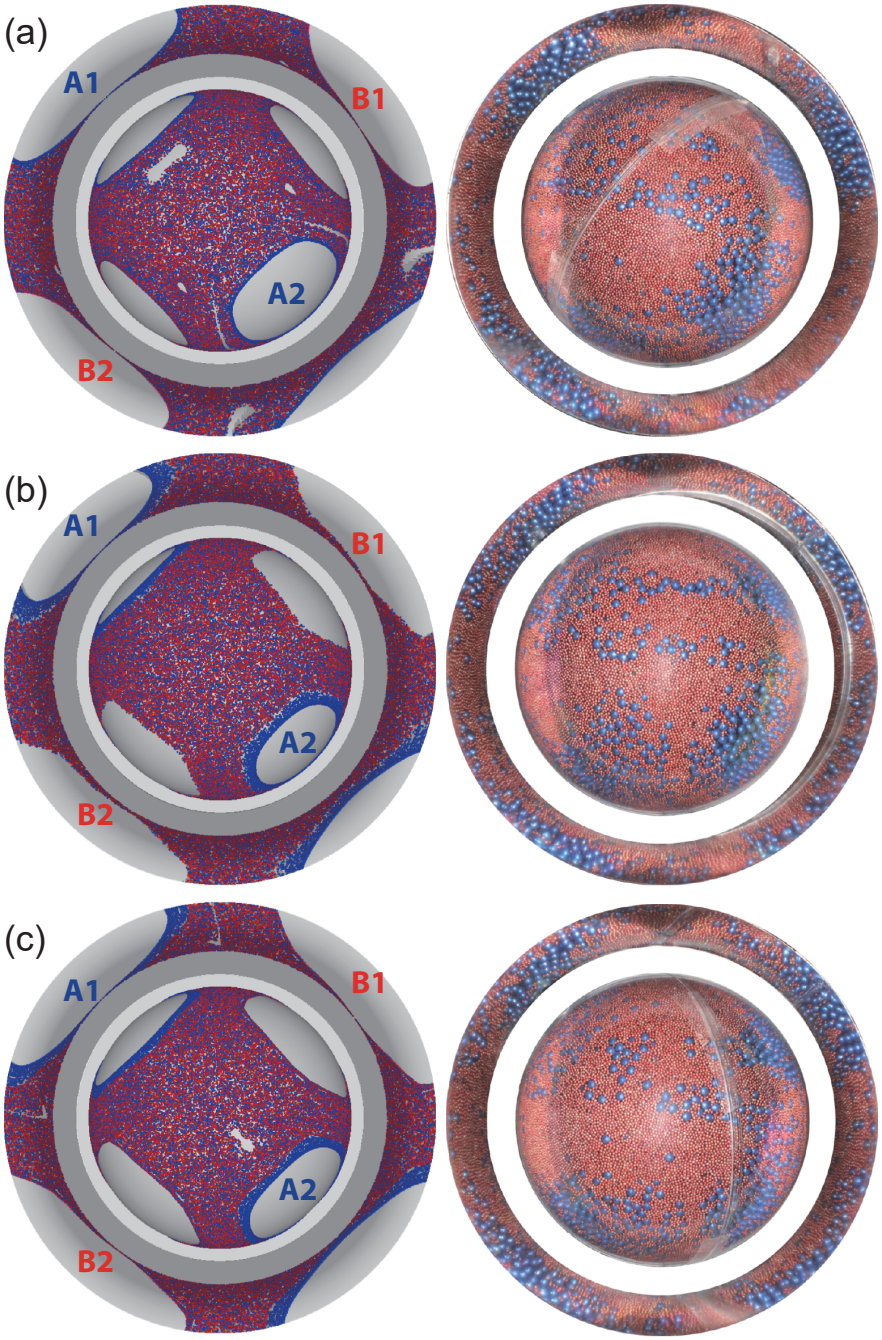

Figure F.4. Poincaré sections (left column) compared to experiments (right column) after 30 iterations of protocol (a) $(93°, 93°, 85°)$, (b) $(93°, 93°, 90°)$, and (c) $(96°, 96°, 90°)$. Period-2 segregation pattern is obvious for protocols with rotation angles within a few degrees of 90° and angle between rotation axes $85° \leq \gamma \leq 90°$.

APPENDIX G

DEM simulation

Bi-axial spherical tumbler flows are simulated using the discrete element method (DEM) with frictional smooth boundaries. The particles are modeled as rigid bodies and their collisions as a slight overlap. The contact forces are computed based on the overlap and their velocities. Thorough discussions of the DEM simulations in dense granular flows can be found in literature [30, 143, 144, 133], and the methods used here are also described in detail elsewhere [42, 137, 168] A linear-spring dashpot force model is used for normal contacts between two particles:

$$\vec{F}_{ij}^{n} = [k_n \zeta - 2\gamma_n m_{\text{eff}} (\vec{V}_{ij} \cdot \hat{\vec{r}}_{ij})] \hat{\vec{r}}_{ij}$$

where ζ and $\vec{V}_{ij}$ represent the overlap and relative velocity, respectively, between two contact particles i and j. The unit normal vector is denoted by $\vec{r}_{ij}$, and the reduced mass is $m_{\text{eff}} = m_i m_j/(m_i + m_j)$. The normal stiffness k_n and damping γ_n of the granular material are determined from the restitution coefficient e and collision time t_c by $k_n = [(\pi/t_c)^2 + \gamma_n^2] m_{\text{eff}}$ and $\gamma_n = -\ln(e)/t_c$. Tangential forces are modeled using a hybrid Coulomb-like friction approach that models static friction with a spring and sliding friction in the standard way:

$$\vec{F}_{ij}^{t} = \min(|k_t \beta_{ij} + 2\gamma_t m_{\text{eff}} (\vec{V}_{ij} \times \hat{\vec{r}}_{ij})|, \mu_s |\vec{F}_{ij}^{n}|) \text{sgn}(\beta) \hat{\vec{s}}_{ij}$$

where the tangential stiffness is $k_t = \frac{2}{7} k_n$. The tangential displacement β_{ij} is defined as $\beta_{ij} = \int_{t_s}^{t} \vec{V}_{ij} \times \hat{\vec{r}}_{ij} dt$, where t_s is initial contact time. The restitution coefficient e is set to 0.87, and friction coefficients μ are 0.6 for contacts between particles as well as between particles and tumbler wall. In most cases unless specifically noted, the spherical tumbler of radius $R_o = 7$ cm is half-filled with a size bi-disperse mixture of $d = 4$ mm and 2 mm

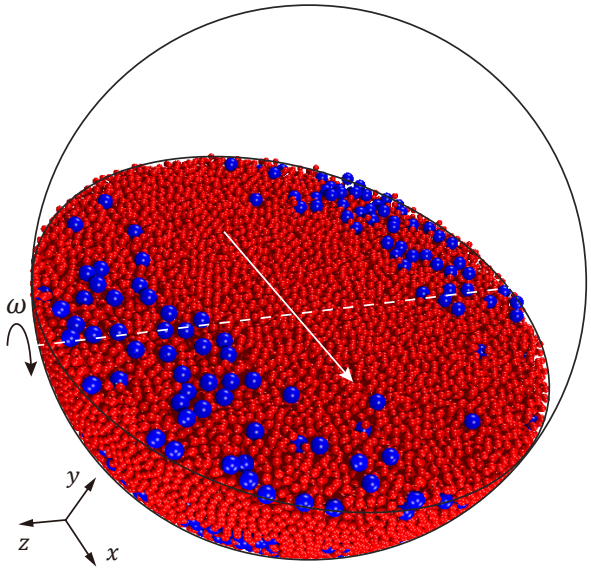

Figure G.1. Rendering of DEM simulation of a size-bidisperse mixture in a spherical tumbler, rotating about the z-axis with angular speed ω. Particles flow across the free surface in a thin flowing layer in the direction indicated by the white arrow and drift toward the poles due to a weak axial velocity (see main text).

particles of density $\rho = 2500\,\mathrm{kg\,m^{-3}}$. The concentration of large versus small particles is varied from 0.05 to 0.25. The spherical tumbler is rotated at 3 rpm, which is close to the value of 2.6 rpm in experiments [173, 171]. A rendering of a DEM simulation in the spherical tumbler with a size-bidisperse mixture is shown in Fig. G.1.